DISSERTATION

TAILORING SOLID-LIQUID INTERACTIONS TO CONTROL DROPLET WETTING AND DYNAMICS

Submitted by

Hamed Vahabi

Department of Mechanical Engineering

In partial fulfillment of the requirements

For the Degree of Doctor of Philosophy

Colorado State University

Fort Collins, Colorado

Summer 2019

Doctoral Committee:

Advisor: Arun K. Kota

Lakshmi Prasad Dasi
Simon Tavener
Todd M Bandhauer

ABSTRACT

TAILORING SOLID-LIQUID INTERACTIONS TO CONTROL DROPLET WETTING AND DYNAMICS

Recent advances in micro/nano-scale fabrication techniques and synthesis of novel chemicals with a variety of functionalities have opened up new avenues in tailoring solid-liquid interactions. In this work, by systematically tuning the wettability and slipperiness of solid surfaces, we developed a multitude of novel surfaces and strategies. First, we developed metamorphic superomniphobic surfaces that display wetting transition in response to heat. Second, we systematically studied the dynamics of droplets of various liquids during coalescence-induced jumping on textured super-repellent surfaces. Third, we developed a simple and passive strategy consisting of superomniphobic surfaces with a protruding macrotexture to demonstrate coalescence-induced jumping with significantly higher energy conversion efficiency, compared to state-of-the-art surfaces. Fourth, we developed a simple "grafting to" technique to fabricate a novel non-textured hydrophilic surface that is counterintuitively slippery with unprecedented potential to enhance the heat transfer coefficient in dropwise condensation. Fifth, we developed a novel triboelectric-based droplet manipulation technique on smooth hydrophobic slippery surfaces that is very simple without any complex fabrication of manipulation platform or expensive actuation system. Overall, the novel surfaces and strategies developed in this work have significant implications for phase-change heat transfer, liquid transportation, anti-fouling, self-cleaning, drag reduction, corrosion control, and manipulation of liquid droplets.

ACKNOWLEDGEMENTS

It is a great pleasure to convey my gratitude to many people without whose participation and assistance the completion of this dissertation would not have been possible.

The foremost among those people is my supervisor, Dr. Arun K. Kota. I would like to express my sincere appreciation for his unwavering support, helpful and insightful criticism, and understanding spirit throughout my PhD. With his determined, experienced and enthusiastic nature, he has been a mentor for me both academically and non-academically.

I would also like to thank my outstanding committee members, Dr. Simon Tavener, Dr. Lakshmi Prasad Dasi and Dr. Todd M. Bandhauer for their encouragement, support and constructive comments.

I extend a warm thanks to my colleague in our research group, Dr. Wei Wang, for his truthful friendship and precious company. I would like to thank all my teachers and professors for inspiring me to love learning.

Last in order, but not in importance, I would like to deliver my love to my beloved wife for her patience, support and encouragement.

DEDICATION

To my beloved wife, Samira,

for her unconditional love, wholehearted support, and day to day encouragement.

She is the only reason of all my endeavors

and any recognition given to me is equally given to her.

TABLE OF CONTENTS

LIST OF FIGURES

LIST OF PUBLICATIONS

So far, the following peer-reviewed journal publications have resulted from my PhD work at Colorado State University (in reverse chronological order):

* means equal contribution

1. Wu, A.*; **Vahabi, H.***; Cha, H.; Chavan, S.; Kim, M-K.; Wang, W.; Kota, A. K.; Miljkovic, N., Dropwise Condensation on Solid Hydrophilic Surfaces. ***Science Advances*** (Under review). Impact factor ~ 11.5

2. Wang, W.; Du, X; **Vahabi, H.**; Kota, A. K.; Tong, T.; Monolithic Omniphobic Membranes: Trade-off in Membrane Distillation, ***Nature Communications*** (Accepted). Impact factor ~ 12.4

3. Wang, W.*; **Vahabi, H.***; Movafaghi, S.; Arun K. Kota, Superomniphobic Surfaces with Improved Durability via Synergistic Effect of Hierarchical Texture and Mechanical Interlocking, ***Advanced Materials Interfaces*** (Under review). Impact factor ~ 4.3.

4. Movafaghi, S.; Cackovic, M. D.; Wang, W.; **Vahabi, H.**; Pendurthi, A.; Kota, A. K.; Superomniphobic Papers for On-paper pH Sensors, ***Advanced Materials Interfaces***, (Accepted).

5. Yan, X.; Zhang, L.; Sett, S.; Feng, L.; Huang, Z.; **Vahabi, H.**; Kota, A. K.; Chen, F.; Miljkovic, N., Droplet Jumping: Effects of Droplet Size, Surface Structure, Pinning, and Liquid Properties, ***ACS Nano***. 2019. Impact factor ~ 13.7

6. **Vahabi, H.***; Wang, W.*; Mabry, S. M.; Kota, A. K., Coalescence-induced Jumping of Droplets on Superomniphobic Surfaces with Macrotexture. ***Science Advances***, 4(11), eaau3488, 2018.

7. Wang, W.; Salazar, J.; **Vahabi, H**.; Joshi-Imre, A.; Voit, W. E.; Kota, A. K., "Metamorphic Superomniphobic Surfaces," ***Advanced Materials***, 2017, 29(27). Impact factor ~ 21.9

8. **Vahabi, H.***; Wang, W.*; Davies, S.; Mabry, S. M.; Kota, A. K., "Coalescence induced self-propulsion of droplets on superomniphobic surfaces," ***ACS Applied Materials & Interfaces***, 2017, 9(34). Impact factor ~ 8.

9. **Vahabi, H.***; Wang, W.*; Movafaghi, S.; Kota, A. K., "Free-Standing, Flexible, Superomniphobic Films," **ACS Applied Materials & Interfaces**, 2016, 8(34).

10. Wang, W.; Lockwood, K.; Boyd, L. M.; Davidson, M. D.; Movafaghi, S.; **Vahabi, H.**; Khetani, S. R.; Kota, A. K., "Superhydrophobic Coatings with Edible Materials," **ACS Applied Materials & Interfaces**, 2016, 8(29).

11. Bark Jr, D. L.; **Vahabi, H.**; Bui, H.; Movafaghi, S.; Moore, B.; Kota, A. K.; Popat, K. C.; Dasi, L. P., "Hemodynamic Performance and Thrombogenic Properties of a Superhydrophobic Bileaflet Mechanical Heart Valve," **Annals of biomedical engineering**, 2017, 45(2). Impact factor ~ 3.3.

12. **Vahabi, H.**; Wang, W.; Popat, K. C.; Kwon, G.; Holland, T. B.; Kota, A. K., "Metallic Superhydrophobic Surfaces via Thermal Sensitization," **Applied Physics Letters**, 2017, 110(25). Impact factor ~ 3.4.

OVERVIEW

In recent years, extensive efforts have been devoted to the investigation of textured super-repellent surfaces (i.e., surfaces that display extreme repellency to liquids) and also smooth slippery surfaces (i.e., surfaces that allow extreme liquid mobility). The extreme liquid repellency and liquid mobility on such surfaces arises from the combination of appropriate surface texture and surface chemistry. Controlling the surface texture and/or surface chemistry, allows tailoring of the solid-liquid interaction to control the droplet wetting and dynamics. Recently, tailoring the wettability and slipperiness of textured super-repellent surfaces and also smooth slippery surfaces has attracted significant attention due to their applications in droplet manipulation and coalescence-induced self-propulsion of droplets, which will be discussed in the following chapters.

In this dissertation, the fundamental chemical and physical principles of designing textured super-repellent and also smooth slippery surfaces will be reviewed in chapter two. Then, our contributions in design and fabrication of textured super-repellent surfaces (e.g., surfaces with switchable wettability) and their applications (i.e., coalescence-induced self-propulsion of droplets in the capillary regime as well as the visco-capillary regime) will be presented in chapter three. Further, the first-ever passive strategy to significantly increase the energy conversation efficiency in coalescence-induced jumping of droplets will be introduced. Following that, our contributions in fabrication of smooth slippery surfaces (e.g., a novel hydrophilic yet slippery surface) and their applications (i.e., enhanced dropwise condensation, and a novel triboelectric-based droplet manipulation technique) will be presented in chapter four. Finally, the contributions of this work to fundamental science and applied science will be summarized in chapter five and also the potential aspects of this work for future investigation will be presented.

1. CHAPTER 1- BACKGROUND

1.1. Introduction

Recent advances in micro/nano-scale fabrication techniques and also chemicals with variety of functionalities have opened up new avenues in tailoring solid-liquid interactions to control the wettability and slipperiness of solid surfaces against contacting droplets. Such control is of great interest for industrial applications such as anti-fouling,[13] self-cleaning,[14-17] drag reduction,[18-22] chemical shielding,[23-24] icephobicity,[25-28] micro-robots,[29-31] anti-corrosion coatings,[32-33] and manipulation of liquid droplets.[34-36] The wettability and slipperiness of solid surfaces are characterized by two parameters – (i) contact angle (governing the profile of a droplet on a solid surface), and (ii) contact angle hysteresis (i.e., the difference between the advancing [maximum] and receding [minimum] contact angles) or roll-off angle (or sliding angle) ω (i.e., the minimum angle by which the surface must be tilted relative to the horizontal for the droplet to roll-off or slide).[37-42] In this chapter, the fundamentals of tailoring the wettability and slipperiness of solid surfaces and their motivations will be presented.

1.2. Fundamentals of Wettability and Slipperiness

The primary measure of wetting of a liquid on a non-textured (i.e., smooth) solid surface (**Figure 1-1a**) is the equilibrium (or Young's) contact angle θ_Y, given by Young's equation:[43]

$$cos\theta_Y = \frac{\gamma_{sv}-\gamma_{sl}}{\gamma_{lv}} \tag{1-1}$$

Here, γ_{sv}, γ_{sl} and γ_{lv} are the solid surface energy, the solid-liquid interfacial tension and the liquid surface tension, respectively.

When a liquid droplet contacts a textured solid surface, it displays an apparent contact angle θ^*, and it can adopt either the Wenzel[44] state or the Cassie–Baxter[45] state to minimize its overall free energy. In Wenzel state, the liquid fully wets the solid surface (even between protrusions, see **Figure 1-1b**) and in the Cassie-Baxter state, air is trapped between the solid and the liquid (**Figure 1-1c**) and θ^* is calculated using the Cassie-Baxter relation:[45]

$$cos\theta^* = f_{sl}cos\theta + f_{la}cos\pi = f_{sl}cos\theta - f_{la} \quad (1\text{-}2)$$

Here, f_{sl} is the area fraction of the solid–liquid interface and f_{la} is the area fraction of the liquid–air interface underneath the liquid droplet on a textured surface.

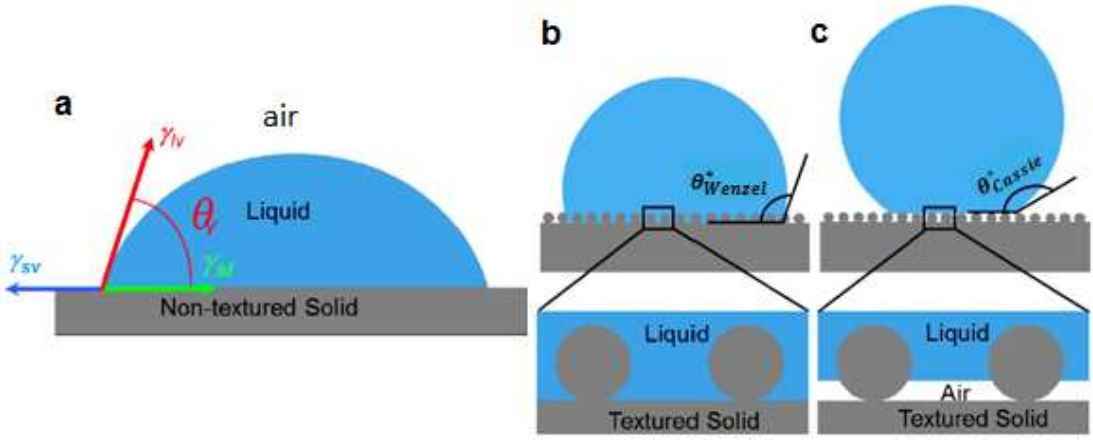

FIGURE 1-1. Schematic of a liquid droplet. (a) On a non-textured surface. **(b)** On a textured surface in the Wenzel state, **c)** On a textured surface in the Cassie-Baxter state.

Eq. (1-2) indicates that for a given value of θ_Y on a textured surface, θ^* can be increased through reducing the f_{sl} and/or increasing the f_{la}.[3, 46-47] Further, lower f_{sl} and higher f_{la} lead to lower contact angle hysteresis $\Delta\theta^* = \theta^*_{adv} - \theta^*_{rec}$ in the Cassie-Baxter state.[3, 46-47] Here, θ^*_{adv} and θ^*_{rec} are the apparent advancing [maximum] and apparent receding [minimum] contact angles, respectively. Contact angle hysteresis, primarily arises from physical heterogeneity (i.e., surface roughness) and chemical heterogeneity[3, 48-53] and indicates the energy barriers that oppose the movement of a liquid droplet on a solid surface. In fact, contact angle hysteresis

characterizes the resistance against droplet movement.[48-49] So, higher contact angle hysteresis results in higher roll-off angle (or sliding angle) ω.

Depending on the wettability of surfaces in contact with high surface tension liquids (e.g., water), they are broadly categorized as superhydrophilic (i.e., contact angle → 0°), hydrophilic (i.e., contact angle < 90°), hydrophobic (i.e., contact angle > 90°), and superhydrophobic (i.e., contact angle > 150°). Similarly, if a surface in contact with low surface tension liquids (e.g., hydrocarbons) displays such contact angles, it is considered superoleophilic, oleophilic, oleophobic, and superoleophobic, respectively. If a surface is both superhydrophobic and superoleophobic, it is considered superomniphobic.[3, 24, 42, 54] Further, depending on the mobility of a liquid droplet on a solid surface, the surface is slippery if the contact angle hysteresis (or roll off angle or sliding angle) is < 10°, indicating negligible adhesion between a solid surface and the contacting droplet.[3, 24, 42, 54] The Cassie-Baxter state is preferred for designing super-repellent surfaces because it can lead to very high θ^* and very low $\Delta\theta^*$, which in turn results in low roll off angle (or sliding angle) ω.[3, 55-56]

1.3. Textured Super-repellent Surfaces

Typically, superhydrophobic and superomniphobic surfaces are fabricated by combining a surface chemistry possessing low solid surface energy (typically $\gamma_{sv} < 15\ \mathrm{mN\ m^{-1}}$) with textured surfaces[3, 24, 42, 54, 57-61] (note that both the surface chemistry and the surface texture affect the surface wettability).[62] Therefore, the wettability of super-repellent surfaces and thus the interaction of liquid droplets with such surfaces can be tailored by tuning the surface chemistry or surface texture.

It is evident from the Young's relation (Eq.1-1) that the contact angle θ_Y increases with decreasing solid surface energy γ_{sv}. This implies that surfaces with very high surface energy tend

to display lower contact angles, while surfaces with very low surface energy tend to display higher contact angles. Therefore, surfaces with low surface energy are preferred to obtain liquid repellency. Zisman *et al.*[63] reported that among various surface functional groups, the surface energy decreases in the order $-CH_2 > -CH_3 > -CF_2 > -CF_2H > -CF_3$. Consequently, non-polar fluorinated and perfluorinated materials, including perfluorinated phosphates, perfluorinated silanes, fluorinated polymers and copolymers, and other fluorinated precursors have become the logical choice of materials used in designing super-repellent surfaces.[3] Of all the fluorinated materials, 1H,1H,2H,2H heptadecafluorodecyl molecules deserve a special mention, because they are among the lowest surface energy materials ever produced.[3] On the contrary, surfaces become more hydrophilic in the order non-polar < polar, no hydrogen-bonding < polar, hydrogen-bonding < hydroxylic < ionic. Hence, polar polymers (e.g., polyethylene glycol) and ionic polymers (e.g., zwitterionic silanes) are widely used in fabrication of hydrophilic and superhydrophilic surfaces.[64-66]

As mentioned previously, super-repellency can be obtained on textured surfaces in the Cassie-Baxter state. Although the formation of the Cassie–Baxter state is desirable in designing superomniphobic surfaces, not all types of textures can lead to a Cassie–Baxter state with low surface tension liquids, which display a Young's contact angle $\theta_Y \ll 90°$.[3] To illustrate this qualitatively, consider the two types of textures shown in **Figures 1-2a and b**, both having the same solid surface energy. The texture shown in Figure 1-2a is concave (texture angle $\psi > 90°$) and the texture shown in Figure 1-2b is convex ($\psi < 90°$) facing upwards. In both the cases, any liquid contacting the texture in the Cassie–Baxter state locally displays a contact angle equal to the Young's contact angle θ_Y. A stable Cassie–Baxter state results only when $\theta_Y \gg \psi$.[3, 58, 67-69] This is because if $\theta_Y < \psi$, the net traction on the liquid–vapor interface is downward due to the

capillary force, which promotes imbibition of the liquid into the solid texture, leading to a fully wetted Wenzel state. Consequently, low surface tension liquids, which display a Young's contact angle $\theta_Y < 90°$, cannot be in a stable Cassie–Baxter state on textures with $\psi > 90°$ (Figure 1-2a). However, they can be in a robust Cassie–Baxter state on textures with $\psi < 90°$ (Figure 1-2b). Such convex topographies, with $\psi < 90°$, are called re-entrant textures. Re-entrant texture (such as the texture of the springtail skin shown in **Figure 1-2c**) is necessary in designing superomniphobic surfaces.

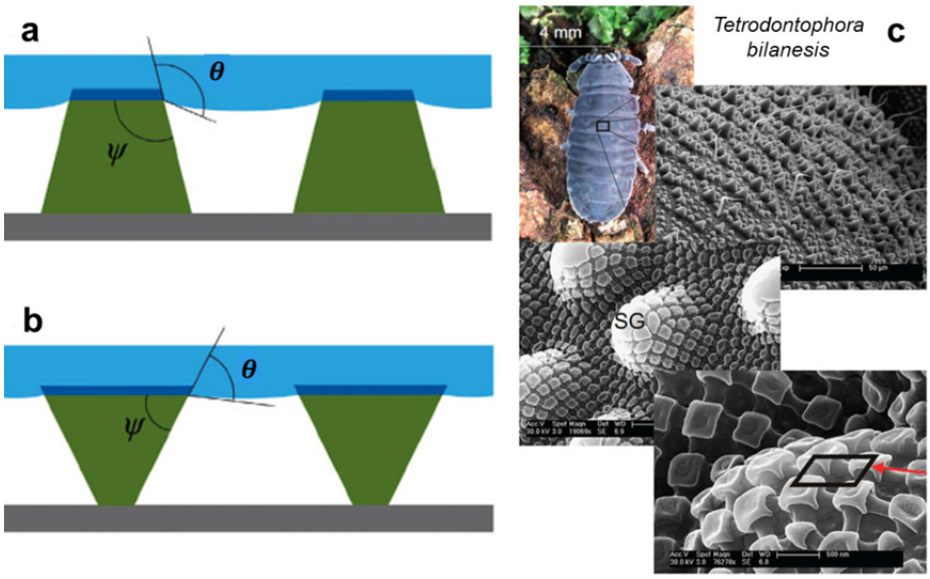

FIGURE 1-2. The critical role of re-entrant texture. (a) A schematic of a concave texture ($\psi > 90°$) showing a liquid droplet with $\theta > 90°$ in the Cassie–Baxter state. **(b)** A schematic of a concave texture ($\psi < 90°$) showing a liquid droplet with $\theta < 90°$ in the Cassie–Baxter state. **(c)** A picture and SEM images of hierarchical structured springtails skin where secondary granules (SG) are superimposed on primary granules. Reproduced with permission.[3] © 2014 Nature Publishing Group.

In addition to the re-entrant form, the hierarchical scales of the textures have a constructive influence on super-repellency of surfaces. Typically, hierarchically structured surfaces consist of a finer length scale texture on an underlying coarser length scale texture (**Figures 1-3a–c**). When a hierarchically structured surface supports a contacting liquid droplet in the Cassie–Baxter state at all length scales, the liquid droplet typically displays higher apparent contact angles compared

with surfaces with a single scale of texture. This is because air is trapped at multiple length scales for a hierarchically structured surface, while air is trapped only at one length scale for surfaces with a single scale of texture.

Hierarchically structured surfaces that can support a contacting liquid droplet in the Cassie–Baxter state also display lower contact angle hysteresis $\Delta\theta^*$ compared with surfaces with a single scale of texture.[42, 56, 60, 70] As mentioned before, contact angle hysteresis is related to energy barriers that a liquid droplet must overcome during its movement along a solid surface and thus characterizes the resistance to the droplet movement.[48] Lower solid–liquid contact area leads to lesser contact line pinning (i.e.,, lower resistance to droplet movement) and consequently lower contact angle hysteresis. Typically, hierarchically structured surfaces (**Figure 1-3c**) have significantly lower solid–liquid contact area compared with surfaces that possess a single scale of texture (Figures 1-3a and 1-3b). This results in significantly lower contact angle hysteresis. Consequently, hierarchically structured surfaces possessing re-entrant texture with very low solid–air interfacial tension, which can support low surface tension liquids in the Cassie–Baxter state, are ideal for designing superomniphobic surfaces.

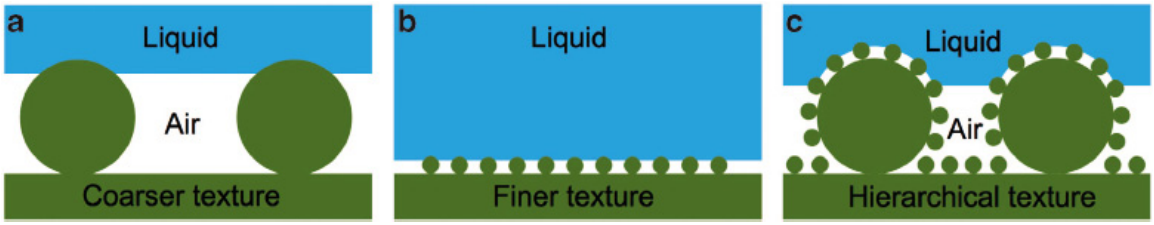

FIGURE 1-3. The need for hierarchical scales of texture. (a-c) Schematics of a liquid droplet in the Cassie–Baxter state on a coarser textured surface, a finer textured surface and a hierarchically textured surface, respectively. Reproduced with permission.[3] © 2014 Nature Publishing Group.

1.4. Smooth Slippery Surfaces

Despite extensive efforts over the past years, retaining the robustness of super-repellent surfaces in harsh conditions continues to be a grand challenge in the field.[5] For instance, the air

cushion required to sustain the super-repellency can vanish due to liquids impinging at high pressure or damage of the surface texture or dissolution into the surrounding fluid.[5] These drawbacks of super-repellent surfaces encouraged scientists to come up with a new strategy of tailoring the solid-liquid interaction to ensure the nearly free motion of liquids on solid surfaces. This strategy (i.e., slippery liquid-infused porous surfaces SLIPS) mainly involves surfaces containing pockets of a lubricating liquid rather than air (**Figure 1-4a**).[71] The premise for such a strategy is that a liquid surface is intrinsically smooth and defect-free and a liquid droplet, which is immiscible and whose wetting is energetically unfavorable compared to the lubricant, can slide on SLIPS very easily (**Figure 1-4b**).[5] SLIPS were brought to prominence through developments reported independently by LaFuma and Quere[72] and Wong *et al.*[71] and have subsequently been described in more detail in applications including condensation enhancement,[73] anti-icing,[74] and paper-based microfluidics.[75] SLIPS repel low surface tension liquids,[71, 76] which is critical for applications in thermal management and hydrocarbon processing; for example, SLIPS can promote formation of highly mobile droplets of low surface tension liquids, including hydrocarbons with surface tensions as low as pentane (γ_{lv}~16 mN m^{-1}).[71] SLIPS can also improve condensation heat transfer of water in the dropwise mode.[73]

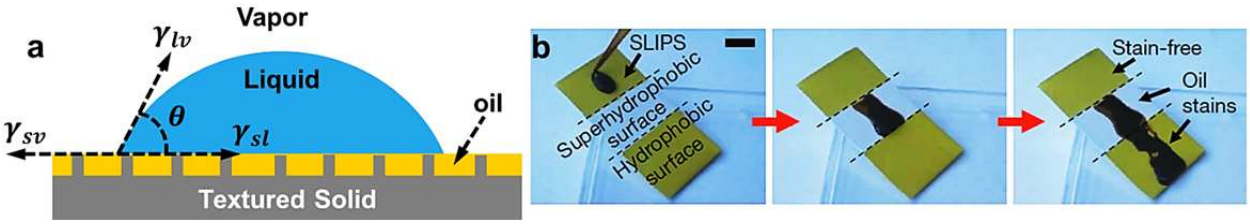

FIGURE 1-4. Slippery liquid-infused porous surfaces SLIPS. (a) A liquid droplet rests on a SLIPS surface. **(b)** Movement of light crude oil on a substrate composed of a SLIPS, a superhydrophobic Teflon porous membrane, and a flat hydrophobic surface. Note the slow movement on and staining of the latter two regions. Reproduced with permission.[5] © 2017 Taylor & Francis Group.

Despite the rapid progress in fabrication of SLIPS, recent studies have shown that the loss of the lubricating liquid (either by evaporation or by the removal of lubricant along with the moving droplets) leads to degradation of the low adhesion characteristic of SLIPS.[77-78] Further, presence of a thick (on the order of micrometers) lubricant layer (with low thermal conductivity) increases the thermal resistance at solid-vapor interface and thus reduces the overall heat transfer coefficient in thermal-fluidic applications. In order to circumvent these drawbacks, recently, covalently attached flexible, lubricating molecules are introduced onto smooth surfaces to make them extremely slippery.[77] The few nanometer-thick grafted groups impart a liquid-like quality to solid surfaces and are not easily washed away or depleted by evaporation. However, these surfaces were limited to the fabrication of hydrophobic slippery surfaces, which highly limits their thermal-fluidic applications (due to low nucleation rate,[79-80] poor wicking,[81] or high Kapitza resistance[82]) as well as bio-fluidic applications (due to very poor bio-fouling resistance[83]). Chapter 3 presents the first-ever hydrophilic surface that is counter-intuitively slippery with significant potential for thermal-fluidic and bio-fluidic applications due to very high nucleation rate, strong wicking, low Kapitza resistance and also very high bio-fouling resistance.

1.5. Switchable Wettability

Over the past few decades, natural surfaces exhibiting stimuli-responsive behaviors, such as the color changes of echinoderms in response to light and heat-shock-responsive behavior of bacteria provided researchers with great inspiration for designing numerous intelligent materials.[84] Among various kinds of intelligent surfaces, smart stimuli-responsive surfaces with switchable wettability have attracted significant interest due to numerous applications, such as controlled drug delivery,[85] cell encapsulation,[86] oil/water separation,[87] and sensors.[88] According to their responsiveness to different external stimuli, smart materials are divided into several

groups, including photo-responsive materials, thermally responsive materials, pH/solvent-responsive materials, electricity-responsive materials, UV light-responsive, plasma-responsive and stress-responsive materials (**Figure 1-5**).[84]

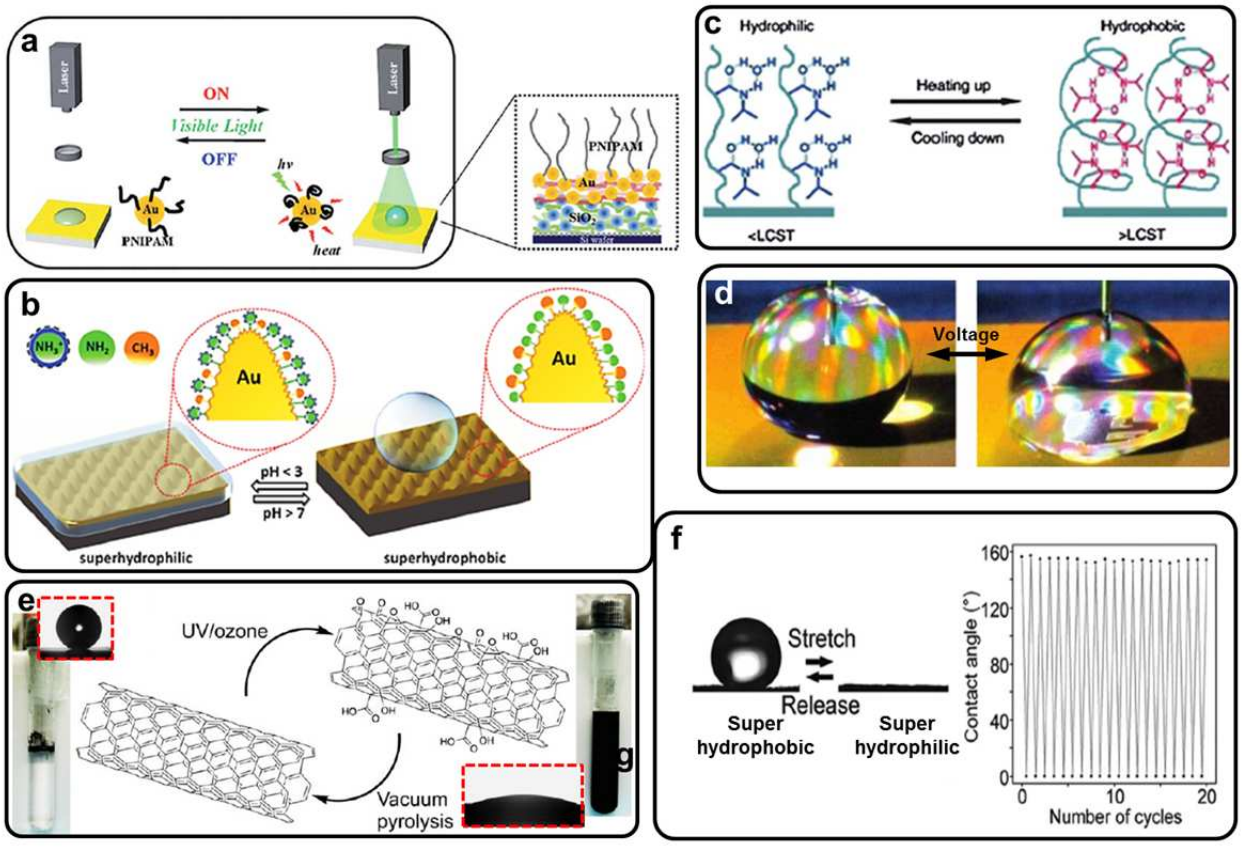

FIGURE 1-5. Switchable wettability methods. (a) Photo responsive. Reproduced with permission.[2] © 2012 The Royal Society of Chemistry **(b)** pH responsive. Reproduced with permission.[7] © 2013 Wiley **(c)** Temperature responsive. Reproduced with permission.[9] © 2004 John Wiley and Sons **(d)** Voltage responsive. Reproduced with permission.[10] © 2007 American Chemical Society **(e)** UV responsive. Reproduced with permission.[11] © 2011 American Chemical Society **(f)** Strain responsive. Reproduced with permission.[12] © 2004 John Wiley and Sons.

For example, Sun *et al.*[9] studied the reversible switching of superhydrophobic surfaces induced by controlling the temperature. They showed the wettability of poly (N-isopropylacrylamide)-modified surfaces can be dramatically changed from superhydrophilicity to superhydrophobicity by increasing the temperature by only 30°C. In order to fabricate a pH-responsive surface, Yu *et al.*[89] combined a fractal-like gold surface obtained via

electrodeposition technique and a mixed thiol self-assembled monolayer to create an acid/base sensitive surface. They observed that their surface is superhydrophobic with acidic droplets and superhydrophilic with basic water droplets. In another study, Minko *et al*.[90] studied controlling of a polymer surface wettability by exposing the surface to different solvents. The solvent sensitivity evoked the switchable wettability from superhydrophilic to superhydrophobic state. Lim *et al*.[91] reported the fabrication of rose-like nanostructured V_2O_5 films that are photo-responsive. The wettability of textured V_2O_5 films was reversed from superhydrophobicity to superhydrophilicity upon UV light irradiation. As another external stimulus, plasma treatment was used by Song *et al*.[92] to create superhydrophobic surface with controllable wettability. They synthesized poly (L-lactic acid) (PLLA) superhydrophobic surfaces using phase inversion-based methods. They showed that by increasing Ar-plasma treatment hydrophilicity of the samples increases. Further, Zhang *et al*.[93] controlled the surface texture of an elastic polyamide film by cooperation of bi-axially extending and unloading the film. Their surfaces exhibited reversible wettability from superhydrophilicity upon extending to superhydrophobicity upon unloading.

Despite the rapid progress in fabrication of surfaces showing switchable wettability, prior work has mainly focused on switchable wettability via changes in chemistry at solid-liquid interfaces, induced by the external stimuli. Chapter 2 discusses the first-ever report of combining the superomniphobicity and shape memory effect to systematically design superomniphobic surfaces with metamorphic textures (i.e., textures that transform their morphology in response to an external stimulus). The wetting transitions on our surfaces are solely due to transformations in morphology of the texture and not due to changes in chemistry.

1.6. Droplet Dynamics on Super-repellent and Slippery Surfaces

In recent years, super-repellent surfaces and also smooth slippery surfaces have been widely used to achieve on-demand (controlled) droplet manipulation. In this context, it is important to understand the fundamental mechanisms that govern manipulation of droplets tangential or perpendicular to surfaces.

1.6.1. Droplet motion tangential to a surface

Rolling or sliding of a droplet on a surface is a measure of the droplet mobility on the surface. Various passive techniques (e.g., wettability gradient, Laplace pressure gradient, photo-induced deformation) have been employed to manipulate droplets tangentially on surfaces for applications in fog harvesting and self-cleaning.[94-98] When a droplet on a solid surface is stimulated, the droplet tends to move toward the stimulation direction, provided the stimulation force can overcome the adhesion force at the solid-liquid interface (**Figure 1-6**).

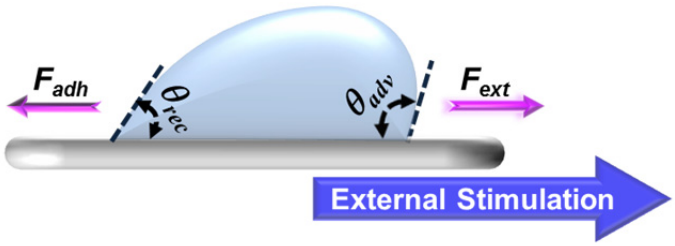

FIGURE 1-6. Droplet motion under external stimulation tangent to a surface.

The adhesion force at solid-liquid interface, arising from the contact angle hysteresis, can be calculated as:

$$F_{adh} = \int_{l_1}^{l_2} \gamma_{lv}(cos\theta_{rec} - cos\theta_{adv})dl \quad (1\text{-}3)$$

Here, l is the integration variable along the width of the droplet.[99] According to Furmidge,[100] if a droplet is placed on an inclined solid surface, based on a balance between the external (here gravitational) force and the adhesion force at solid-liquid interface, the roll off or sliding angle ω

(i.e., the minimum angle by which the surface must be tilted relative to the horizontal for the droplet to roll off or slide) is given as:

$$\omega = \sin^{-1}[\frac{\gamma_{lv} D_{TCL}(cos\theta_{rec} - cos\theta_{adv})}{mg}] \quad (1\text{-}4)$$

Here, m is the mass of the droplet, g is the acceleration due to gravity, and D_{TCL} is the width of the triple phase contact line perpendicular to the rolling/sliding direction. When the shape of the droplet does not deviate significantly from a spherical cap, the width of the triple phase contact line can be computed as:

$$D_{TCL} = 2\cos(\bar{\theta}^* - \frac{\pi}{2})[\frac{3V}{\pi(2 - 3cos\bar{\theta}^* + cos^3\bar{\theta}^*)}]^{1/3} \quad (1\text{-}5)$$

Here, V is the volume of the droplet and $\bar{\theta}^*$ is the average apparent contact angle, given as:

$$cos\bar{\theta}^* = \frac{cos\theta^*_{adv} + cos\theta^*_{rec}}{2} \quad (1\text{-}6)$$

The roll off angle (or sliding angle) can be measured to characterize the droplet mobility on a solid surface. Further, minimizing the contact angle hysteresis (e.g., through increasing the liquid-vapor area fraction f_{lv} on the super-repellent surface) is a universal strategy to reduce the roll off (or sliding) angle, which results in higher droplet mobility on functional surfaces.

Chapter 2-1 demonstrates a variation in droplet mobility (measured by the rolling angle) on our Metamorphic Superomniphobic (MorphS) Surfaces by altering the liquid-air area fraction f_{la} via morphology transformation. Chapter 3 demonstrates the tangential motion of droplets on smooth slippery surfaces under triboelectric stimulation.

1.6.2. Droplet motion perpendicular to a surface

In this section, two types of perpendicular interactions of droplets with surfaces are considered – a) impingement of droplets on solid surfaces, and b) coalescence-induced self-propulsion of droplets on surfaces. Despite their differences, these dynamic processes are both

highly influenced by the local solid-liquid interactions at the contact area and also the deformation of the droplets during the processes.

When a liquid droplet with radius R_0, density ρ, viscosity μ, and velocity u impinges a super-repellent or slippery surface (showing negligible solid-liquid adhesion, **Figure 1-7a**), it spreads on the surface. During spreading, the kinetic energy of the droplet (scales as $\rho R_0^3 u^2$) is partly converted into the excess surface energy (scales as $\gamma_{lv} A_{surf}$, where A_{surf} is the area of the droplet), while the rest of it is being dissipated due to the viscosity (scales as $\mu R_0^2 u$).[101] Weber number $We = \rho u^2 R_0/\gamma_{lv}$ measures the relative importance of the kinetic energy of the droplet compared to its surface energy. Further, Reynolds number $Re = \rho u R_0/\mu$ measures the relative importance of the kinetic energy of the droplet compared to viscos dissipation.

Prior work demonstrated that at low We, the droplet deforms slightly when it impinges the surface and the restitution coefficient (i.e., ratio of the kinetic energy of the droplet after and before impingement) is very large indicating negligible energy dissipation.[101-102] If a droplet impinges on a surface with higher We, it is subject to a pronounced deformation leading to the redistributed liquid flow from vertical to horizontal direction. Subsequently, in the retraction stage, the droplet bounces back from the surface in the capillary-inertial regime (where the initial kinetic energy is mainly converted into the surface energy) or visco-capillary regime (where the initial kinetic energy is mainly dissipated by the viscosity).[103-105]

One of the most important issues preventing the complete bouncing of droplets from textured super-repellent surfaces is the Cassie to Wenzel transition,[44-45, 54, 106-109] which is an indication of the breakdown of the super-repellent property.

Perpendicular interaction of droplets with functional surfaces can also be seen in the coalescence-induced self-propulsion of droplets on super-repellent surfaces, which has

similarities with the retraction stage of the droplet impingement process, and has potential applications in self-cleaning and sustained dropwise condensation (**Figure 1-7b**).[101] Due to these applications, dynamics of the droplets coalescing on a super-repellent surface has attracted significant interest. Similar to the retraction stage of the droplet impingement process, when two liquid droplets (with radius R_0, density ρ, viscosity μ, **Figure 1-7c**) coalesce, the overall surface area of the merged droplet decreases due to the reduction in the overall area of the droplet A_{surf}. This results in a release of the excess surface energy, which drives the coalescence.[6, 8, 110-116]

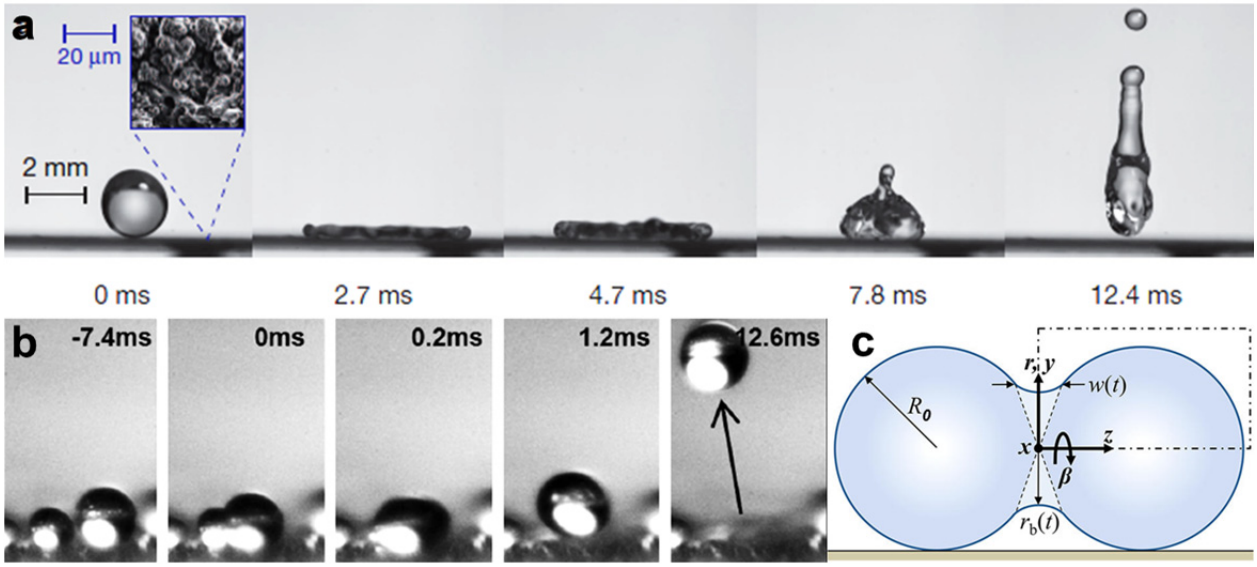

FIGURE 1-7. Droplet motion perpendicular to a surface. (a) Water droplet impinging on a superhydrophobic surface. Reproduced with permission.[1] © 2013 Springer Nature. **(b)** Coalescence-induced self-propulsion of water droplets on a superhydrophobic surface. Reproduced with permission.[6] © 2009 American Physical Society. **(c)** Schematic of two droplets undergoing coalescence defined by radius R_0. Reproduced with permission.[8] © 2014 American Chemical Society.

During coalescence, the excess surface energy is partly converted into the total kinetic energy, while the rest of it is lost due to viscous dissipation. Droplet coalescence is inherently a symmetric process, which is followed by periodic expansion and contraction of the merged droplet in the plane of coalescence (i.e., no scope of the perpendicular motion of the droplet, see **Figure 1-8a**). Assuming the viscous dissipation is negligible (i.e., inertial-capillary regime),[4, 8]

all the released surface energy during the coalescence is converted into the total kinetic energy and according to the balance of these two energy components, the inertial-capillary velocity can be defined as:[4, 8, 110-117]

$$V_{ic} = \sqrt{\frac{\gamma_{lv}}{\rho R_0}} \tag{1-7}$$

However, when two liquid droplets coalesce on a super-repellent surface (showing negligible solid-liquid adhesion), presence of a super-repellent surface breaks the symmetry of coalescence (**Figure 1-8b**). This results in a velocity component perpendicular to the plane of coalescence and away from the super-repellent surface that allows the coalesced droplet to self-propel away from the surface at a jumping velocity V_j.[4, 8, 110-116] Prior work[4, 8, 110-116] has demonstrated that the coalescence-induced jumping velocity of droplets V_j scales as the inertial-capillary velocity V_{ic}.

Chapter 2-2 describes a systematic study on different regimes of coalescence-induced self-propulsion of liquid droplets (i.e., both inertial-capillary and visco-capillary regimes) by using a wide range of droplet radii, viscosities, and surface tensions. As a result of this study, we demonstrate that the classic scaling analysis derived based on an energy argument in the inertial-capillary regime cannot be extended to the visco-capillary regime.

Prior work.[4, 8, 110-111] has also demonstrated that the measured droplet jumping velocities are significantly smaller than those predicted based on the inertial-capillary scaling law (i.e., equation 1-7). This indicates that only a small fraction of the released surface energy is converted into the out of plane kinetic energy (allowing the droplet to self-propel from the surface) and the majority of the released surface energy is consumed during the periodic expansion and contraction of the droplet in the plane of coalescence. Enright *et al.*[8] argued that < 6% of the released surface energy on a super-repellent surface can be transformed into perpendicular

kinetic energy. Such low energy conversion does not allow coalescence-induced jumping of high viscosity droplets (due to significant viscous dissipation) or low surface tension droplets (due to lack of sufficient excess surface energy).[118-119] In order to enable the coalescence-induced jumping of a wide range of liquids (including those with high viscosity or low surface tension), it is necessary to increase the energy conversion efficiency. For example, Lv *et al*.[120] reported that coalescence-induced self-propulsion of multiple droplets results in higher jumping velocities due to the relatively lower energy barrier. In addition to the coalescence-induced release of excess surface energy, electric fields have also been used to enhance the jumping motion.[121] Further, recent work revealed the coalescence-induced self-propulsion of droplets under a low-pressure environment, resulting from the generation of an overpressure underneath the droplet as a result of fast evaporation.[122]

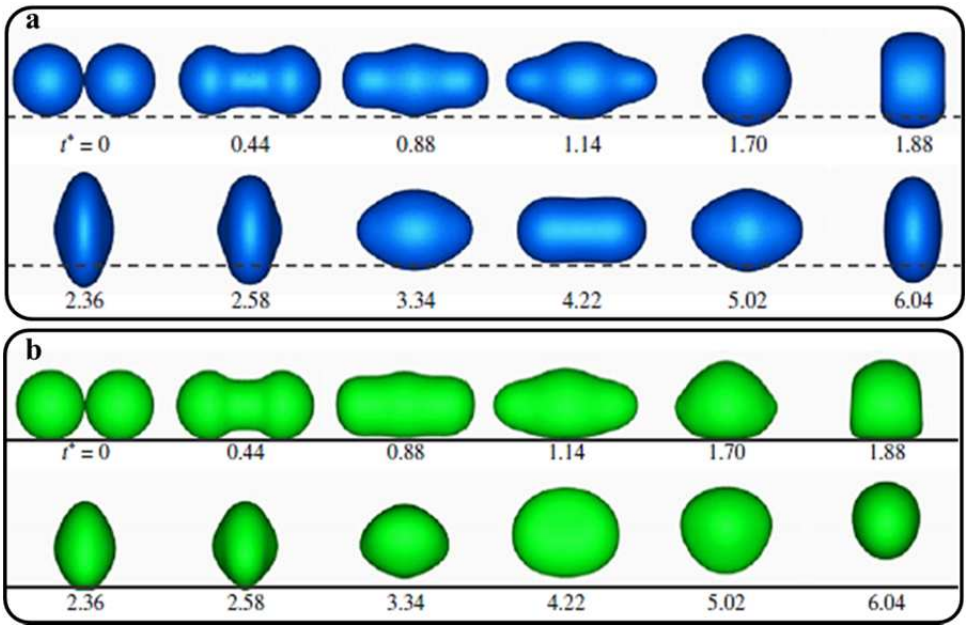

FIGURE 1-8. Droplet coalescence. (a) in the air **(b)** on a super-repellent surface. Note the top view of the coalescence on a super-repellent surface is similar to the panel a. Reproduced with permission.[4] © 2014 Cambridge University Press

Despite all efforts, to the best of our knowledge, there are no reports of simple and passive techniques that can increase the energy conversion efficiency in coalescence-induced jumping of droplets. In order to circumvent this drawback, chapter 2-3, presents a passive technique to significantly increase the upward kinetic energy of the coalesced droplets and thus the energy conversion efficiency during the coalesce-induced self-propulsion of droplets.

2. CHAPTER 2- TEXTURED SUPER-REPELLENT SURFACES

2.1. Metamorphic Superomniphobic Surfaces

Summary: Rewritable liquid patterns are an emerging application of superomniphobic surfaces with wetting transition capability that can be obtained through tuning the surface chemistry and/or the surface morphology. While prior work has mainly focused on tuning the surface chemistry, altering the surface wettability (against low surface tension liquids) through changing the morphology of the solid surface has not been investigated. In this work, by combining superomniphobicity and shape memory effect, we developed the first ever metamorphic superomniphobic (MorphS) surfaces that transform their morphology in response to heat (**published in Advanced Materials, 2017**). Further, we established a theoretical framework to design such surfaces based on a balance between the pressure induced by a droplet to the surface and the breakthrough pressure on the surface. Along with rewritable liquid patterns, we envision that the robust MorphS surfaces with reversible wetting transition will have a wide range of applications including hazardous liquid transport, controlled drug release, lab-on-a-chip devices, and biosensors.

2.1.1. Introduction

Superomniphobic surfaces are extremely repellent to virtually all liquids – aqueous or organic, acids or bases or solvents, Newtonian or non-Newtonian.[3, 23, 40] Recently, temporal and on-demand switching of the wettability of superomniphobic surfaces has absorbed huge interests due to its application in rewritable liquid patterns, hazardous liquid transport. However, to the best of our knowledge, there are no reports that combine superomniphobicity and shape memory effect to systematically design superomniphobic surfaces with metamorphic textures (i.e., textures that transform their morphology in response to an external stimulus). In this work,[123] we present the first-ever metamorphic superomniphobic (MorphS) surfaces fabricated with a thermo-responsive shape memory polymer (SMP).[124-126] Unlike prior work,[9, 127-130] utilizing our MorphS surfaces, we demonstrate the distinctly different wetting transitions of liquids with different surface tensions and elucidate the underlying physics. The wetting transitions on our MorphS surfaces are solely due to transformations in morphology of the texture. We envision that our robust MorphS surfaces with reversible wetting transitions will have a wide range of

applications including rewritable liquid patterns, controlled drug release systems, liquid-liquid separation membranes, lab-on-a-chip devices, and biosensors.

2.1.2. Design Principles

As described in chapter one, when a liquid droplet is in Cassie-Baxter state, pockets of air remain trapped underneath the liquid droplet introducing a composite liquid-air-solid interface. This greatly reduces the solid-liquid interfacial area, which in turn leads to high θ^* and low roll off angles ω.[3, 39] The Cassie-Baxter state can be obtained by combining a surface chemistry possessing a low solid surface energy with an appropriate texture.[3, 41] Assuming our MorphS surfaces composed of a hexagonal array of mushroom-like pillars can be represented by a hexagonal array of cylindrical pillars capped with a circular plate having rounded edges (**Figure 2-1.a** and **2-1.b**), f_{sl} and f_{lv} can be determined as:

$$f_{sl} = \frac{A_{sl}}{A_{total}} = \frac{\pi(R-r)^2+2\pi[r(\pi-\theta)][R-r+\frac{r}{3}\left(\frac{\frac{3}{2}+2cos\theta+\frac{1}{2}cos2\theta}{\pi-\theta-sin\theta}\right)]}{2\sqrt{3}(D+R)^2} \tag{2-1}$$

$$f_{lv} = \frac{A_{lv}}{A_{total}} = 1 - \frac{\pi(R-r+rsin\theta)^2}{2\sqrt{3}(D+R)^2} \tag{2-2}$$

Here, A_{total} is the area of a hexagonal unit cell, A_{sl} is the area of the solid-liquid interface, A_{lv} is the area of the liquid-air interface, R is radius of the circular plate cap of the pillar, D is half the edge-to-edge spacing between the circular plate caps and r is radius of the rounded edge of the circular plate cap. For our MorphS surfaces, in which $r \ll R$, we can represent them as a hexagonal array of cylindrical pillars capped with a cylindrical plate (**Figure 2-1.c**), and f_{sl} and f_{lv} can be simplified as:

$$f_{sl} \approx \frac{\pi}{2\sqrt{3}\left\{1+\left(\frac{D}{R}\right)\right\}^2} \tag{2-3}$$

$$f_{lv} \approx 1 - \frac{\pi}{2\sqrt{3}\left\{1+\left(\frac{D}{R}\right)\right\}^2} \tag{2-4}$$

The Cassie-Baxter equation can then be rewritten as:

$$cos\theta^* = f_{sl}cos\theta - f_{lv} \approx \left(\frac{\pi}{2\sqrt{3}\left(1+\frac{D}{R}\right)^2}\right)cos\theta - \left(1 - \frac{\pi}{2\sqrt{3}\left(1+\frac{D}{R}\right)^2}\right) \tag{2-5}$$

It is evident from equation (2-5) that high values of the liquid-air area fraction f_{lv}, which can be obtained by increasing the ratio D/R, lead to high apparent contact angles θ^*. Further, high values of liquid-air area fraction f_{lv} also lead to low contact angle hysteresis $\Delta\theta^*$,[100] which in turn lead to low roll off angles ω.

The Cassie-Baxter state is a metastable state. When a sufficiently high pressure is applied on a liquid in the Cassie-Baxter state, the liquid will breakthrough, (i.e., permeate and fully wet the protrusions) thereby transitioning to the Wenzel state. The breakthrough pressure $P_{breakthrough}$ is the minimum pressure that can force such a transition from the Cassie-Baxter state to the fully wetted Wenzel state and to have effective super-repellence to liquids, it is essential to have a robust Cassie-Baxter state with high $P_{breakthrough}$.

In order to determine the breakthrough pressure $P_{breakthrough}$ of water on our MorphS surfaces composed of a hexagonal array of mushroom-like pillars, we assume that the texture can be represented by a hexagonal array of cylindrical pillars capped with a cylindrical plate and the liquid-air interface is pinned at the very top of the cylindrical plate (**Figure 2-1d**). A force balance at the liquid-air interfaces gives:[60]

$$P_{breakthrough,water} \approx \frac{-2\pi\gamma_{lv}cos\theta}{R\left[2\sqrt{3}\left\{\left(\frac{D}{R}\right)+1\right\}^2-\pi\right]} \tag{2-6}$$

Similarly, we can determine the breakthrough pressure $P_{breakthrough}$ of n-hexadecane, by assuming that the liquid-air interface is pinned at the very bottom of the cylindrical plate (**Figure**

2-1.e). For n-hexadecane, note that the liquid-air interface cannot get pinned at the top of the cylindrical plate[58, 61] and a force balance at the liquid-air interfaces gives:[58, 60]

$$P_{breakthrough,oil} \approx \frac{2\pi\gamma_{lv}sin\theta}{R\left[2\sqrt{3}\left\{\left(\frac{D}{R}\right)+1\right\}^2-\pi\right]} \tag{2-7}$$

Further, if a droplet of water comes in contact with collapsed pillar texture, the breakthrough pressure can be estimated by assuming that the hexagonal array of collapsed pillars can be represented as a hexagonal array of rectangular pillars (**Figure 2-1.f**) with half the pillar width R and half the edge-to-edge spacing between pillars D that are different in the parallel direction and the diagonal direction (for the collapsed pillar texture, $D_d > D_p$).

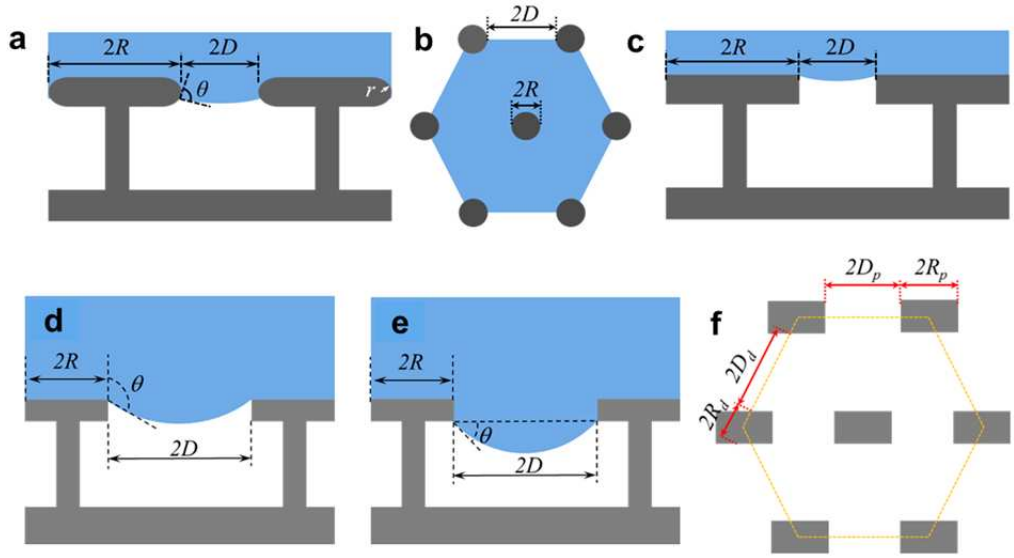

FIGURE 2-1. Schematics of the texture of MorphS surfaces. (a-b) Side view and the top view, respectively, of a hexagonal array of cylindrical pillars capped with a circular plate having rounded edges. **(c)** Side view of a hexagonal array of cylindrical pillars capped with a cylindrical plate. **(d-e)** Liquid-air interface pinned at the very top and the very bottom, respectively, of the cylindrical plate. (f) Top view of a hexagonal array of collapsed pillars.

Since breakthrough occurs more easily for larger inter-pillar spacing, we anticipate that the breakthrough would occur along the diagonal direction of the collapsed pillars. Assuming that the liquid-air interface is pinned at the top of the pillars, estimated the breakthrough pressure $P_{breakthrough}$ of water as:[58, 60]

$$P_{breakthrough,collapsed} \approx \frac{-2\pi\gamma_{lv}cos\theta}{R_d\left[2\sqrt{3}\left\{\left(\frac{D_d}{R_d}\right)+1\right\}^2-\pi\right]} \quad (2\text{-}8)$$

Our MorphS surfaces possess texture on two length scales – the coarser length scale (mushroom-like pillar texture or collapsed pillar texture) and the finer length scale (bump-like texture between the coarser pillar texture, **Figure 2-2a**).

Assuming that the finer bump-like texture can be represented as a hexagonal array of cylindrical pillars (with radius R_{fine} and half the edge-to-edge spacing between D_{fine}, **Figure 2-2.b**) and the liquid-air interface is pinned at the very top of the pillar, we have estimated the breakthrough pressure $P_{breakthrough}$ of water as:[58, 60]

$$P_{breakthrough,fine} \approx \frac{-2\pi\gamma_{lv}cos\theta}{R_{fine}\left[2\sqrt{3}\left\{\left(\frac{D_{fine}}{R_{fine}}\right)+1\right\}^2-\pi\right]} \quad (2\text{-}9)$$

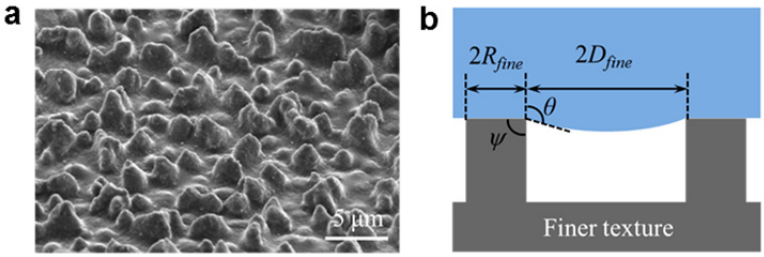

FIGURE 2-2. Finer bump-like texture of our MorphS surfaces. (a) SEM image. **(b)** Schematic illustrating the side view of a hexagonal array of cylindrical pillars.

For a droplet in the Cassie-Baxter state on a surface, the applied pressure acting downwards on the liquid-air interface can be estimated as $P_{applied} \approx 2\gamma_{lv}R_{drop}$. If $P_{breakthrough} \gg P_{applied}$, the droplet continues to remain in the Cassie-Baxter state and if $P_{breakthrough} \leq P_{applied}$, the droplet transitions to the Wenzel state.[58, 60]

2.1.3. Fabrication and Characterization

Relying on the design principles discussed above, in this work, we fabricated our MorphS surfaces by combining hexagonal arrays of re-entrant textured mushroom-like pillars of a thiol-

ene/acrylate-based thermo-responsive shape memory polymer SMP[125, 131] with a surface chemistry possessing a low solid surface energy (see **CH. 2-1 Supplementary Information**). We fabricated the mushroom-like pillars of the thermoresponsive shape memory polymer through a combination of photolithography and reactive ion etching (**Figure 2-3**). Subsequently, we modified the surface chemistry using a fluorinated silane to impart low solid surface energy, $\gamma_{sv} \approx 10$ mN/m.

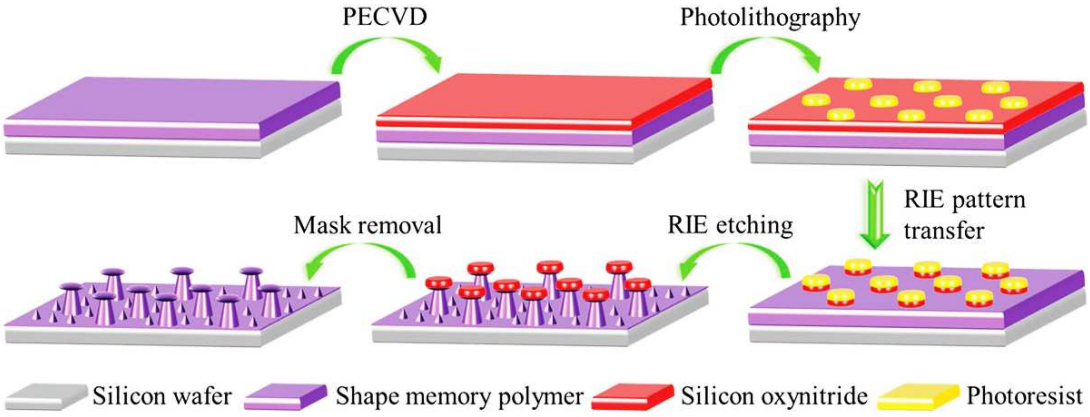

FIGURE 2-3. Schematic illustrating the fabrication of MorphS surfaces. PECVD is plasma enhanced chemical vapor deposition and RIE is reactive ion etching.

2.1.4. Results and Discussion

In order to obtain superomniphobicity, we systematically increased the ratio D/R of the mushroom-like pillar texture (**Figures 2-4.a-c**) by using different masks in the photolithography step. As might be anticipated from equation (2-5) and the related discussion, increasing the ratio D/R (i.e., the pillars are farther apart and/or the mushroom caps are smaller in size) increases the liquid-air area fraction f_{lv} in the Cassie-Baxter state, which in turn increases the apparent contact angles (particularly the receding contact angle, see **Figure 2-4.d**), decreases the contact angle hysteresis (see Figure 2-4.d) and decreases the roll-off angles (see **Figure 2-4e**) for both water (a

representative liquid with high surface tension, $\gamma_{lv} \approx 72.1$ mN/m) and n-hexadecane (a representative liquid with low surface tension, $\gamma_{lv} \approx 27.5$ mN/m).

The experimentally measured roll off angles of ~8 µL droplets of water and n-hexadecane are in good agreement with the predicted roll off angles obtained using equation 1-5. At sufficiently high liquid-air area fraction $f_{lv} \approx 97\%$, the surface is both superhydrophobic ($\theta^*_{adv} = 166°$, $\theta^*_{rec} = 154°$, and $\omega = 5°$ for water) and superoleophobic ($\theta^*_{adv} = 164°$, $\theta^*_{rec} = 146°$, and $\omega = 7°$ for n-hexadecane), and consequently the surface is superomniphobic.

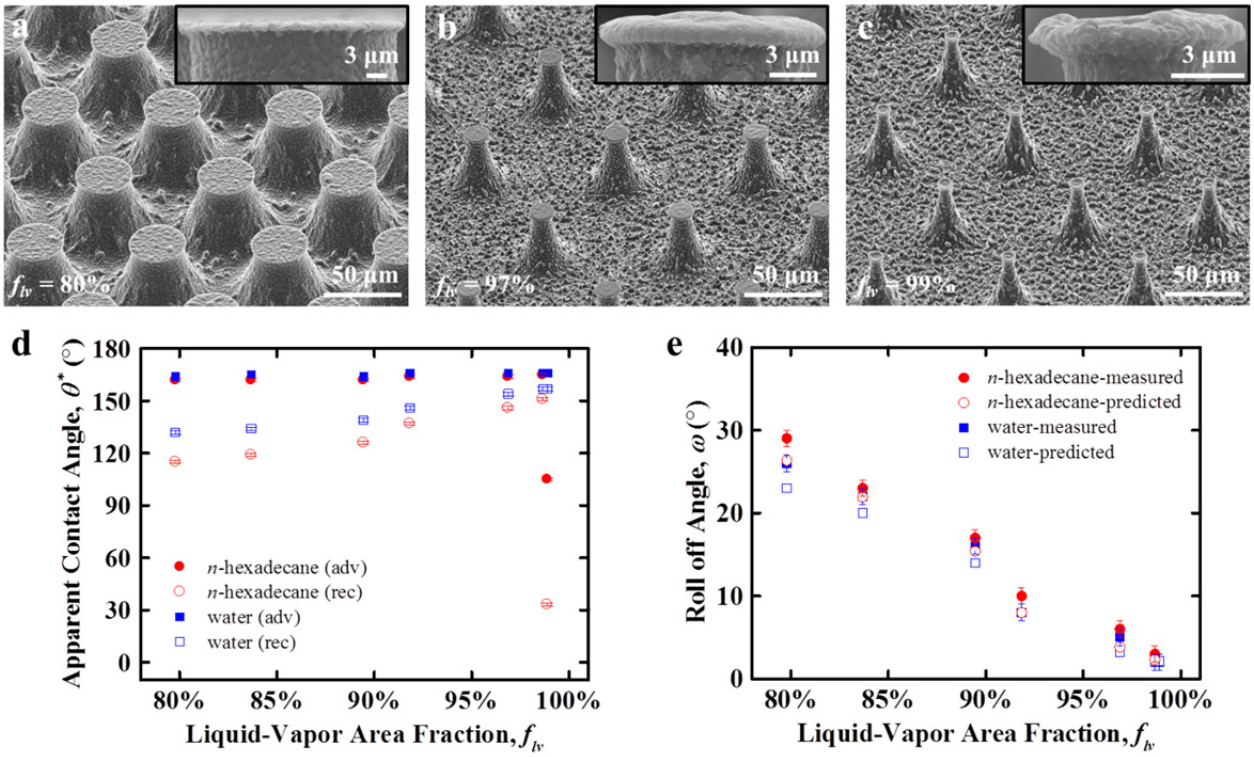

FIGURE 2-4. Characterization of MorphS surfaces. (a-c) SEM images showing the morphology of mushroom-like pillar texture with different D/R ratios that result in liquid–air area fractions $f_{lv} \approx 80\%$, 97%, and 99%, respectively. The insets show the re-entrant texture of the mushroom caps. **(d-e)** Apparent contact angles and roll off angles, respectively, of n-hexadecane and water droplets (≈8 µL) on MorphS surfaces with different liquid–air area fractions.

Based on equation (2-6), on the mushroom-like pillar texture with $f_{lv} \approx 97\%$ ($R \approx 7.3$ µm, $D \approx 32.1$ µm; see Figure 2-4.b) and $f_{lv} \approx 99\%$ ($R \approx 6.6$ µm, $D \approx 55$ µm; Figure 3-4.c), the

breakthrough pressure $P_{breakthrough} \approx 258$ Pa and $P_{breakthrough} \approx 92$ Pa, respectively, for water ($\theta \approx \theta^*_{adv} = 114°$). For a ~8 μL water droplet, the applied pressure on the water-air interface can be estimated as, $P_{applied} \approx 2\gamma_{lv}/R_{drop} \approx 116$ Pa. The water droplet adopts the Cassie-Baxter state on the surface with $f_{lv} \approx 97\%$ because $P_{breakthrough} \gg P_{applied}$. In contrast, the water droplet adopts the Wenzel state on the surface with $f_{lv} \approx 99\%$ because $P_{breakthrough}$ is comparable to $P_{applied}$. Further, Based on equation (2-7), on the mushroom-like pillar texture with $f_{lv} \approx 97\%$ ($R \approx 7.3$ μm, $D \approx 32.1$ μm; see Figure 2-4.b) and $f_{lv} \approx 99\%$ ($R \approx 6.6$ μm, $D \approx 55$ μm; Figure 2-4.c), the breakthrough pressure $P_{breakthrough} \approx 238$ Pa and $P_{breakthrough} \approx 85$ Pa, respectively, for n-hexadecane ($\theta \approx \theta^*_{adv} = 79°$). For a ~8 μL n-hexadecane droplet, the applied pressure on the n-hexadecane-air interface can be estimated as, $P_{applied} \approx 2\gamma_{lv}/R_{drop} \approx 44$ Pa. The n-hexadecane droplet adopts the Cassie-Baxter state on the surface with $f_{lv} \approx 97\%$ because $P_{breakthrough} \gg P_{applied}$. In contrast, the n-hexadecane droplet adopts the Wenzel state on the surface with $f_{lv} \approx 99\%$ because $P_{breakthrough}$ is comparable to $P_{applied}$. Consequently, even small vibrations in our experimental setting induced a transition of water and n-hexadecane droplets into the Wenzel state with lower apparent contact angles θ^*, higher contact angle hysteresis $\Delta\theta^*$, and no roll off. So, we employed MorphS surfaces with liquid-air area fraction $f_{lv} \approx 97\%$ in all the results discussed below.

We chose to fabricate our MorphS surfaces with the thiol-ene/acrylate copolymer because the morphology of the texture can be transformed reversibly by heating above the glass transition temperature $T_g \approx 60$°C (**Figure 2-5.a**; also CH. 2-1 Supplementary Information).[132-134] When the mushroom-like pillar texture (see **Figure 2-5.b**) is heated above the glass transition temperature, deformed under a compressive stress (~ 10 MPa), and cooled down to room temperature, the morphology is immediately "locked" into a new collapsed pillar texture (i.e., mushroom-like

pillars are flattened, **Figure 2-5.c**). During this morphological transformation, the polymer chains of the crosslinked SMP are temporarily deformed into a more ordered, low entropy state (i.e., collapsed pillar texture) at elevated temperature. Upon cooling below T_g, the collapsed pillars remain locked in this ordered state because the entropic gains in reverting back to the more disordered state (i.e., mushroom-like pillar texture) are insufficient to overcome the inter-chain and intra-chain steric hindrance. Upon reheating above T_g, the morphology is transformed back to the mushroom-like pillar texture (**Figure 2-5.d**) because the higher mobility of the polymer chains allows them to revert back to the more disordered state. By repeating this process, the morphology can be reversibly transformed between the mushroom-like pillar texture and the collapsed pillar texture. While the mushroom-like pillar texture (with $f_{lv} \approx 97\%$) possesses a higher D/R and a re-entrant texture (i.e., $R \approx 7.3$ μm, $D \approx 32.1$ μm, Figure 2-4.b), the collapsed pillar texture possesses a lower effective D/R (i.e., $R_p \approx 15.2$ μm, $D_p \approx 24.2$ μm in the parallel direction and $R_p \approx 8.4$ μm, $D_p \approx 32$ μm in the diagonal direction; Figures 2-1.f and 2-5.c) and no re-entrant texture. Indeed, the ratios D/R in the parallel direction $D_p/R_p \approx 1.6$ and in the diagonal direction $D_d/R_d \approx 3.8$ (and correspondingly the liquid-air area fraction f_{lv}) of the collapsed pillar texture are lower than the ratio $D/R \approx 4.4$ for the mushroom-like pillar texture. Hence, since wettability depends strongly on the morphology of the texture,[68, 135-138] especially the ratio D/R (which directly influences f_{lv} in the Cassie-Baxter state) and the presence or absence of re-entrant texture, the reversible morphological transformations on our MorphS surfaces can induce programmable wettability transitions that are distinctly different for liquids with different surface tensions.

Let us consider the wettability transitions of water, a representative high surface tension liquid, on our MorphS surfaces. When a droplet of water comes in contact with the as-prepared

mushroom-like pillar texture, it adopts the Cassie-Baxter state because $P_{breakthrough} \approx 258\ \text{Pa} \gg P_{applied} = 116\ \text{Pa}$ for water. This is further corroborated by the high apparent receding contact angle $\theta^*_{rec} = 154°$ and low roll off angle $\omega = 5°$ of water on the mushroom-like pillar texture. Here, our emphasis is on the apparent receding contact angle because it is more sensitive to changes in the morphology than the apparent advancing contact angle.[60, 139-140]

Further, the Cassie-Baxter state is also evident from the visible pockets of air trapped beneath the water droplet (**Figure 2-5.e**). After heating the mushroom-like pillar texture above the glass transition temperature, deforming and cooling down to room temperature to form the collapsed pillar texture, when another droplet of water comes in contact with this collapsed pillar texture (**Figure 2-5.f**), it also adopts the Cassie-Baxter state because $P_{breakthrough} \approx 301\ \text{Pa} \gg P_{applied} = 116\ \text{Pa}$ (equation 2-8, along the diagonal direction of the collapsed pillar texture). Although the pockets of air underneath the droplet are not clearly visible, the Cassie-Baxter state is corroborated by the reasonably high apparent receding contact angle $\theta^*_{rec} = 141°$ and reasonably low roll off angle $\omega = 17°$ of water on the collapsed pillar texture. If the water droplet were to be in the Wenzel state, it would not roll off easily. The apparent receding contact angle is lower and the roll off angle is higher on the collapsed pillar texture because of the lower effective D/R (and correspondingly lower liquid-air area fraction f_{lv}) compared to the mushroom-like pillar texture.

Further, it is worth noting here that our MorphS surfaces possess texture on two length scales (see Figure 2-4.b) – the coarser length scale (mushroom-like pillar texture or collapsed pillar texture) and the finer length scale (bump-like texture between the coarser pillar texture). Consequently, when a pressure $P_{applied} > P_{breakthrough}$ for the collapsed pillar texture is applied on the water droplet, we anticipate that the droplet will adopt the "coarser-Wenzel state" (i.e., the droplet will wet the coarser collapsed pillar texture), but it may adopt a "finer-Cassie

state" (i.e., the droplet will not wet the finer bump-like texture) if $P_{applied} < P_{breakthrough,fine}$ for the finer texture. Based on equation (2-9), on the finer bump-like texture ($R_{fine} \approx 1$ μm, $D_{fine} \approx 3$ μm; Figure 2-2), the breakthrough pressure $P_{breakthrough,fine} \approx 3524$ Pa for water. So, we anticipate that water will adopt the Cassie-Baxter state if the applied pressure $P_{applied} < 3524$ Pa. Upon reheating the collapsed pillar texture above the glass transition temperature to recover the mushroom-like pillar texture, when yet another water droplet comes in contact with the recovered mushroom-like pillar texture, it adopts the Cassie-Baxter state (see **Figure 2-5.g**) virtually identical to the as-prepared mushroom-like pillar texture with high apparent receding contact angle $\theta^*_{rec} = 154°$ and low roll off angle $\omega = 6°$. The morphological transformations can be easily repeated on our MorphS surfaces to induce reversible wetting transitions of water droplets ex-situ (i.e., with different droplets) between Cassie-Baxter states of relatively lower adhesion and higher adhesion (see **Figures 2-5.k-l** and **2-5.l**).

Now, let us consider the wettability transitions of n-hexadecane, a representative low surface tension liquid, on our MorphS surfaces. When a droplet of n-hexadecane comes in contact with the as-prepared mushroom-like pillar texture, it adopts the Cassie-Baxter state because $P_{breakthrough} \approx 238$ Pa >> $P_{applied} = 44$ Pa for n-hexadecane. This is further corroborated by the high apparent receding contact angle $\theta^*_{rec} = 146°$ and low roll off angle $\omega = 7°$ of n-hexadecane on the mushroom-like pillar texture. Further, the Cassie-Baxter state is also evident from the visible pockets of air trapped beneath the n-hexadecane droplet (**Figure 2-5.h**). After heating the mushroom-like pillar texture above the glass transition temperature, deforming and cooling down to room temperature to form the collapsed pillar texture, when another droplet of n-hexadecane comes in contact with this collapsed pillar texture, it immediately adopts the Wenzel state (see **Figure 2-5.i**) due to lack of re-entrant texture, which is essential for a low

surface tension liquid to adopt the Cassie-Baxter state.[40, 57, 60, 141] This is further corroborated by the low apparent receding contact angle θ^*_{rec} = 10° and no roll off of n-hexadecane on the collapsed pillar texture. In addition to the "coarser-Wenzel state" on the collapsed pillar texture, we anticipate that the n-hexadecane droplet will adopt the "finer-Wenzel state" on the finer bump-like texture due to lack of re-entrant texture (i.e., a convex texture). This can be explained as follows: When a liquid droplet contacts a textured surface (with a texture angle ψ, Figure 2-2.b), it locally displays the Young's contact angle θ. A stable Cassie-Baxter is possible only if $\theta \geq \psi$. If $\theta < \psi$, the net traction on the triple phase contact line is downward, which promotes imbibition of the liquid into the solid texture, leading to a fully wetted Wenzel state.[3, 57-58, 68, 141] The finer bump-like texture of our MorphS surfaces possesses a texture angle $\psi \geq 90°$ (Figure 1-2.a). In other words, it does not have re-entrant texture (i.e., it does not have $\psi < 90°$). Consequently, low surface tension liquids (e.g., n-hexadecane with $\theta \approx \theta_{adv} = 79°$), which display a Young's contact angle $\theta < 90°$, completely wet the finer surface texture resulting in the Wenzel state. Upon reheating the collapsed pillar texture above the glass transition temperature to recover the mushroom-like pillar texture, when yet another n-hexadecane droplet comes in contact with the recovered mushroom-like pillar texture, it adopts the Cassie-Baxter state (see **Figure 2-5.j**) virtually identical to the as-prepared mushroom-like pillar texture with high apparent receding contact angle θ^*_{rec} = 147° and low roll off angle ω = 7°. The morphological transformations can be easily repeated on our MorphS surfaces to induce reversible wetting transitions of n-hexadecane droplets ex-situ between the Cassie-Baxter state and the Wenzel state (see Figures 2-5.k and 2-5.l). It is evident the ex-situ wetting transitions of n-hexadecane droplets are distinctly different from those of the water droplets.

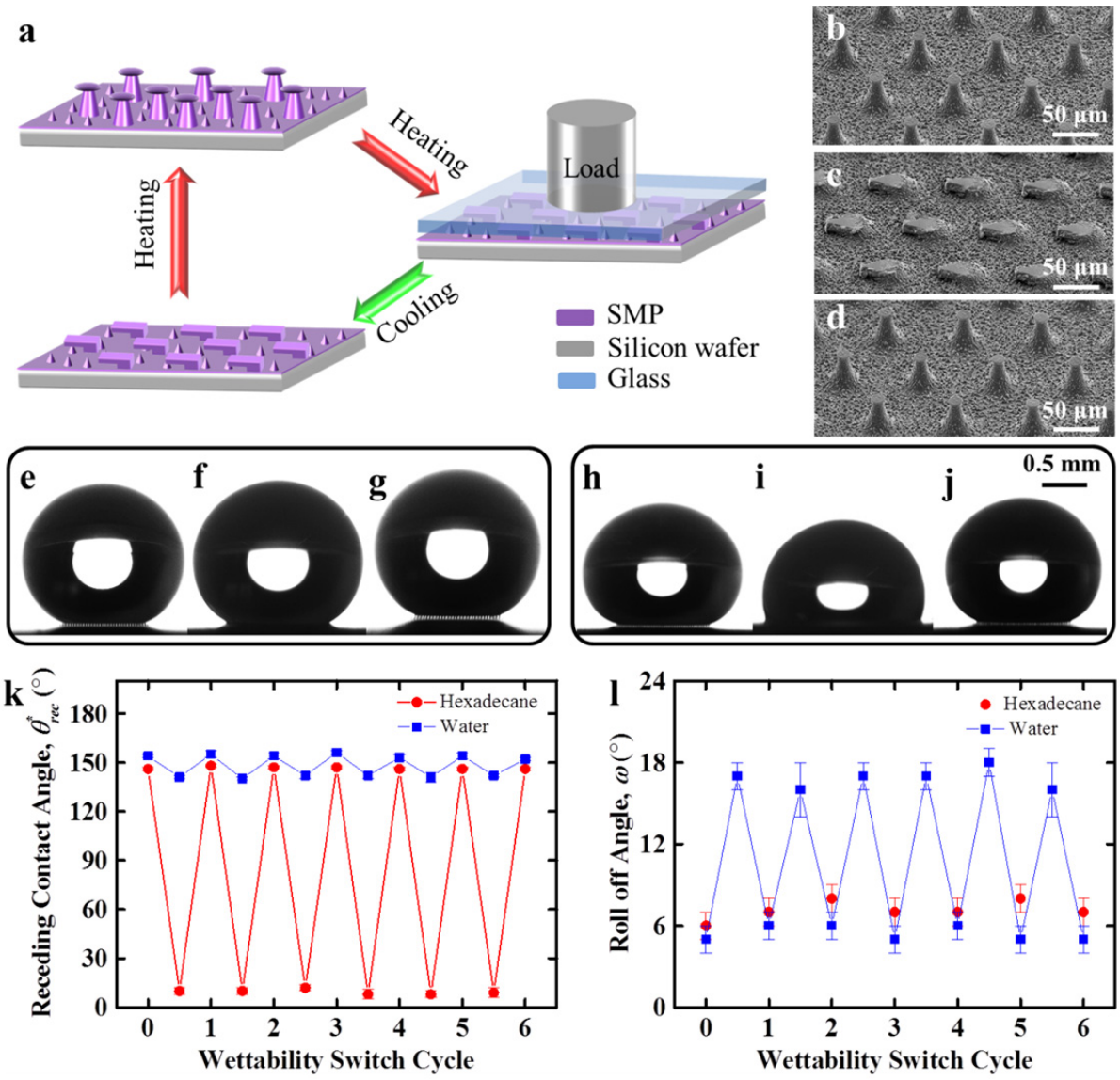

FIGURE 2-5. Switchable wettability (ex situ). (a) Schematic depicting the reversible morphology transformation between the mushroom-like pillar texture and the collapsed pillar texture. **(b–d)** SEM images showing the as-prepared mushroom-like pillar texture, the collapsed pillar texture, and the recovered mushroom-like pillar texture, respectively. **(e–g)** Droplets of water on the as-prepared mushroom-like pillar texture, the collapsed pillar texture, and the recovered mushroom-like pillar texture, respectively. **(h–j)** Droplets of n-hexadecane on the as-prepared mushroom-like pillar texture, the collapsed pillar texture, and the recovered mushroom-like pillar texture, respectively. **(k,l)** A few representative cycles showing changes in the apparent receding contact angles and the roll off angles, respectively, of water and n-hexadecane droplets (≈8 μL) due to changes in morphology of the texture.

In addition to ex-situ wetting transitions, we have also investigated in-situ (i.e., with the same droplet) wetting transitions on our MorphS surfaces when the morphology transforms from

the collapsed pillar texture to the mushroom-like pillar texture. As described previously, when a water droplet comes in contact with the collapsed pillar texture at room temperature, it adopts a relatively high adhesion Cassie-Baxter state with a roll off angle $\omega = 17^{\circ}$. In this state, the pockets of air underneath the water droplet are not clearly visible (see **Figure 2-6.a**). When the surface is heated above the glass transition temperature, with the water droplet in continuous contact, the morphology begins to transform into the mushroom-like pillar texture. During this morphological transformation, the elastic energy stored within the collapsed pillars lifts the water droplet from the height of the shorter collapsed pillars to the height of the taller mushroom-like pillars. Simultaneously, the water droplet continues to adopt newer Cassie-Baxter states due to increasing f_{lv}, eventually reaching a relatively low adhesion Cassie-Baxter state with a roll off angle $\omega = 6^{\circ}$. As a result, the pockets of air underneath the water droplet become increasingly visible during this morphological transformation (see Figure 2-6.a). This in-situ wetting transition of water droplets from a high adhesion Cassie-Baxter state to a low adhesion Cassie-Baxter state accompanying the morphological transformation from the collapsed pillar texture to the mushroom-like pillar texture is highly reproducible on our MorphS surfaces.

A careful inspection of the water droplet during the in-situ wetting transition indicates that the droplet volume decreases from ~8 μL to ~5 μL. In order to ensure that the in-situ wetting transition to the low adhesion Cassie-Baxter state is entirely due to morphological transformation and not due to the water vapor simultaneously generated, we conducted our in-situ wetting transition experiments with a lower vapor pressure liquid, formamide (boiling point $T_{boiling}$ = 210°C, γ_{lv} = 58.2 mN/m, ρ = 1130 kg/m^3).

Similar to a water droplet, when a formamide droplet comes in contact with the collapsed pillar texture at room temperature, it adopts a high adhesion Cassie-Baxter state with a roll off

angle $\omega = 30°$ and no visible air pockets underneath the formamide droplet (see **Figure 2-6.b**). Upon heating the surface above the glass transition temperature, the morphological transformation lifts up the formamide droplet, which eventually adopts a low adhesion Cassie-Baxter state with a roll off angle $\omega = 6°$ and clearly visible air pockets (see Figure 2-6.b). There is virtually no change in droplet volume accompanying this in-situ wetting transition indicating that the influence (if any) of the vapor generated due to heating is insignificant. Unlike water and formamide, we did not observe an in-situ wetting transition of n-hexadecane on our MorphS surfaces because the energy barrier to overcome both the finer-Wenzel state and the coarser-Wenzel state and eventually transition to the Cassie-Baxter state is too high.

The wetting transitions on our MorphS surfaces can be used to design rewritable liquid patterns. To demonstrate this, we heated our MorphS surfaces above the glass transition temperature, deformed it using a stamp to create a "UTD" pattern of collapsed pillars and cooled the surface down to room temperature. When droplets of n-hexadecane are deposited everywhere on this patterned surface, they adhered to the deformed collapsed pillar texture (Wenzel state) and rolled off easily from the undeformed mushroom-like pillar texture (Cassie-Baxter state) to result in a "UTD" liquid pattern (**Figure 2-6.c**). In order to erase this pattern and recover our MorphS surface, we washed the n-hexadecane liquid pattern on the surface with acetone, blow dried the surface, and then reheated the surface above glass transition temperature. Subsequently, to rewrite a new liquid pattern, we reheated the erased MorphS surface above the glass transition temperature, deformed it using a new stamp to create a "CSU" pattern of collapsed pillars, and cooled the surface down to room temperature. When droplets of n-hexadecane are deposited everywhere on this new patterned surface, they resulted in a "CSU" liquid pattern (**Figure 2-6.d**). In this manner, our MorphS surfaces can be reused to write different liquid patterns.

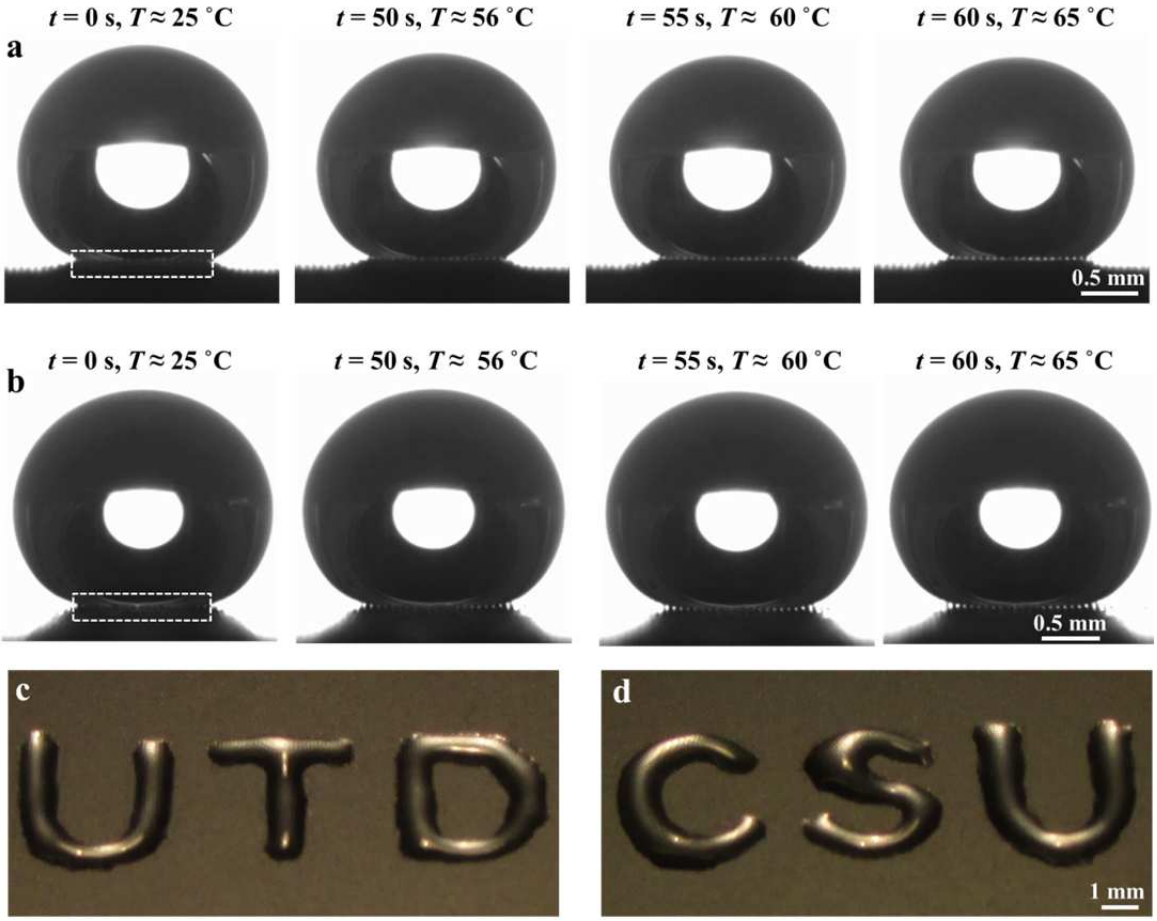

FIGURE 2-6. Switchable wettability (in situ). (a,b) Wetting transition of a water droplet and a formamide droplet, respectively, when the morphology transforms from the collapsed pillar texture to the mushroom-like pillar texture upon heating the surface from room temperature (*RT*) to above the glass transition temperature within 1 min. **(c,d)** Images illustrating the rewritable liquid patterns on our MorphS surfaces.

2.1.5. Conclusions

In summary, we fabricated the metamorphic superomniphobic (MorphS) surfaces with a thermo-responsive SMP and demonstrated the distinctly different wetting transitions of liquids with different surface tensions and elucidated the underlying physics. We believe that the reversible wetting transitions on our robust MorphS surfaces will have a wide range of applications including rewritable liquid patterns, controlled drug release systems, liquid-liquid separation membranes, lab-on-a-chip devices, and biosensors. Further, we envision remotely and reversibly actuated MorphS surfaces (e.g., surfaces with completely thermally driven

morphological transition without any mechanical intervention) can be easily fabricated by utilizing liquid crystal elastomers[142-143] or two-way SMPs[144-145].

2.2. Coalescence Induced Self-Propulsion of Droplets on Superomniphobic Surfaces

Summary: We utilized superomniphobic surfaces to systematically investigate the different regimes of coalescence-induced self-propulsion of liquid droplets with a wide range of droplet radii, viscosities and surface tensions (**published in ACS applied materials & interfaces, 2017**). Our results indicate that the non-dimensional jumping velocity V_j^* is nearly constant ($V_j^* \approx 0.2$) in the inertial-capillary regime and decreases in the visco-capillary regime as the Ohnesorge number Oh increases. Within the visco-capillary regime, decreasing the droplet radius R_0 results in a more rapid decrease in the non-dimensional jumping velocity V_j^* compared to increasing the viscosity μ. This is because decreasing the droplet radius R_0 increases the inertial-capillary velocity V_{ic} in addition to increasing the Ohnesorge number Oh. We envision that our work will enhance the fundamental understanding of coalescence-induced self-propulsion in the inertial-capillary regime and the visco-capillary regime.

2.2.1. Introduction

As described in chapter one, when two liquid droplets coalesce on a super-repellent surface, the presence of a super-repellent surface breaks the symmetry of coalescence. This results in a velocity component normal to the plane of coalescence and away from the super-repellent surface for the coalesced droplet. The negligible adhesion to the super-repellent surface allows the coalesced droplet to self-propel (or jump) away from the super-repellent surface at a jumping velocity V_j.[4, 8, 111-116] Such coalescence-induced self-propulsion of droplets has been reported on a variety of natural water-repellent surfaces, including lacewings and cicadas,[17, 146] and has attracted significant attention due to its applications in sustained dropwise condensation[147-157] as well as anti-icing,[27, 158] and self-cleaning[17] surfaces.

Consider two small liquid droplets with radii R_0, density ρ, viscosity μ, and surface tension γ_{lv}, such that the Bond number $Bo = \rho g R_0^2 / \gamma_{lv} < 1$ (i.e., gravity can be neglected).[111] When these two liquid droplets coalesce on a super-repellent surface, with negligible adhesion, the excess surface energy released is either lost due to viscous dissipation or converted to the kinetic energy of the jumping droplet.[4, 8, 111-113, 159] A scaling argument based on the energy balance can be written as:

$$C_1\gamma_{lv}R_0^2 - C_2\mu\sqrt{\frac{\gamma_{lv}R_0^3}{\rho}} \sim \rho R_0^3 V_j^2 \tag{2-10}$$

In equation 2-10, the term on the left represents the excess surface energy released, the first term on the right represents the viscous dissipation[160] and the second term on the right represents the kinetic energy of the jumping droplet.[4, 8, 111-113, 159] Recognizing that the Ohnesorge number[4, 8, 111-113] $Oh = \mu/\sqrt{\rho\gamma_{lv}R_0}$ and the inertial-capillary velocity[4, 8, 111-113] $V_{ic} = \sqrt{\gamma_{lv}/\rho R_0}$, equation 2-10 can be rewritten in the non-dimensional form as:

$$V_j^* = \frac{V_j}{V_{ic}} \sim \sqrt{C_1 - C_2 Oh} \tag{2-11}$$

Here, V_j^* is the non-dimensional jumping velocity. The Ohnesorge number *Oh* can be understood as the ratio of the visco-capillary time scale ($t_{vc} \sim \mu R_0/\gamma_{lv}$) and the inertial-capillary time scale ($t_{ic} \sim \sqrt{\rho R_0^3/\gamma_{lv}}$), indicating the relative importance of the viscosity compared to fluid inertia and surface tension.[4, 161]

Prior work has identified different regimes of coalescence-induced self-propulsion of droplets on super-repellent surfaces by investigating the scaling of the non-dimensional jumping velocity V_j^* as a function of the Ohnesorge number *Oh*.[4, 8, 111-112] In the inertial-capillary regime, the influence of viscous dissipation is negligible (i.e., $Oh << 1$) and the non-dimensional jumping velocity V_j^* was found to be nearly constant,[4, 8, 110-114, 162-163] as evident from equation 2-11. In the visco-capillary regime (i.e., higher *Oh*), viscous dissipation increases with increasing Ohnesorge number *Oh* and correspondingly the non-dimensional jumping velocity V_j^* decreases,[4, 111-113] as evident from equation 2-11. At very high Ohnesorge number *Oh*, the released excess surface energy is completely consumed by viscous dissipation and $V_j^* \to 0$, i.e., the droplet cannot jump away from the surface.[4, 111-112]

It is evident from the discussion above that the non-dimensional jumping velocity V_j^* is a function of Ohnesorge number *Oh*. The Ohnesorge number *Oh* can be tuned by altering the liquid viscosity μ, surface tension γ_{lv} or the droplet radius R_0. All prior reports have employed water droplets of different radii R_0 on superhydrophobic surfaces to investigate the different regimes of coalescence-induced self-propulsion.[4, 111, 160] To the best of our knowledge, there are no reports that have employed liquids with a wide range of surface tensions γ_{lv} or wide range of viscosities μ to investigate the different regimes of coalescence-induced self-propulsion. This is partly due to the inability of superhydrophobic surfaces to repel low surface tension liquids. In this work,[118] we utilized superomniphobic surfaces (i.e., surfaces extremely repellent to both high surface tension liquids like water and low surface tension liquids like oils and alcohols) to overcome this limitation. Utilizing superomniphobic surfaces, we experimentally investigated the different regimes of coalescence-induced self-propulsion for liquid droplets with a range of (i) droplet radii ($R_0 \approx$ 450 μm to 760 μm), (ii) viscosities ($\mu \approx$ 1 mPa.s to 220 mPa.s), and (iii) surface tensions ($\gamma_{lv} \approx$ 40 mN m^{-1} to 72 mN m^{-1}). Further, in order to study the different regimes of coalescence-induced self-propulsion well beyond the limited range of droplet radius, viscosity and surface tension accessible in our experiments, we also conducted numerical simulations (see **Section 2.2.3**) for a wide range of (i) droplet radii ($R_0 \approx$ 5 μm to 760 μm), (ii) viscosities ($\mu \approx$ 1 mPa.s to 220 mPa.s), and (iii) surface tensions ($\gamma_{lv} \approx$ 10 mN m^{-1} to 400 mN m^{-1}). We envision that our work will enhance the fundamental understanding of coalescence-induced self-propulsion in the inertial-capillary regime and the visco-capillary regime.

2.2.2. Fabrication and Characterization

We fabricated hierarchically structured (i.e., a finer length scale texture superimposed on an underlying coarser length scale texture), re-entrant textured, superomniphobic surfaces by

conformally spray coating stainless steel wire meshes (coarser texture) with blends of fluorodecyl POSS and super-fast instant adhesive SF100 (finer texture).

Spray coating the blends of fluorodecyl POSS and super-fast instant adhesive SF100 (i.e., finer length scale texture) on an underlying wire mesh (i.e., coarser length scale texture, **Figure 2-7.a** inset) resulted in a hierarchical structure. The key parameter influencing the surface texture (and hence superomniphobicity) is the volume of spray coating solution V_{spray}. In order to systematically investigate the influence of V_{spray} on wetting, we fabricated surfaces using different V_{spray} and measured the advancing contact angle, the receding contact angle and the roll off angle of droplets of n-hexadecane (a representative liquid with low surface tension, $\gamma_{lv} \approx 27.5$ mN m^{-1}).

Our results (Figure 2-7a and insets) indicate that at low V_{spray}, the surface coverage is insufficient to render the surface superomniphobic. At $V_{spray} \approx$ 25-35 ml, the sufficient surface coverage, hierarchical structure, re-entrant texture and the low solid surface energy ($\gamma_{sv} \approx 10$ mN m^{-1})[60] led to a robust Cassie-Baxter state and rendered our surfaces superomniphobic for a wide variety of liquids with surface tension $\gamma_{lv} \geq 27.5$ mN m^{-1}. Further increase in V_{spray} results in clogging of the wire mesh pores that reduces the liquid-air area fraction, which in turn reduces the superomniphobicity.[3, 38, 40, 46, 60, 164] Based on these results, we fabricated our superomniphobic surfaces with $V_{spray} \approx 30$ ml for all the results discussed below. The high liquid-air area fraction in the Cassie-Baxter state resulted in high apparent contact angles θ^* and low contact angle hysteresis $\Delta\theta^*$ for a wide range of liquids (see **Figure 2-7.b,** also see CH. 2-2 Supplementary Information) on our superomniphobic surfaces. Further, the super-repellency of our surfaces is also evident from an impinging water droplet (with Weber number, $We = \rho R_0 V_j^2 / \gamma_{lv} \approx 0.3$) rebounding back with a restitution coefficient ε (i.e., ratio of the velocity

of a droplet after and before it impacts a surface)[165-166] that is very high ($\varepsilon > 0.95$; see **Figure 2-7.c**).

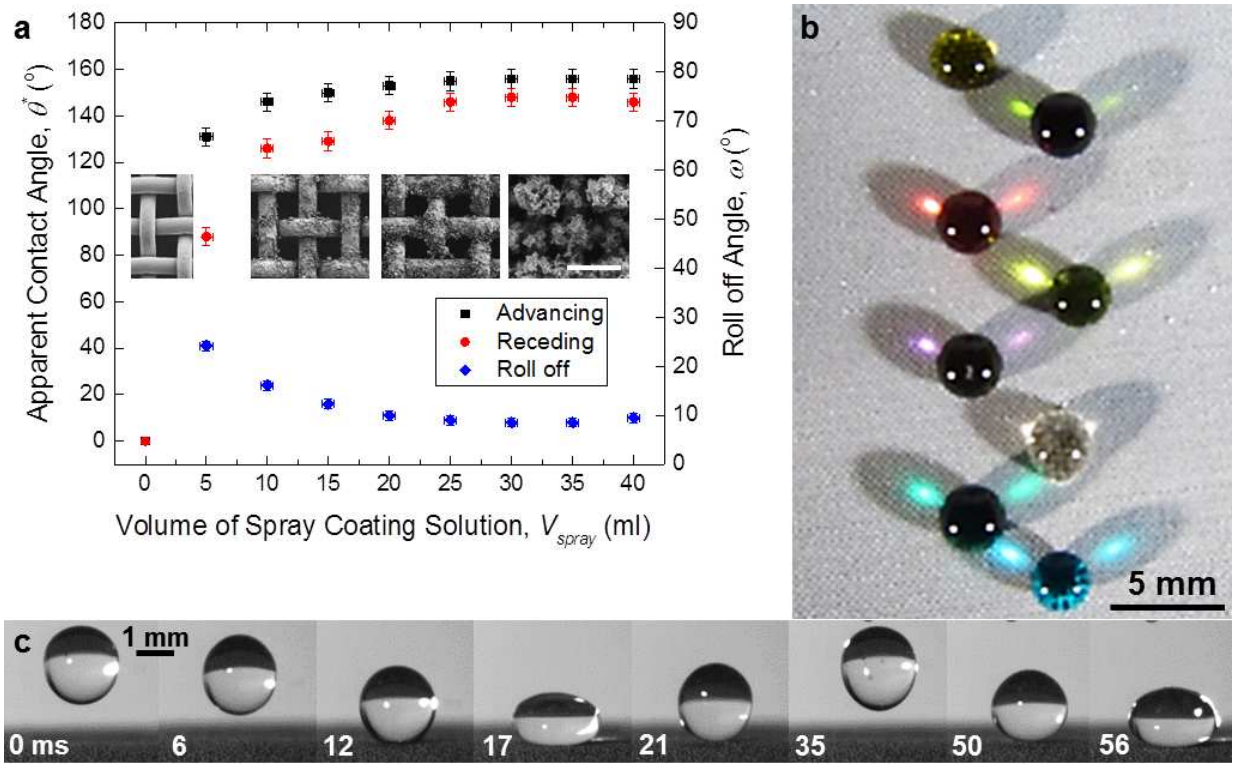

FIGURE 2-7. Characterization of our superomniphobic surface. (a) Influence of the volume of spray coating solution (V_{spray}) on the apparent contact angles and the roll-off angles of n-hexadecane. Insets (left to right) show SEM images of surfaces with $V_{spray} \approx 0$, 10, 20 and 30 ml, respectively. Scale bar represents 50 μm. **(b)** Droplets from bottom to top: water ($\gamma_{lv} \approx 72$ mN/m), glycerol ($\gamma_{lv} \approx 64$ mN/m), 1 mM SDS in water ($\gamma_{lv} \approx 67$ mN/m), 1.5 mM SDS in water ($\gamma_{lv} \approx 61$ mN/m), 2 mM SDS in water ($\gamma_{lv} \approx 56$ mN/m), 3 mM SDS in water ($\gamma_{lv} \approx 46$ mN/m), 6 mM SDS in water ($\gamma_{lv} \approx 40$ mN/m), and n-hexadecane ($\gamma_{lv} \approx 27.5$ mN/m) showing very high apparent contact angles on the surface. **(c)** A series of snapshots showing a bouncing water droplet (with restitution coefficient, $\varepsilon > 0.95$) on our superomniphobic surface.

2.2.3. Numerical Model

We implemented 3D numerical simulations with an incompressible, laminar flow model to capture the evolution of the liquid-air interface during the coalescence of two identical liquid droplets (radius R_0) at rest on a superomniphobic surface.[167-168] Prior work[4, 8, 111, 114, 160] has employed smooth surfaces in their numerical simulations and found reasonable agreement with

experiments that employed textured super-repellent surfaces. Similar to prior work,[4, 8, 111, 114, 160] we also employed smooth surfaces (with perfectly smooth wall boundary conditions) with known contact angles (i.e., $\theta^* \approx (\theta^*_{adv} + \theta^*_{rec})/2$; see CH. 2-2 Supplementary Information), to define the superomniphobic surfaces in our simulations. We observed a reasonable agreement between our experimental results (based on textured surfaces) and our numerical results (based on smooth surfaces). Further, prior work[111] has reported that the influence of solid-liquid adhesion on coalescence-induced jumping velocity V_j of droplets on super-repellent surfaces is negligible, if the contact angle hysteresis low (i.e., $\Delta\theta^* < 10°$). Hence, we ignored the contact angle hysteresis at the lower boundary of the computational domain (i.e., $z = 0$), representing the superomniphobic surface (**Figure 2-8**). The two droplets were initially situated with overlapping diffuse interfaces that led to the onset of coalescence.[4, 111, 169-170] Due to the symmetry in the x- and y- directions, only half of each coalescing droplet was simulated in a computational domain of $6R_0 \times 6R_0 \times 10\ R_0$ (see Figure 2-8).[4, 111] Symmetric boundary conditions were used at the planes $x = 0$ and $y = 0$.[111, 168] We solved the governing equations (equation of continuity and momentum equation) with ANSYS Fluent (i.e., a CFD-based commercial software) using a pressure-based solver.[168] The geometric reconstruction scheme was used in the VOF (volume of fluid) model[171-173] to represent the liquid-air interface, with a piecewise-linear approach. Further, we used the CSF (continuum surface force) method, with surface tension as the source term in the momentum equation. The momentum equation was discretized using the second-order upwind scheme.[168] We used the SIMPLE (semi implicit, explicit) algorithm for pressure-velocity coupling and fluid properties were updated from the pressures using the PISO (pressure implicit with splitting of operators) algorithm.[168] Since $Bo = \rho g R_0^2/\gamma_{lv} < 0.1$ in all our experiments and virtually all our simulations, we ignored the role of gravity in our simulations.[111, 160] A mesh with

> 40 cells per radius was employed within the droplet.[170, 174] Further, local mesh refinement was performed close to the lower boundary of the computational domain (i.e., $z \rightarrow 0$) and close to the symmetric planes (i.e., $x \rightarrow 0$ and $y \rightarrow 0$), to mitigate the influence of high gradients (see Figure 2-8). A mesh-independence check was performed to confirm that the numerical results were virtually insensitive to further mesh refinement. A time step $\Delta t < 10^{-6}$ was used in all cases to ensure CFL (Courant-Friedrich-Levy number)[167-168] < 0.8. Iterations at each time step were terminated when the convergence criteria of all equations was smaller than 10^{-6}.

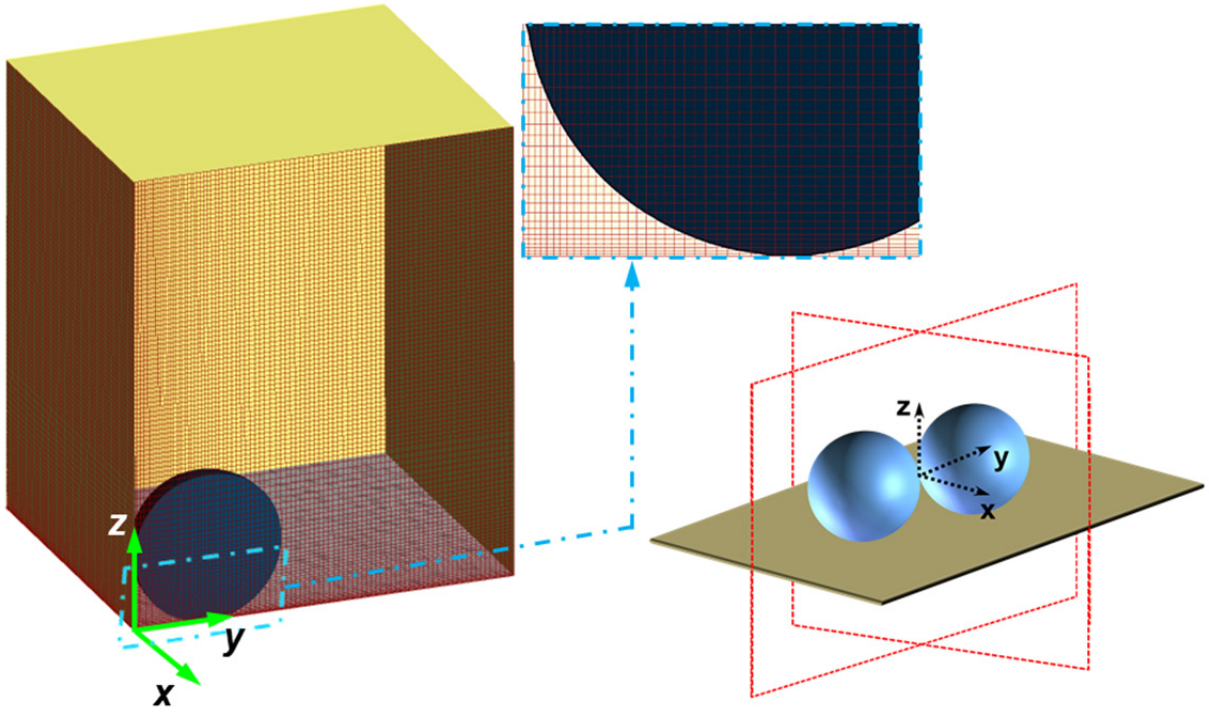

FIGURE 2-8. Computational domain. Half of a coalescing droplet (radius R_0) resting on a superomniphobic surface (at $z = 0$) in a computational domain of volume 6 R_0×6 R_0×10 R_0. Finer mesh was used close to the lower boundary of the computational domain (i.e., $z \rightarrow 0$) and close to the symmetric planes (i.e., $x \rightarrow 0$ and $y \rightarrow 0$) to mitigate the influence of high gradients.

2.2.4. Results and Discussion

Utilizing our superomniphobic surfaces, we systematically investigated the different regimes of coalescence-induced self-propulsion for – (i) droplets of water with different radii (R_0

≈ 450 μm to 760 μm in experiments and R_0 ≈ 5 μm to 760 μm in numerical simulations), but constant surface tension and viscosity, (ii) droplets of water containing different compositions of glycerol with different viscosities (μ ≈ 1 mPa s to 220 mPa s in both experiments and numerical simulations), but approximately constant droplet radius and surface tension, and (iii) droplets of water containing different concentrations of sodium dodecyl sulfate (SDS) with different surface tensions (γ_{lv} ≈ 40 mN m^{-1} to 72 mN m^{-1} in experiments and γ_{lv} ≈ 10 mN m^{-1} to 400 mN m^{-1} in numerical simulations), but approximately constant droplet radius and viscosity (see CH. 2-2 Supplementary Information).

In order to compare coalescence-induced self-propulsion on superomniphobic surfaces with prior reports on superhydrophobic surfaces as well as to compare our experimental results with our numerical results, we first investigated the coalescence-induced self-propulsion of water droplets with different radii (R_0 ≈ 450 μm to 760 μm for experiments and R_0 ≈ 4 μm to 760 μm for numerical simulations), but constant surface tension (γ_{lv} ≈ 72 mN m^{-1}) and viscosity (μ ≈ 1 mPa s), to result in a range of Ohnesorge numbers (Oh ≈ 0.003 to 0.004 for experiments and Oh ≈ 0.003 to 0.06 for numerical simulations). Our numerical simulations (**Figure 2-9.a** and **2-9.b**) indicate an inertial-capillary regime for droplet radius R_0 > 20 μm (i.e., Oh < 0.02) and a visco-capillary regime for droplet radius R_0 < 20 μm (i.e., Oh > 0.02).

In the inertial-capillary regime, the jumping velocity V_j decreases with increasing droplet radius R_0. This is because the jumping velocity is expected to scale as the inertial-capillary velocity (i.e., $V_j \sim V_{ic}$),[4, 8, 111] which decreases with increasing droplet radius R_0. Further, the nearly constant non-dimensional jumping velocity V_j^* ≈ 0.2 in the inertial-capillary regime (i.e., Oh < 0.02) indicates negligible viscous dissipation (also see equation 2-11). In the visco-capillary regime, the jumping velocity V_j decreases rapidly with decreasing droplet radius R_0.

Correspondingly, the non-dimensional jumping velocity V_j^* decreases rapidly with increasing Ohnesorge number Oh (as evident from equation 2-11). At a sufficiently high Ohnesorge number, $Oh \rightarrow 0.05$, the non-dimensional jumping velocity $V_j^* \rightarrow 0$ and the coalesced droplet no longer jumps away from the superomniphobic surface.

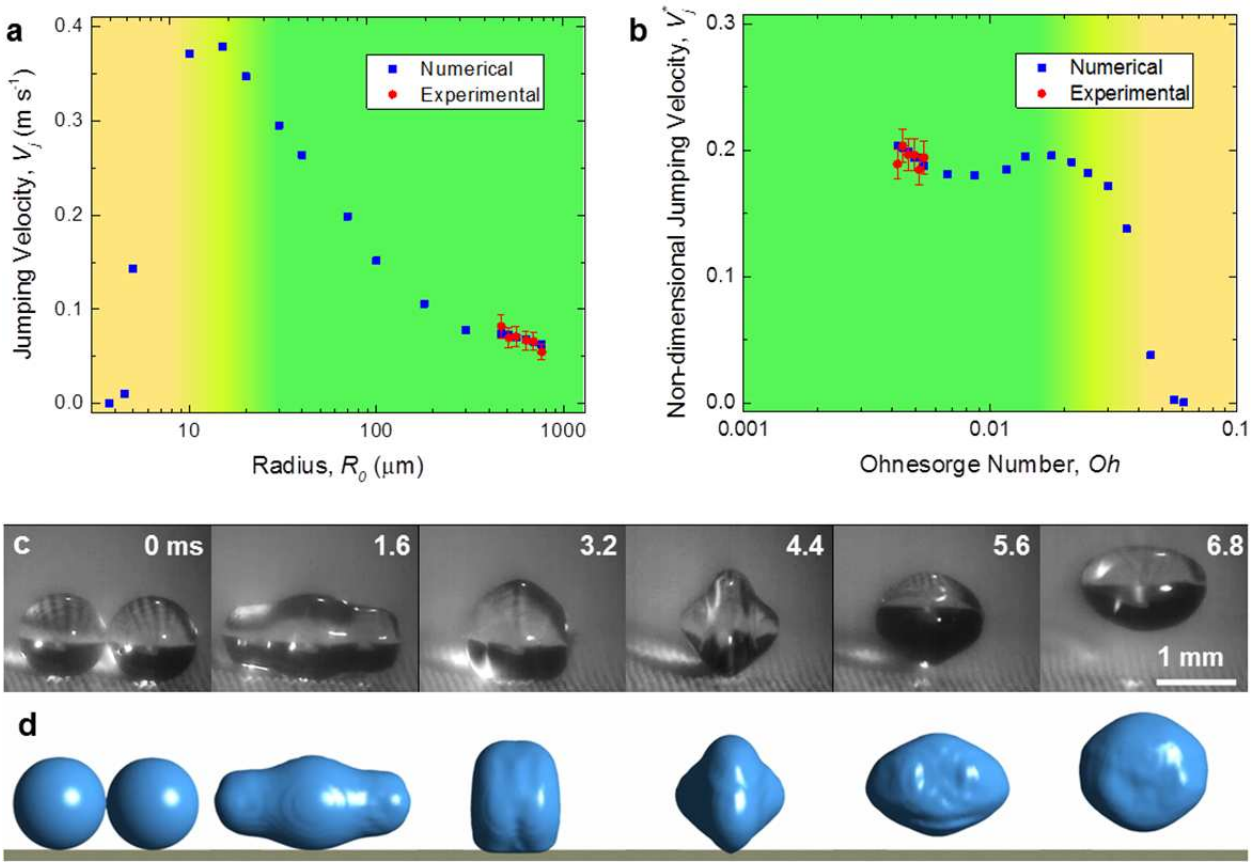

FIGURE 2-9. Coalescence-induced self-propulsion of water droplets on a superomniphobic surface. (a) Jumping velocity V_j as a function of the droplet radius R_0. **(b)** Non-dimensional velocity V_j^* as a function of the Ohnesorge number Oh. In (a) and (b), inertial-capillary and visco-capillary regimes are shown in green and yellow, respectively. **(c)** and **(d)** Series of snapshots from experiments and numerical simulations, respectively ($R_0 \approx 550$ μm). The time difference between the experimental and corresponding numerical frames is negligible (< 0.2 ms).

A series of snapshots of the coalescence-induced self-propulsion of two droplets of water ($R_0 \approx 550$ μm) indicate that our experimental results (**Figure 2-9.c**) match reasonably well with our numerical simulations (**Figure 2-9.d**). Further, both our experiments and numerical simulations agree well with prior work.[4, 111, 160]

We have also investigated the coalescence-induced self-propulsion of droplets of water containing different compositions of glycerol, with different viscosities ($\mu \approx$ 1 mPa s to 220 mPa s for both experiments and numerical simulations), but approximately constant droplet radius (R_0 $\approx$ 620 μm) and surface tension ($\gamma_{lv} \approx$ 72 mN m^{-1} to 65 mN m^{-1}), to result in a wide range of Ohnesorge numbers ($Oh \approx$ 0.003 to 0.7 for both experiments and numerical simulations). Our experiments as well as numerical simulations (**Figure 2-10.a** and **2-10.b**) indicate an inertial-capillary regime for viscosity $\mu <$ 20 mPa.s (i.e., $Oh <$ 0.05) and a visco-capillary regime for viscosity $\mu >$ 20 mPa.s (i.e., $Oh >$ 0.05). In the inertial-capillary regime, the jumping velocity V_j (which is expected to scale as the inertial-capillary velocity V_{ic}) [4, 8, 111] decreases slightly with increasing composition of glycerol in water because of the decrease in surface tension and increase in density (see CH. 2-2 Supplementary Information), but not due to the increase in viscous dissipation associated with increase in viscosity. This negligible viscous dissipation with increasing Ohnesorge number Oh in the inertial-capillary regime is also evident from the nearly constant non-dimensional jumping velocity $V_j^* \approx 0.2$ (also see equation 2-11).

In the visco-capillary regime, the jumping velocity V_j decreases with increasing viscosity μ and correspondingly the non-dimensional jumping velocity V_j^* decreases with increasing Ohnesorge number Oh (as evident from equation 2-11). This is because as viscosity μ increases and Ohnesorge number Oh increases, the viscous dissipation increases significantly. At a sufficiently high Ohnesorge number, $Oh \rightarrow 0.38$, the non-dimensional jumping velocity $V_j^* \rightarrow 0$ and the coalesced droplet no longer jumps away from the superomniphobic surface. A series of snapshots of the coalescence-induced self-propulsion of two droplets of water + 85% glycerol (μ $\approx$ 109 mPa s) indicate that our experimental results (**Figure 2-10.c**) match reasonably well with our numerical simulations (**Figure 2-10.d**).

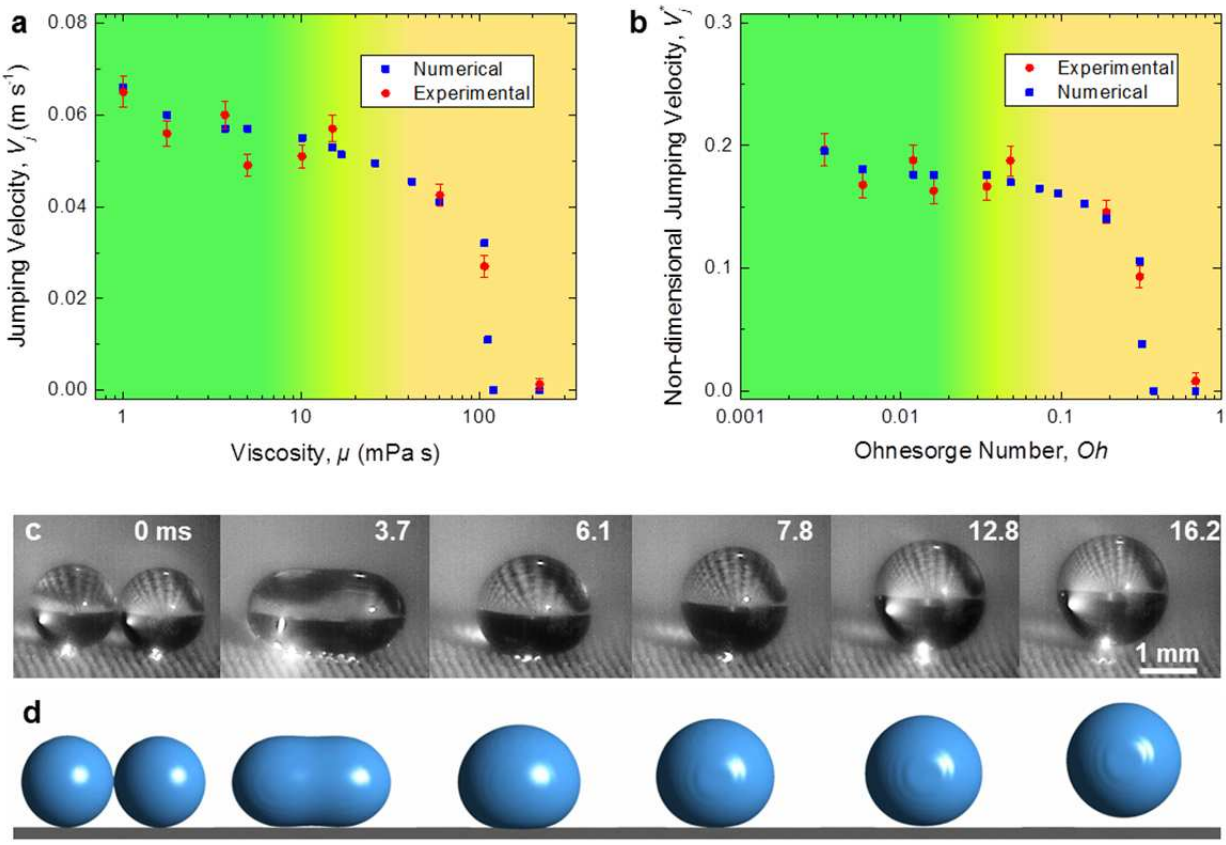

FIGURE 2-10. Coalescence-induced self-propulsion of water+glycerol droplets on a superomniphobic surface. (a) Jumping velocity V_j as a function of the viscosity μ. **(b)** Non-dimensional velocity V_j^* as a function of the Ohnesorge number Oh. In (a) and (b), inertial-capillary and visco-capillary regimes are shown in green and yellow, respectively. **(c)** and **(d)** Series of snapshots from experiments and numerical simulations, respectively ($\mu \approx$ 109 mPa.s). The time difference between the experimental and corresponding numerical frames is negligible (< 0.2 ms).

Utilizing our superomniphobic surfaces, we have also investigated the coalescence-induced self-propulsion of droplets of water containing different concentrations of SDS, with different surface tensions ($\gamma_{lv} \approx$ 72 mN m^{-1} to 40 mN m^{-1} for experiments and $\gamma_{lv} \approx$ 400 mN m^{-1} to 10 mN m^{-1} for numerical simulations), but approximately constant droplet radius ($R_0 \approx$ 710 μm) and viscosity ($\mu \approx$ 1 mPa.s), to result in a range of Ohnesorge numbers ($Oh \approx$ 0.003 to 0.004 for experiments and $Oh \approx$ 0.0009 to 0.009 for numerical simulations). We have limited our numerical simulations to surface tension $\gamma_{lv} \geq$ 10 mN m^{-1} because there are no known liquids

with surface tension γ_{lv} <10 mN m^{-1} (at room temperature and atmospheric pressure).[175-176] Recent work[177-179] has demonstrated that when two similar droplets containing the same surfactant with equal concentrations coalesce, the temporal gradients in the surface tension (due to reconfiguration of the surfactant) disappear very quickly and do not influence the dynamic coalescence process significantly. Consequently, in our experiments with two nearly identical droplets with the same concentration of SDS, we do not anticipate a significant influence of the surface tension gradients on the coalescence process and the coalescence-induced jumping velocity V_j. Our results (**Figure 2-11.a** and **2-11.b**) indicate that the coalescence-induced self-propulsion of droplets with $R_0 \approx 710$ μm over the entire range of surface tension studied (i.e., 10 mN m^{-1} < γ_{lv} < 400 mN m^{-1}) lies in the inertial-capillary regime (i.e., negligible viscous dissipation), with a constant non-dimensional velocity $V_j^* \approx 0.2$ (also see equation 2-11). The jumping velocity V_j increases with increasing surface tension, as might be anticipated from its scaling with the inertial-capillary velocity V_{ic}.[4, 8, 111]

A series of snapshots of the coalescence-induced self-propulsion of two droplets of 6 mM SDS in water ($\gamma_{lv} \approx 40$ mN m^{-1}) indicate that our experimental results (**Figure 2-11.c**) match reasonably well with our numerical simulations (**Figure 2-11.d**). Negligible influence of the surface tension gradients on the coalescence process and the coalescence-induced jumping velocity V_j is further corroborated by the agreement between our numerical simulations (that do not consider the presence of surfactants) and our experimental results.

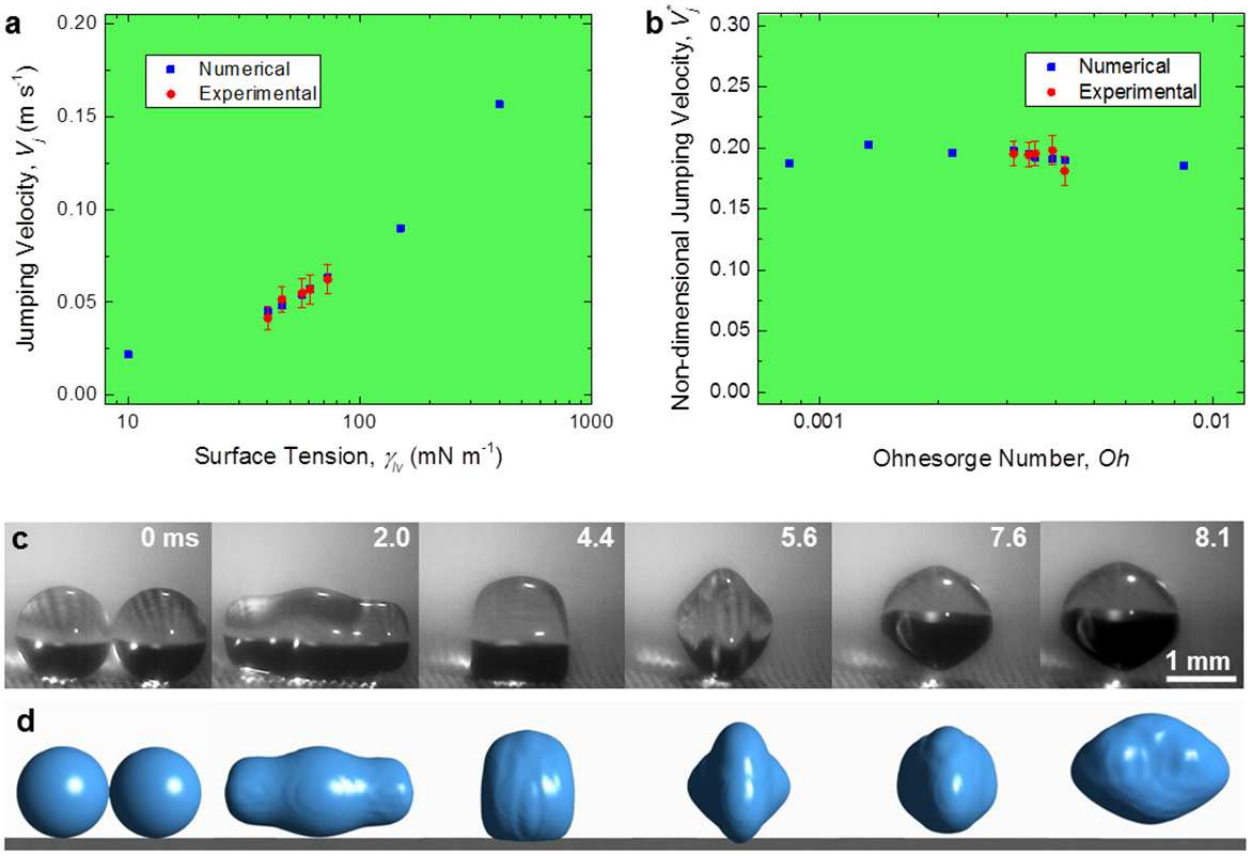

FIGURE 2-11. Coalescence-induced self-propulsion of SDS in water droplets on a superomniphobic surface. **(a)** Jumping velocity V_j as a function of the surface tension γ_{lv}. **(b)** Non-dimensional velocity V_j^* as a function of the Ohnesorge number Oh. In (a) and (b), inertial-capillary regime is shown in green. **(c)** and **(d)** Series of snapshots from experiments and numerical simulations, respectively ($\gamma_{lv} \approx 40$ mN/m). The time difference between the experimental and corresponding numerical frames is negligible (< 0.2 ms).

Prior reports[4, 8, 111-113] on coalescence-induced self-propulsion of droplets indicate that the transition from the inertial-capillary regime to the visco-capillary regime (which approximately corresponds to the maximum V_j with decreasing R_0) occurs over a wide range of R_0 (i.e., 0.1 μm < R_0 < 50 μm) and correspondingly a wide range of Oh (i.e., 0.006 < Oh < 0.22). This wide range can be attributed to the differences in the Young's contact angles, the apparent contact angles, the contact angle hystereses and the length scales of surface texture employed in the experiments or assumed in numerical simulations.[4, 111] Our results indicate that the transition from the inertial-capillary regime to the visco-capillary regime occurs at $R_0 \approx 20$ μm (Figure

2.9a) and $0.02 < Oh < 0.05$ (Figures 2.9b and 2.10b), which is within the wide range reported in prior work.

More importantly, our results indicate that in the visco-capillary regime, the non-dimensional jumping velocity V_j^* decreases more rapidly with increasing Ohnesorge number Oh due to decreasing droplet radius R_0 (**Figure 2-12**) than increasing the Ohnesorge number Oh due to increasing viscosity μ (Figure 2-12). We explain this as follows – increasing the viscosity μ, and correspondingly increasing the Ohnesorge number Oh, results in a decrease in the non-dimensional jumping velocity V_j^*, as evident from equation 2-11. However, as the radius R_0 decreases, in addition to increasing the Ohnesorge number Oh, the inertial-capillary velocity V_{ic} also increases. Both the increase in Ohnesorge number Oh and the increase in inertial-capillary velocity V_{ic} (i.e., two different factors) contribute to a decrease in the non-dimensional jumping velocity V_j^*, as evident from equation 2-11. Correspondingly, the non-dimensional jumping velocity V_j^* decreases more rapidly with increasing Ohnesorge number Oh (and increasing inertial-capillary velocity V_{ic}) due to decreasing droplet radius R_0 than increasing Ohnesorge number Oh due to increasing viscosity μ.

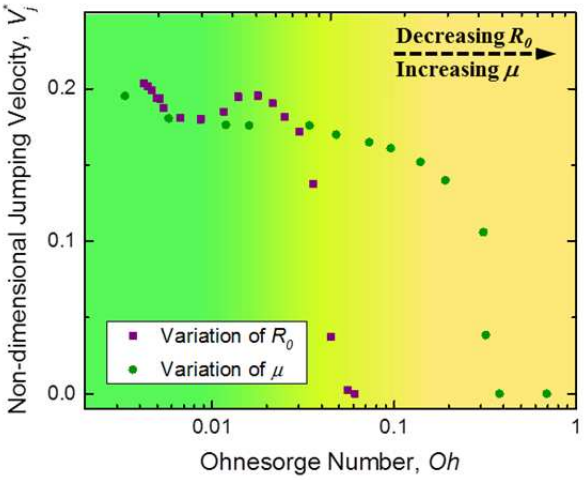

FIGURE 2-12. Discrepancy in the visco-capillary regime. Reduction of the non-dimensional jumping velocity V_j^* by decreasing the droplet radius R_0 or increasing the viscosity μ.

Recent work[112] investigated the coalescence of droplets of water on superhydrophobic surfaces with different wettability and emphasized that the solid-liquid adhesion significantly influences the jumping velocity V_j in the visco-capillary regime. In general, increasing the contact angle hysteresis $\Delta\theta^*$ of a droplet on a super-repellent surface increases the solid-liquid adhesion. During coalescence-induced self-propulsion, higher $\Delta\theta^*$ results in higher dissipation of the released excess surface energy to overcome this solid-liquid adhesion. This in turn reduces the available released excess surface energy that can be converted to the kinetic energy of the jumping droplet. So, higher $\Delta\theta^*$, in general, results in lower jumping velocity V_j than lower $\Delta\theta^*$. However, when $\Delta\theta^*$ is very low, the influence of solid-liquid adhesion is negligible. This is also evident from a recent report[111] that demonstrated virtually no change in the jumping velocity V_j for contact angle hysteresis $\Delta\theta^* < 10°$. In probing the visco-capillary regime (see Figures 3-9 and 3-10), we employed liquids with very high apparent contact angles ($\theta^*_{adv} \approx 162°$ to 165°) and very low contact angle hysteresis ($\Delta\theta^* \approx 2°$ to 4°) on our superomniphobic surfaces (see CH 2-2 Supplementary Information). In other words, we employed surfaces with negligible solid-liquid adhesion. Consequently, in our work, we do not anticipate a significant influence of solid-liquid adhesion on the jumping velocity V_j in the visco-capillary regime. In our work, the decrease in non-dimensional jumping velocity V_j^* with increasing Ohnesorge number Oh in the visco-capillary regime is primarily due to viscous dissipation.

Finally, it must be noted that although liquids with high surface tension may condense in the Cassie-Baxter state on our superomniphobic surfaces, low surface tension liquids will condense in the Wenzel state. This results in relatively high adhesion between the low surface tension liquids and our superomniphobic surfaces. Consequently, coalescence-induced self-propulsion of low surface tension droplets cannot be currently achieved on our superomniphobic

surfaces in practical condensation applications. Further, although the binary mixtures (e.g., water + glycerol) employed in our work allow us to study the fundamental fluid mechanics of coalescence-induced self-propulsion in the inertial-capillary and visco-capillary regimes, during condensation of such binary mixtures, the vapor-liquid equilibria, which determine the composition of the vapor phase and the liquid phase, will have to be carefully considered. So, additional coalescence-induced self-propulsion experiments with practically relevant (chemically homogeneous) liquids are necessary to better understand the implications for practical condensation applications.

2.2.5. Conclusions

We employed superomniphobic surfaces to systematically investigate the coalescence-induced self-propulsion of liquid droplets with a wide range of droplet radii, viscosities and surface tensions in the inertial-capillary regime and the visco-capillary regime. Our results indicate that for all the liquids studied, the non-dimensional jumping velocity V_j^* is nearly constant ($V_j^* \approx 0.2$) in the inertial-capillary regime and decreases in the visco-capillary regime as the Ohnesorge number Oh increases, in agreement with prior work. In the visco-capillary regime, the non-dimensional jumping velocity V_j^* decreases more rapidly with increasing Ohnesorge number Oh due to decreasing droplet radius R_0 than increasing the Ohnesorge number Oh due to increasing viscosity μ. This is because decreasing the droplet radius R_0 increases the inertial-capillary velocity V_{ic} in addition to increasing the Ohnesorge number Oh. Both the increase in Ohnesorge number Oh and the increase in inertial-capillary velocity V_{ic} (i.e., two different factors) contribute to a decrease in the non-dimensional jumping velocity V_j^* with decreasing R_0. Further, in our work, the decrease in jumping velocity V_j and non-dimensional jumping velocity V_j^* with increasing Ohnesorge number Oh in the visco-capillary regime is primarily due to

viscous dissipation; the role of solid-liquid adhesion is negligible because of the very high apparent contact angles θ^* and the very low contact angle hysteresis $\Delta\theta^*$.

2.3. Coalescence-induced Jumping of Droplets on Superomniphobic Surfaces with Macrotexture

Summary: When two liquid droplets coalesce on a super-repellent surface, the excess surface energy is partly converted to upward kinetic energy and the coalesced droplet jumps away from the surface. However, the efficiency of this energy conversion is very low. In this work (**published in Science Advances, 2018**), we employed a simple and passive technique consisting of superomniphobic surfaces with a macrotexture (comparable to the droplet size) to experimentally demonstrate coalescence-induced jumping with an energy conversion efficiency of 18.8% (i.e., ≈ 600% increase compared to superomniphobic surfaces without a macrotexture). The higher energy conversion efficiency arises primarily from the effective redirection of in-plane velocity vectors to out-of-plane by the macrotexture. Utilizing this higher energy conversion efficiency, we demonstrated coalescence-induced jumping of droplets with low surface tension droplets (26.6 mN m^{-1}) and very high viscosity (220 mPa s). These results constitute the first-ever demonstration of coalescence-induced jumping of droplets at Ohnesorge number>1.

2.3.1. Introduction

As described in chapter one and section 2.2, when two liquid droplets coalesce, the released excess surface energy is partly converted into the out-of-plane kinetic energy (due to symmetry breaking), allowing the coalesced droplet to jump away from the super-repellent surface. Prior work on coalescence-induced jumping has demonstrated that the efficiency η of converting the excess surface energy to the out-of-plane kinetic energy (which causes the droplet to jump away from the surface) is very low.[4, 8, 111-113, 118] Such low energy conversion efficiency does not allow coalescence-induced jumping of high viscosity droplets (due to significant viscous dissipation) or low surface tension droplets (due to lack of sufficient excess surface energy).[118-119] In order to enable the coalescence-induced jumping of a wide range of liquids (including those with high viscosity or low surface tension), it is necessary to increase the energy conversion efficiency. However, to the best of our knowledge, there are no reports of simple and passive techniques that can increase the energy conversion efficiency in coalescence-induced jumping on super-repellent surfaces.[157, 180-184] In this work,[185-186] we employed superomniphobic

surfaces possessing a protruding macrotexture (comparable to the droplet size) to experimentally demonstrate coalescence-induced jumping with energy conversion efficiency $\eta \approx 18.8\%$ (i.e., $\approx$ 600% increase in energy conversion efficiency compared to superomniphobic surfaces without a macrotexture). Our numerical simulations indicate that the increase in energy conversion efficiency arises primarily from the effective redirection of in-plane velocity vectors to out-of-plane velocity vectors due to the presence of the protruding macrotexture. Utilizing the significant increase in energy conversion efficiency on our superomniphobic surfaces with a macrotexture, we demonstrate the coalescence-induced jumping of low surface tension droplets (e.g., tetradecane, surface tension $\gamma_{lv} \approx 26.6$ mN m^{-1} and viscosity $\mu \approx 2.1$ mPa s) and very high viscosity droplets (e.g., water + 90% glycerol[187], $\gamma_{lv} \approx 64$ mN m^{-1} and $\mu \approx 220$ mPa s). This is the first-ever demonstration of coalescence-induced jumping at Ohnesorge number $Oh > 1$.[161] Furthermore, based on a non-dimensionalized energy balance that accounts for the additional surface energy stored in the coalesced droplet due to the presence of the protruding macrotexture, we demonstrate that the Weber number at droplet departure (a measure of the conversion of surface energy into upward kinetic energy) increases linearly with the non-dimensional macrotexture height. We envision that the results and insights obtained from our work will impact a wide variety of applications including self-cleaning, anti-icing, energy harvesting, hot spot cooling, condensation and lab-on-chip devices, especially when liquids with significant viscous dissipation and/or systems with significant solid-liquid adhesion are involved.[17, 27, 101, 110, 151, 163, 183, 188-190]

2.3.2. Fabrication and Characterization

Fabrication and characterization of the superomniphobic surfaces were conducted similar to our prior work (see CH 2-2 Supplementary Information). An experimental apparatus

composed of three pieces (i.e., a ridge and two flat solid surfaces) mounted on a stage with a groove (see **Figure 2-13a**) was used to study the coalescence-induced jumping of liquid droplets. The ridge was fabricated by machining an aluminum sheet (thickness ≈ 0.4 mm) with a bench-top grinding machine. The ridge was then placed between two flat aluminum sheets (2 cm x 2 cm) with beveled edges. By adjusting the location of the ridge within the wooden groove, we altered the height of the ridge (100 μm < h_r < 500 μm). After spray coating the ridge and the two flat sheets with 20 wt.% SF100 + 80 wt.% fluorodecyl POSS blends (see CH. 2-2 Supplementary Information), two droplets of equal volume (dispensed with a micropipette) were placed on either side of the ridge. A very thin metal fiber (also spray coated with a superomniphobic coating) was used as a maneuvering probe to gently nudge one of the droplets (with negligible horizontal velocity) and induce coalescence. Note that a thinner coating of 20 wt.% SF100 + 80 wt.% fluorodecyl POSS blends was sufficient to obtain super-repellency for high surface tension liquids (e.g., water, water + 90% glycerol), but a thicker coating, especially at the tip of the ridge (to ensure multiple layers of re-entrant texture), was necessary to obtain super-repellency for low surface tension liquids.

2.3.3. Results and Discussion

In order to investigate the influence of the protruding macrotexture, we experimentally and numerically (see Section 2.2.3, Numerical Model) studied the coalescence of two water droplets (density $\rho \approx 1000$ kg m^{-3}, viscosity $\mu \approx 1$ mPa.s, surface tension $\gamma_{lv} \approx 72$ mN m^{-1}, radius $R_0 \approx 600$ μm) placed on superomniphobic surfaces without and with a protruding macrotexture (a triangular ridge; see Figure 2-13a). Both our experimental results (see **Figures 2-13b** and **2-13d**) and numerical results (see **Figures 2-13c** and **2-13e**) indicate ≈ 600% increase in out-of-plane kinetic energy of the coalesced droplet on superomniphobic surfaces with the ridge compared to

those without the ridge. This manifests as a significant increase in the jumping velocity and jumping height of the droplets on superomniphobic surfaces with the ridge. In each of Figures 2-13b-e, please note that the series of six images (from left to right) represent the following physical events: (i) onset of coalescence, (ii) capillary bridge impinging the surface, (iii) maximum contraction of the coalesced droplet, (iv) departure of the coalesced droplet from the surface, (v) maximum height attained by the coalesced droplet after departing from the surface, and (vi) coalesced droplet impacting the surface upon return.

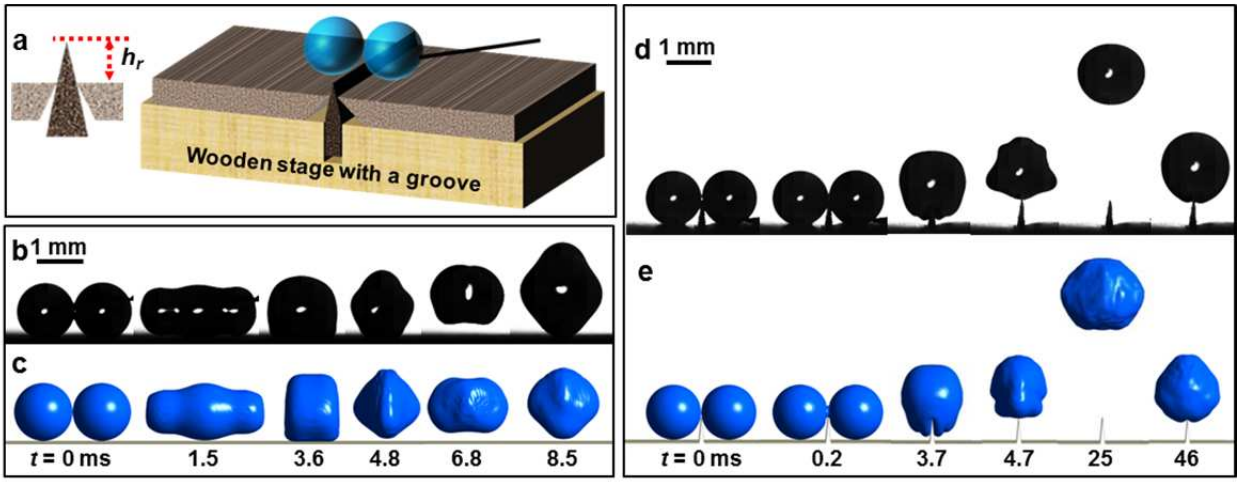

FIGURE 2-13. Coalescence-induced self-propulsion with and without a ridge. a) Schematic of the experimental set-up used to study the coalescence-induced self-propulsion of liquid droplets. The inset shows the height of the ridge h_r. A series of snapshots showing the coalescence-induced self-propulsion of water droplets (R_0 ≈ 600 μm) on superomniphobic surfaces **b)** without a ridge (experimental); **c)** without a ridge (numerical); **d)** with a ridge (experimental); **e)** with a ridge (numerical). In d) and e), the ridge height h_r ≈ 500 μm. Time difference between the experimental snapshots and the corresponding numerical snapshots is < 0.2 ms.

In order to understand the physical principles underlying this increase in out-of-plane kinetic energy, we numerically studied the evolution of the excess surface energy (i.e., driving force of coalescence) and the upward kinetic energy (i.e., kinetic energy by virtue of the net upward velocity) during coalescence of droplets on a superomniphobic surface without and with a ridge. We define the coordinate system as follows – droplets coalesce along the x direction, the

ridge is along the *y* direction and coalesced droplet jumps along the *z* direction (see inset in **Figure 2-14a**). The onset of coalescence of droplets with radius R_0 occurs at time $t = 0$ and eventually the coalesced droplet attains a radius $R_c \approx 2^{1/3} R_0$. At any time t during the coalescence, the driving force for coalescence is the excess surface energy $E_{surf,ex}(t) = E_{surf}(t) - E_{surf,c}$, where $E_{surf}(t) = \gamma_{lv} A_{surf}(t)$ is the surface energy of droplet, $A_{surf}(t)$ is the surface area of the droplet, and $E_{surf,c} = \gamma_{lv} 4\pi R_c^2$ is the surface energy of the coalesced droplet that has eventually attained the radius R_c. At the onset of coalescence (i.e., $t = 0$), the total available excess surface energy $E_{surf,ex}(0) = E_{surf}(0) - E_{surf,c}$. Here, $E_{surf}(0) = \gamma_{lv} 8\pi R_0^2$. During coalescence, this excess surface energy is gradually released. A fraction of the released surface energy is converted to upward kinetic energy $E_{kin,up}(t) = m_c V_{up}^2(t)/2$, where $m_c = \rho 4\pi R_c^3/3$ is the mass of the coalesced droplet and $V_{up}(t)$ is the net upward velocity of the coalesced droplet (see **CH 2-3 Supplementary Information, Components of Velocity**). In our analysis, we non-dimensionalized the relevant parameters as follows: non-dimensional time $t^* = t/t_{ic}$, where $t_{ic} = \sqrt{\rho R_0^3/\gamma_{lv}}$ is the inertial-capillary time scale, non-dimensional excess surface energy $E^*_{surf,ex}(t^*) = E_{surf,ex}(t)/E_{surf,ex}(0)$, and non-dimensional upward kinetic energy $E^*_{kin,up}(t^*) = E_{kin,up}(t)/E_{surf,ex}(0)$. At the onset of coalescence (i.e., at $t^* = 0$), $E^*_{surf,ex}(0) = 1$ and $E^*_{kin,up}(0) = 0$. When the droplet departs from the surface at $t = t_d$ (i.e., at $t^* = t_d^*$), the energy conversion efficiency $\eta = E^*_{kin,up}(t_d^*)$. In order to better explain the physical phenomena, we classify coalescence into three stages – stage I is from the onset of coalescence until the capillary bridge impinges on the surface, stage II is from the capillary bridge impinging on the surface

until the maximum solid-liquid contact area is attained and stage III is from the maximum solid-liquid contact area until the droplet departs from the surface, as described in more detail below.

First, let us consider two droplets of water ($R_0 \approx 600$ μm) coalescing on a superomniphobic surface without a ridge (see Figure 2-14a). Upon coalescence, the capillary bridge begins to expand in *y* and *z* directions, the excess surface energy $E^*_{surf,ex}(t^*)$ reduces with time t^*, and due to the symmetric deformation of the droplet relative to the *xy* plane of coalescence, the net upward velocity of the droplet $V_{up} = 0$ and the upward kinetic energy of the droplet $E^*_{kin,up} = 0$ (see stage I in Figure 2-14a and **CH. 2-3 Supplementary Information, In-plane, Out-of-plane and Total Kinetic Energy**). At $t^* \approx 1$ (i.e., $t \approx t_{ic}$),[4, 111, 118] the capillary bridge impinges on the superomniphobic surface (see **Figure 2-14b**; also see **CH. 2-3 Supplementary Information, Evolution of the Droplet Dynamics in yz view during Droplet Coalescence**), causing symmetry-breaking, which forces the droplet (i.e., the center of mass) to move upward, resulting in a net upward velocity V_{up} [4, 111, 118] and upward kinetic energy of the droplet $E^*_{kin,up}$ (see stage II in Figure 2-14a). Simultaneously, the droplet displays maximum expansion in the *x* direction with two symmetric, high-pressure lobes at +*x* and –*x* extremes (see **Figure 2-14c** and CH. 2-3 Supplementary Information, Evolution of the Droplet Dynamics in yz view during Droplet Coalescence). Subsequently, the internal flow from the high-pressure regions at the lobes to the low-pressure region near the center of the droplet results in droplet contraction in the *x* direction, with maximum contraction and maximum solid-liquid contact area at $t^* \approx 2$ (see **Figure 2-14d** and CH. 2-3 Supplementary Information, Evolution of the Droplet Dynamics in yz view during Droplet Coalescence).[4, 111, 118] The maximum contraction results in a high-pressure region near the center of the droplet and the maximum contact area results in the maximum upward reaction

force on the droplet.[4, 111, 118] This upward reaction force aligns the velocity vectors in the $+z$ direction, resulting in further increase in the upward kinetic energy of the droplet $E^*_{kin,up}$ (see stage III in Figure 2-14a). However, the alignment of velocity vectors is disturbed by the radially outward internal flow from the high-pressure region near the center of the droplet (see **Figure 2-14e** and CH. 2-3 Supplementary Information, Evolution of the Droplet Dynamics in yz view during Droplet Coalescence), impeding the upward motion of the droplet.

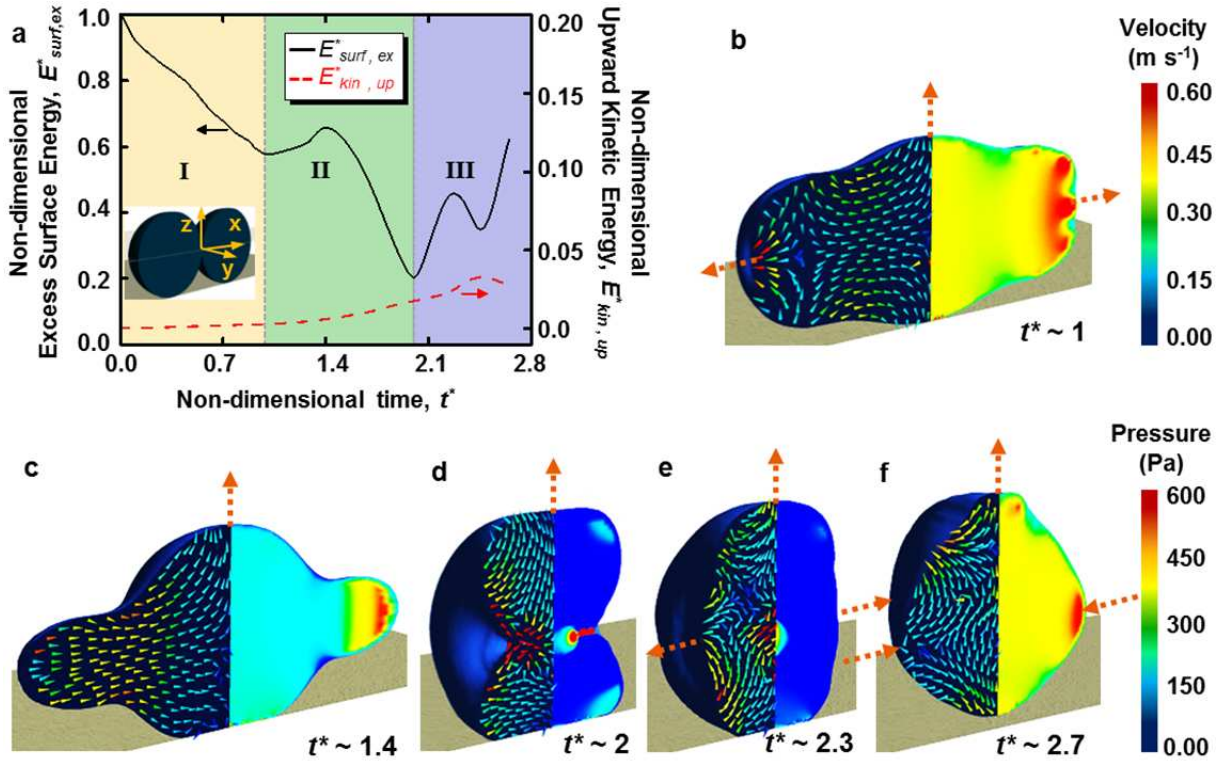

FIGURE 2-14. Droplet dynamics without a ridge. a) Evolution of the non-dimensional excess surface energy ($E^*_{surf,ex}$) and the non-dimensional upward kinetic energy ($E^*_{kin,up}$) during the coalescence of water droplets ($R_0 \approx$ 600 μm) on a superomniphobic surface without a ridge. Inset shows the coordinate system. The three stages (I, II and III) of coalescence are shown with different colors; **b-f)** A series of snapshots showing the pressure distribution and velocity vectors within the droplet on a superomniphobic surface without a ridge. The colors represent the magnitude of pressure and velocity. The dotted orange arrows at droplet periphery indicate the direction of droplet deformation.

Consequently, when the droplet departs from the superomniphobic surface at $t^* = t_d^*$ (see **Figure 2-14f** and CH. 2-3 Supplementary Information, Evolution of the Droplet Dynamics in yz view during Droplet Coalescence), it does so with a relatively low upward kinetic energy and a relatively low energy conversion efficiency $\eta = E_{kin,up}^*(t_d^*) \approx 2.8\%$ (see stage III in Figure 2-14a).[4, 8, 111]

Now, let us consider two similar droplets of water ($R_0 \approx 600$ μm) coalescing on a superomniphobic surface with a ridge (ridge height $h_r \approx 500$ μm; see **Figure 2-15a**). Upon coalescence, similar to that on a superomniphobic surface with no ridge, the capillary bridge begins to expand in *y* and *z* directions, the excess surface energy $E_{surf,ex}^*(t^*)$ reduces with time t^*, and due to the symmetric deformation of the droplet relative to the *xy* plane of coalescence, the net upward velocity of the droplet $V_{up} = 0$ and the upward kinetic energy of the droplet $E_{kin,up}^* = 0$ (see stage I in Figure 2-15a). As might be anticipated, in contrast to the superomniphobic surface with no ridge, the presence of the ridge forces the capillary bridge to impinge on the superomniphobic surface at $t^* < 1$ (i.e., $t < t_{ic}$), causing early symmetry-breaking (see **Figure 2-15b** and CH. 2-3 Supplementary Information, Evolution of the Droplet Dynamics in yz view during Droplet Coalescence). Subsequently, similar to that on a superomniphobic surface with no ridge, the symmetry-breaking forces the droplet (i.e., the center of mass) to move upward, resulting in a net upward velocity V_{up} and upward kinetic energy $E_{kin,up}^*$ (see stage II in Figure 2-15a). Simultaneously, the droplet displays maximum expansion in the *x* direction with two symmetric, high-pressure lobes at $+x$ and $-x$ extremes (see **Figure 2-15c** and CH. 2-3 Supplementary Information, Evolution of the Droplet Dynamics in yz view during Droplet Coalescence). Subsequently, the internal flow from the high-pressure regions at the lobes to the

low-pressure region near the center of the droplet results in the onset of droplet contraction in the *x* direction. However, in striking contrast to the superomniphobic surface with no ridge, during droplet contraction in the *x* direction, the obstruction posed by the ridge redirects the velocity vectors primarily in the +*z* direction (see **Figure 2-15d** and CH. 2-3 Supplementary Information, Evolution of the Droplet Dynamics in yz view during Droplet Coalescence). This redirection of the velocity vectors results in a significant increase in the $E^*_{kin,up}$ (see stage II in Figure 2-15a). Simultaneously, the high-pressure regions move downward (i.e., –*z* direction) and the droplet "wraps" around the ridge with maximum solid-liquid contact area at $t^* \approx 2.1$ (see Figure 2-15d). The maximum contact area results in maximum upward reaction force. A combination of the upward reaction force and the high-pressure regions at the bottom of the droplet (unlike the high-pressure region near the center of the droplet for coalescence on a superomniphobic surface with no ridge) synergistically lead to further alignment of velocity vectors in the +*z* direction (see **Figure 2-15e** and CH. 2-3 Supplementary Information, Evolution of the Droplet Dynamics in yz view during Droplet Coalescence), resulting in further increase in the upward kinetic energy of the droplet $E^*_{kin,up}$ (see stage III in Figure 2-15a). Consequently, when the droplet departs from the superomniphobic surface with the ridge at $t^* = t^*_d$ (see **Figure 2-15f** and CH. 2-3 Supplementary Information, Evolution of the Droplet Dynamics in yz view during Droplet Coalescence), it does so with a high upward kinetic energy and a high energy conversion efficiency $\eta = E^*_{kin,up}(t^*_d) \approx 18.8\%$ (see stage III in Figure 2-15a). Such high energy conversion efficiency η is also possible in coalescence of significantly smaller droplets (R_0 << 600 μm) with ridges comparable to droplet size (see **CH. 2-3 Supplementary Information, Applicability to Smaller Droplets R_0 < 10 μm**).

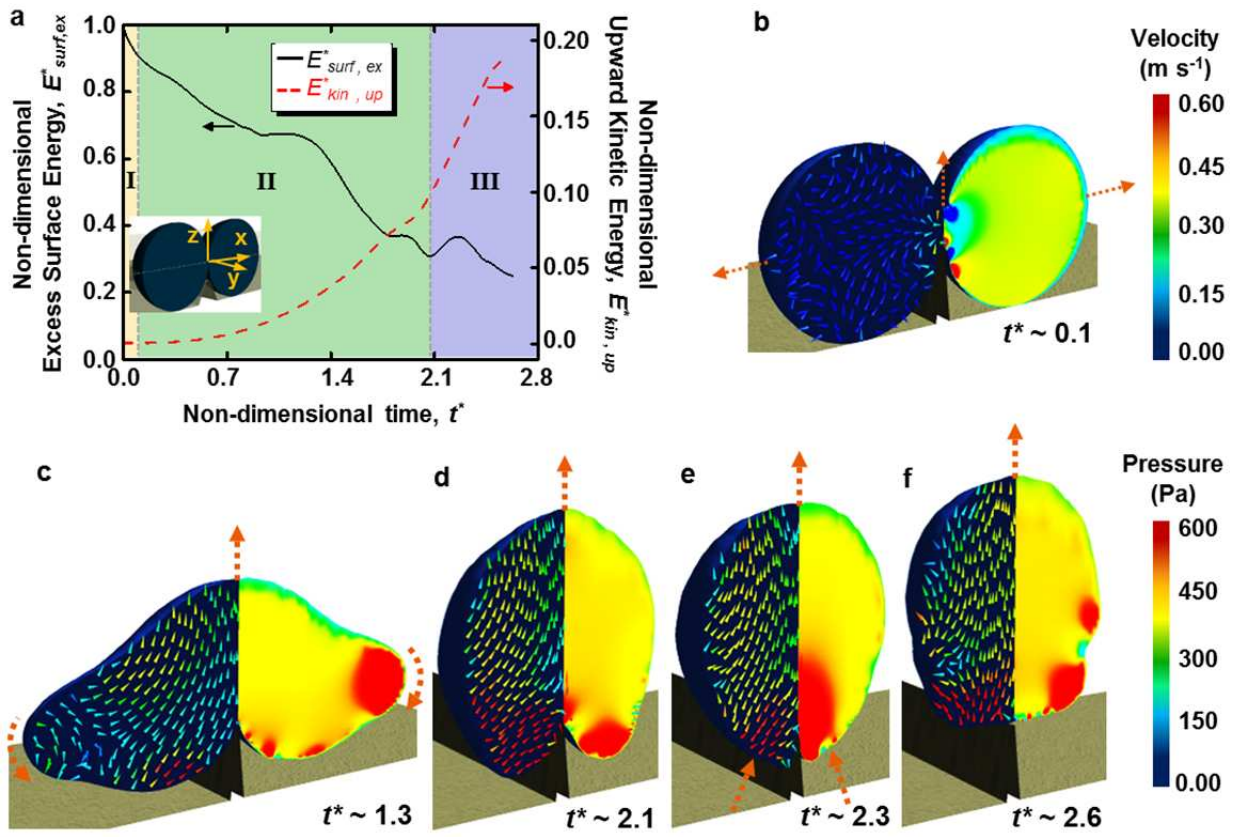

FIGURE 2-15. Droplet dynamics with a ridge. a) Evolution of the non-dimensional excess surface energy ($E^*_{surf,ex}$) and the non-dimensional upward kinetic energy ($E^*_{kin,up}$) during the coalescence of water droplets ($R_0 \approx$ 600 μm) on a superomniphobic surface with a ridge (ridge height $h_r \approx$ 500 μm). Inset shows the coordinate system. The three stages (I, II and III) of coalescence are shown with different colors; **b-f)** A series of snapshots showing the pressure distribution and velocity vectors within the droplet on a superomniphobic surface with a ridge. The colors represent the magnitude of pressure and velocity. The dotted orange arrows at droplet periphery indicate the direction of droplet deformation.

It is evident from the preceding discussion that the energy conversion efficiency during coalescence on a superomniphobic surface with a ridge is ≈ 600% higher than that on a superomniphobic surface without a ridge (see Figure 2-14a and 2-15a). The higher energy conversion efficiency arises primarily from the effective redirection of in-plane velocity vectors to out-of-plane velocity vectors by the ridge. Utilizing this high energy conversion efficiency, we can now achieve coalescence-induced jumping of low surface tension droplets (e.g., *n*-tetradecane with $\rho \approx$ 760 kg m^{-3}, $\mu \approx$ 2.1 mPa s, $\gamma_{lv} \approx$ 26.6 mN m^{-1}, $R_0 \approx$ 480 μm; see **Figure 2-**

16a and **2-16b**) and high viscosity droplets (e.g., water + 90% glycerol[187] with $\rho \approx 1230$ kg m^{-3}, $\mu \approx 220$ mPa s, $\gamma_{lv} \approx 64$ mN m^{-1}, $R_0 \approx 480$ μm; see **Figure 2-16c** and **2-16d**) on superomniphobic surfaces with a ridge. Note that we did not observe coalescence-induced jumping of such low surface tension and high viscosity droplets on superomniphobic surfaces without a ridge (see **CH. 2-3 Supplementary Information, Coalescence of Low Surface Tension and High Viscosity Droplets**). Further, for our coalescence-induced jumping of water + 90% glycerol droplets on superomniphobic surfaces with a ridge, the Ohnesorge number $Oh = \mu/\sqrt{\rho\gamma_{lv}R_0} \approx 1.14$. To the best of our knowledge, this is the first-ever demonstration of coalescence-induced jumping of droplets at $Oh > 1$, i.e., in the viscosity-dominated regime.[4, 111-113, 118]

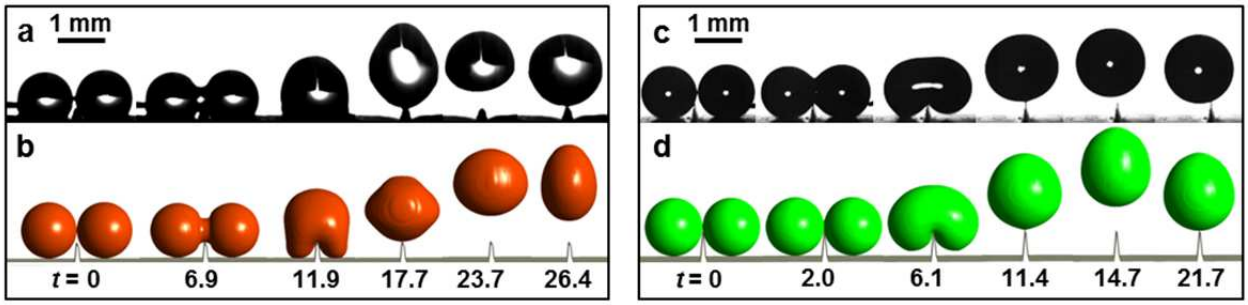

FIGURE 2-16. Coalescence-induced self-propulsion of low surface tension and high viscosity droplets. A series of snapshots showing the coalescence-induced self-propulsion of *n*-tetradecane droplets ($R_0 \approx 480$ μm, $\gamma_{lv} \approx$ 26.6 mN/m) on a superomniphobic surface with a ridge – **a)** experimental, and **b)** numerical; A series of snapshots showing the coalescence-induced self-propulsion of water + 90% glycerol droplets ($R_0 \approx 480$ μm, $\mu \approx 220$ mPa s) on a superomniphobic surface with a ridge – **c)** experimental, and **d)** numerical.

In order to quantitatively investigate the influence of ridge height h_r on the coalescence-induced jumping velocity V_j (note that $V_j = V_{up}(t_d)$), we numerically investigated the coalescence-induced jumping of water droplets with different radii (R_0 = 60 μm, 180 μm and 600 μm) on superomniphobic surfaces with ridges of different heights ($0 < h_r < 600$ μm). Our results (**Figure 2-17a**) indicate that the jumping velocity V_j increases with increasing ridge height h_r and

decreasing droplet radius R_0. In order to physically understand these trends, we rely on scaling arguments based on an energy balance. During droplet coalescence in the inertial-capillary regime on a superomniphobic surface without a ridge, the excess surface energy is partly converted into the upward kinetic energy of the droplet. The corresponding scaling argument based on an energy balance (equation 2-10) can be written as:[4, 8, 111-113, 118, 184]

$$\rho R_0^3 V_j^2 \sim \gamma_{lv} R_0^2 \tag{2-12}$$

Similarly, during droplet coalescence in the inertial-capillary regime on a superomniphobic surface with a ridge, the excess surface energy is partly converted into the upward kinetic energy of the droplet. However, in striking contrast to the superomniphobic surface without a ridge, during coalescence on a superomniphobic surface with a ridge, the droplet "wraps" around the ridge (see Figure 2-15d). In this configuration, additional surface energy is stored in the deformed droplet. This additional surface energy scales as $\gamma_{lv} R_0 h_r$. When the droplet departs from the surface (i.e., $t = t_d$), in addition to the excess surface energy, this additional surface energy stored in the deformed droplet is also partly converted to upward kinetic energy. The corresponding scaling argument based on an energy balance can be written as:

$$\rho R_0^3 V_j^2 \approx C_1 \gamma_{lv} R_0^2 + C_2 \gamma_{lv} R_0 h_r \tag{2-13}$$

Here, the constants C_1 and C_2 account for the partial energy conversion and the geometric factors. Non-dimensionalizing the ridge height as $h^* = h_r / R_0$ and the jumping velocity as $V_j^* = V_j / V_{ic}$, where $V_{ic} = \sqrt{\gamma_{lv} / \rho R_0}$ is the inertial-capillary velocity, equation (2-13) can be rewritten as:

$$We_j \sim C_1 + C_2 h^* \tag{2-14}$$

Here, $We_j = V_j^{*2} = \rho R_0 V_j^2 / \gamma_{lv}$ is the Weber number when the droplet departs (or jumps away) from the surface. We_j is a measure of the conversion of surface energy into upward kinetic energy. Hence, the energy conversion efficiency η can be rewritten in terms of the Weber number We_j at $t = t_d$ as:

$$\eta = \frac{E_{kin,up}(t_d)}{E_{surf,ex}(0)} = \frac{\rho \frac{4}{3}\pi R_c^3 V_j^2 / 2}{\gamma_{lv} 8\pi R_0^2 - \gamma_{lv} 4\pi R_c^2} \approx 0.8 \frac{\rho R_0 V_j^2}{\gamma_{lv}} \approx 0.8 We_j \qquad (2\text{-}15)$$

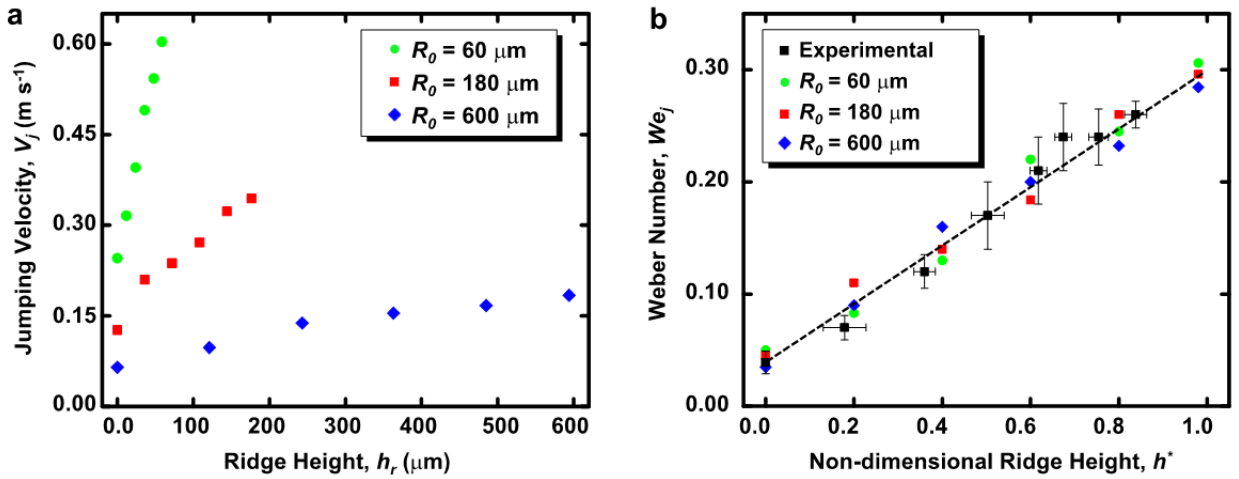

FIGURE 2-17. Jumping velocity of coalescing droplets with and without a ridge. a) Jumping velocity of droplets with different radii on superomniphobic surfaces with different ridge heights (data from numerical simulations); **b)** Both numerical and experimental data collapse onto a single non-dimensional straight line of Weber number at droplet departure (or jumping) vs. non-dimensional ridge height, in accordance with equation (3). Error bars in the experimental data represent the error associated with velocity, droplet radius and ridge height measurements.

It is evident from equation (2-14) that We_j increases linearly with increasing non-dimensional ridge height h^*. Physically, this implies that a higher ridge height h_r or a smaller droplet radius R_0 leads to a more efficient conversion of the surface energy to upward kinetic energy. Indeed, both our numerical and experimental results (with different droplet radius R_0 and ridge height h_r) collapse onto a single non-dimensional straight line in accordance with equation (2-14), confirming the validity of our scaling arguments (see **Figure 2-17b**). Further, at $h^* = 0$

(i.e., on a superomniphobic surface without a ridge), $We_j = V_j^{*2} \approx 0.041$ (i.e., non-dimensional jumping velocity, $V_j^* \approx 0.2$), which is in good agreement with prior reports of coalescence-induced jumping on super-repellent surfaces without a ridge.[4, 8, 111-113, 118, 184]

Along with the ridge height h_r, the ridge angle α can potentially affect the coalescence-induced jumping of droplets through inducing a geometric limitation for coalescence to occur. For a ridge height h_r and droplet radius R_0 (i.e., non-dimensional ridge height, $h^* = h_r / R_0$), there is a maximum ridge angle α_{max} beyond which coalescence cannot occur because the ridge physically obstructs the droplets from contacting each other.

In order to determine α_{max}, consider a 2D view of the *xz* plane (**Figure 2-18**; *y*-axis is into and out of the plane of the figure) with two identical droplets of radius R_0 contacting each other, just prior to coalescing symmetrically relative to the *yz* plane. Now, consider a triangular ridge (*ABC* in Figure 2-18) of height $OA = h_r$, located symmetrically relative to the *yz* plane, between the two coalescing droplets, with the maximum possible ridge angle $BAC = \alpha_{max}$. When the ridge angle $\alpha > \alpha_{max}$, the ridge physically obstructs the droplets from contacting each other, thereby preventing coalescence. When $\alpha = \alpha_{max}$, each ridge arm (*AB* and *AC*) contacts each droplet tangentially (at *D* and *E*). Say, the origin is at *O*, then the ridge peak *A* is (0, h_r). Let the tangential contact point *E* be (x_E, y_E). The slope *m* of the tangent *AEC* to the circle (representing the right droplet), is given as:

$$m = -\frac{x_E - R_0}{z_E - R_0} \tag{2-16}$$

The slope *m* of the line *AE* in terms of the ridge height h_r, is given as:

$$m = -\frac{h_r - z_E}{x_E} \tag{2-17}$$

Combining equations 2-16 and 2-17 and recognizing that $E(x_E, y_E)$ must satisfy the equation of the circle (representing the right droplet), $(x-R_0)^2+(z-R_0)^2=R_0^2$, we obtain,

$$x_E = \frac{2R_0(R_0-h_r)^2}{R_0^2+(R_0-h_r)^2} \quad \& \quad z_E = \frac{R_0 h_r^2}{R_0^2+(R_0-h_r)^2} \tag{2-18}$$

Now, recognizing that $\tan\left(\frac{\alpha_{max}}{2}\right) = \frac{x_E}{h_r - z_E}$, and using equation 2-18, we obtain:

$$\alpha_{max} = 2\tan^{-1}\left\{\frac{2(1-h^*)}{1-(1-h^*)^2}\right\} \tag{2-19}$$

It is evident from equation 2-19 that as $h^* \to 0$ (i.e., when the ridge height is negligible compared to the droplet radius), $\alpha_{max} \to \pi$; and as $h^* \to 1$ (i.e., when the ridge height approaches the droplet radius), $\alpha_{max} \to 0$. As may be anticipated, physically, it implies that as the ridge height increases, the ridge should be sharper (i.e., the maximum ridge angle is smaller) to prevent physical obstruction and allow coalescence, i.e., as h^* increases, α_{max} decreases (see **CH. 2-3 Supplementary Information, Influence of the Ridge Angle**).

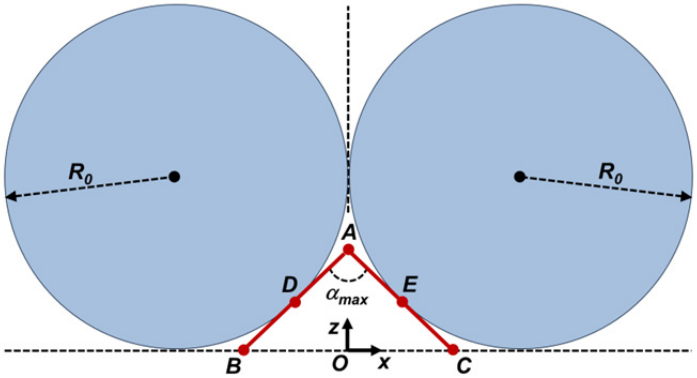

FIGURE 2-18. 2D schematic of two coalescing droplets and a ridge with maximum ridge angle α_{max}.

2.3.4. Conclusion

In summary, we employed a simple and passive technique consisting of superomniphobic surfaces with a ridge to experimentally demonstrate coalescence-induced jumping with a high energy conversion efficiency $\eta \approx 18.8\%$ (i.e., about 600% increase in energy conversion efficiency compared to superomniphobic surfaces without a ridge). Utilizing the significant increase in energy conversion efficiency on our superomniphobic surfaces with a ridge, we demonstrate the coalescence-induced jumping of low surface tension droplets (e.g., tetradecane, surface tension $\gamma_{lv} \approx 26.6$ mN m^{-1}) and very high viscosity droplets (e.g., water + 90% glycerol, $\mu \approx 220$ mPa s). These results constitute the first-ever demonstration of coalescence-induced jumping of droplets at $Oh > 1$, i.e., in the viscosity-dominated regime. We envision that the results and insights obtained from our work will impact a wide variety of applications including self-cleaning, anti-icing, energy harvesting, hot spot cooling, condensation and lab-on-chip devices, especially when liquids with significant viscous dissipation and/or systems with significant solid-liquid adhesion are involved.[17, 27, 101, 110, 151, 163, 183, 188-190] In specific, we anticipate super-repellent surfaces that possess hierarchically structured, periodic ridges throughout the surface can enhance the energy conversion efficiency in practical applications with droplet coalescence at multiple length scales (see **CH. 2-3 Supplementary Information, Hierarchical Structure for Coalescence-induced Jumping of Droplets at Different Length Scales**).[191-192]

Further, our numerical simulations indicate that the underlying mechanism for the increase in energy conversion efficiency is the effective redirection of in-plane velocity vectors to out-of-plane velocity vectors due to the presence of the ridge. Based on a non-dimensionalized energy balance that accounts for the additional surface energy stored in the coalesced droplet due to the presence of the ridge, we demonstrated that the Weber number at droplet departure (a measure of

the conversion of surface energy into upward kinetic energy) increases linearly with the non-dimensional ridge height. In this context, it is interesting to note that protruding macrotextures on super-repellent surfaces can favorably alter the droplet dynamics in coalescence (by increasing the jumping velocity and energy conversion efficiency) as well as in bouncing or splitting (by reducing the contact time),[1, 193] to enhance the departure of the droplet from the surface. In droplet coalescence on macrotextures, surface energy is converted to kinetic energy and in droplet bouncing or splitting on macrotextures, kinetic energy is converted to surface energy; in both cases, some energy is lost to viscous dissipation. The scaling arguments presented in our work, especially those related to surface energy stored in a deformed droplet, may be useful to understand droplet dynamics in bouncing and splitting on ridges. While our work has primarily focused on incorporating the influence of the ridge height into the scaling arguments, a more detailed study is necessary to incorporate the influence of the ridge angle into the scaling arguments.

3. CHAPTER 3- SMOOTH SLIPPERY SURFACES

3.1. Slippery Hydrophilic (SLIC) Solid Surfaces

Summary: Hydrophilic surfaces, fabricated through tethering of hydrophilic nano-brushes to solid surfaces, have huge potential in phase-change heat transfer (e.g., dropwise condensation) due to significantly higher nucleation rate. However, despite such great potential, conventional hydrophilic surfaces have not been widely used in thermal-fluidic applications due to the poor liquid mobility or lack of slipperiness. In this work (**under review in Science Advances**), we, for the first time, developed a simple "grafting to" technique to fabricate a novel hydrophilic yet slippery surface that has not been experimentally realized thus far. Combination of very high droplet nucleation and growth rate (aroused by the hydrophilic nature of the surface) with prompt droplet removal (due to the slippery nature of the surface) makes it a viable alternative for state-of-art surfaces used in dropwise condensation. Finally, relying on the selective slipperiness of our surface against low and high surface tension liquids, we developed the first-ever simple slipperiness-based technique for water-oil separation. Due to such novel properties, we envision that our SLIC surface will attract significant attention in the thermal-fluidic research community and also from industrial sectors.

3.1.1. Introduction

Tailoring the interactions between solid surfaces and contacting liquids has many biomedical and industrial implications such as fabrication of antifouling[194] and thrombo-resistant[195] surfaces as well as surfaces to be used in devices with high-flux modes of heat transfer[196]. Prior work has shown that compared to hydrophobic surfaces, hydrophilic surfaces (i.e., $\theta \ll 90°$) are preferred for phase-change heat transfer applications (e.g., dropwise condensation) due to lower energy barriers for heterogeneous nucleation (facilitated by higher solid surface energy)[197] that can result in orders of magnitude higher nucleation rate[79-80]. Combination of such high nucleation rate with lower conduction thermal resistance[198] (induced by low contact angle) can potentially increase the heat transfer coefficient, significantly. Further, high liquid mobility is required to enable droplet removal during condensation that is crucial for sustained dropwise condensation. Consequently, a hydrophilic surface that is also slippery can potentially attract tremendous interest in thermal-fluidic applications. However, lack of slipperiness on conventional hydrophilic surfaces (see **Figure 3-1a** demonstrating a water

droplet that cannot slide on a hydrophilic surface even when it is tilted by 90°) hinders the utilization of such surfaces in many thermo-fluidic applications.

Despite this experimental inability to obtain slipperiness on hydrophilic surfaces, a prior work[199] numerically investigated the possibility of slippage of water molecules on such surfaces. They assumed a solid surface that is *i*) perfectly physically homogeneous (i.e., no roughness on the surface), *ii*) perfectly chemically homogeneous (i.e., uniform distribution of hydrophilic agents on the surface) and *iii*) is tethered by hydrophilic nano-brushes (i.e., molecules) to obtain low contact angle ($\theta \approx 40°$). Using molecular dynamic MD simulation, they explored the critical role of inter-tether distance *D* (i.e., the distance between two adjacent hydrophilic nano-brushes) on slippage of water molecules between two adjacent nano-brushes on the surface. Their results indicate that if the inter-tether distance *D* is sufficiently low, water molecules can smoothly slide from one hydrophilic site to the next one, indicative of low energy barrier against the motion (i.e., the surface is highly slippery); whereas on a surface with high inter-tether distance *D*, water molecules need to hop from one hydrophilic agent to the next one, indicative of high energy barrier against motion, which results in no slippery behavior.

3.1.2. Fabrication and Characterization

Motivated by the MD simulations,[199] we fabricated the first-ever non-textured (i.e., smooth) **S**lippery Hydrophi**lic** (SLIC) Solid Surface that demonstrates unprecedented slipperiness despite its hydrophilicity. Macroscopic water droplets (i.e., Volume of test droplets ≈ 20 μl) deposited on our precisely engineered SLIC surfaces displayed advancing and receding contact angles of $\theta_{\mathrm{adv}} = 38 \pm 1°$ and $\theta_{\mathrm{rec}} = 35 \pm 1°$, respectively (see **Figure 3-1b**, $\Delta\theta \approx 3°$). Such negligible contact angle hysteresis results in very low sliding angle (i.e., $\omega = 3°$, see Figure 3-1b). The fabrication process contains acid-catalyzed grafting of hydrophilic nano-brushes

(length of brushes in the straightest conformation < 2 nm) to nearly perfectly smooth silicon wafers with sufficiently high grafting density (i.e., number of nano-brushes per unit area), resulting in low inter-tether distance *D*. We hydroxylated the surface (see **Figure 3-1c**) that was followed by PEGylation (i.e., immobilization of the Polyethylene glycol nano-brushes to the surface, see **CH. 3-1 Supplementary Information**). PEGylation of the surfaces conducted with a low molecular weight (i.e., possessing very short chain length) PEG silane (i.e., 2-[Methoxy(Polyethyleneoxy) 6-9propyl]Trimethoxysilane) using a "grafting to" technique. The fabrication procedure of our SLIC surface is fairly simple and straightforward (i.e., no need for complex synthetic-chemistry techniques and equipment) and can be termed "instant" as it takes only a few minutes to fabricate a hydrophilic slippery surface at room temperature. Despite its simplicity, the "grafting to" approach has not been considered a viable method in fabrication of surfaces with high grafting density, because polymer chains can hardly approach a solid surface that is already sterically hindered around pre-existing bound chains.[200] Nevertheless, utilizing a PEG silane with very short chain length in this work shrank the area surrounding each nano-brush which is sterically unfavorable for other PEG silanes to be tethered. This indeed enabled us to obtain high grafting densities (i.e., $\sigma > 1$) that are substantially above the maximum grafting densities accessible using "grafting to" techniques.[201] To the best of our knowledge, this is the first-ever report of very high grafting density using a "grafting to" approach. We envision that our slippery hydrophilic solid surface will have numerous biomedical and thermal applications including, but not limited to, self-cleaning, surfaces for sustained dropwise condensation, fluid handling and transportation, and antifouling bio-implants.

Hydrophilic surfaces are known to display high affinity to contacting liquids that results in spreading of the droplets on the surface and thus low contact angles ($\theta < 90°$; see Figure 3-1a). If

an external stimulation is applied to a droplet on a solid surface (e.g., the gravitational force on a tilted surface, see Figure 3-1a), the droplet distorts from its axi-symmetry and adopts the minimum contact angle at the receding edge (θ_{rec}) and the maximum contact angle at the advancing edge (θ_{adv}) of the triple phase (i.e., solid-liquid-vapor) contact line TPCL. When the applied external force (here $mg\sin\omega$, where m , g, and ω are the mass of the droplet, the gravitational acceleration and the sliding angle, respectively) is greater than the adhesion force at the solid-liquid interface ($\gamma_{lv}D_{TCL}\left(\cos\theta_{rec}-\cos\theta_{adv}\right)$, where γ_{lv} and D_{TCL} are the liquid surface tension and the width of TPCL perpendicular to the direction of droplet motion, respectively), the droplet begins to slide on the surface.[3, 16, 54] Contact angle hysteresis $\Delta\theta=\theta_{adv}-\theta_{rec}$ is a measure of the energy dissipated when a droplet moves on a solid surface. Low $\Delta\theta$ leads to low sliding angle ω, which is a measure of the slipperiness of the surface. Hence, the low sliding angle of a droplet on a solid surface ($\omega\rightarrow 0$) represents the highly slippery nature of the surface, whereas the sliding angle of a droplet increases ($\omega\rightarrow 90$) by decreasing the slipperiness of the surface. Easy motion of a liquid droplet on a hydrophilic surface is impeded by pinning of the droplet at the receding edge of the TPCPL that leads to $\theta_{rec}\rightarrow 0°$. This indeed causes the droplet to either stick to the surface (i.e., the droplet cannot slide on the surface even if it is tilted by 90°, see Figure 3-1a), or sheds (without de-pining) and forms a continuous film on the surface.

Prior MD work[199] indicated the critical role of the inter-tether distance D on the slipperiness of hydrophilic surfaces that are perfectly physically and chemically homogeneous. In order to investigate the mechanism underlying such superior slipperiness on our SLIC surfaces, in this work, we estimated the inter-tether distance $D\sim 2/\sqrt{\pi\sigma}$ through calculation of the grafting density σ as:[202]

$$\sigma = \frac{h\rho N_A \times 10^{-21}}{M_n} \tag{3-1}$$

Here h is the thickness of the monolayer of PEG nano-brushes on the solid surface, ρ is the density of the bulk PEG at 293 K, N_A is the Avogardo's number, and M_n is the average molecular weight of the PEG. Our results (see **Figure 3-1d**) indicate that we can vary the grafting density from very low ($\sigma \rightarrow 0$ Chain nm^{-2}) to very high ($\sigma \rightarrow 1.4$ Chain nm^{-2}) by increasing the PEGylation time t_{PEG}. This in turn varies the inter-tether distance from very high ($D \rightarrow 16$ nm) to very low ($D \rightarrow 0.9$ nm). At PEGylation time $t_{PEG} = 0$ min, the grafting density $\sigma = 0$ Chain nm^{-2} and surface is fully covered by hydroxyl groups (–OH) which display higher affinity to contacting liquids. This results in substantial spreading of the test droplet on the surface (i.e., $\theta \rightarrow 0°$) and the droplet sheds on the surface without de-pinning at the receding edge of the TPCL (i.e., $\theta_{rec} \rightarrow 0°$) and thus forms a film when the surface is tilted. However, at very high PEGylation time (e.g., $t_{PEG} = 300$ min), the grafting density is very high (i.e., $\sigma \rightarrow 1.4$ Chain nm^{-2}) and the surface is virtually fully covered by PEG nano-brushes. This results in a hemispherical shape in the test droplet on the surface with contact angle $\theta \approx 36°$, the receding contact angle is close to the advancing and Young's contact angles (i.e., $\theta \approx \theta_{adv} \approx \theta_{rec}$ and thus $\Delta\theta \rightarrow 0°$) and the droplet easily slides on the surface (i.e., $\omega \approx 3°$, see Figure 3-1b). If the PEGylation time is very low ($t_{PEG} \rightarrow 0$ s), the grafting density σ is very low and the PEG nano-brushes are sparsely distributed on the surface that results in very high inter-tether distance ($D \rightarrow 16$ nm). Hence, the test droplet is in contact with a composite layer of PEG nano-brushes and hydroxyl groups that, compared to $t_{PEG} = 0$ s, results in an increase in the Young's contact angle ($0° < \theta \rightarrow 36°$; see **Figure 3-1e**). In addition, increase of the receding contact angle ($\theta_{rec} > 0°$) facilitates the de-pining of the droplet form the surface and the droplet can slide on the surface (see **Figure 3-1f**).

Further increase of the grafting density σ through increasing the PEGylation time t_{PEG} results in reduction of the inter-tether distance D, which in turn increases the contact angle θ and reduces the sliding angle ω (indicative of higher slipperiness). Our results (Figure 3-1e and 3-1f) indicate a plateau in the contact angle and the sliding angle of a droplet at higher grafting density (i.e., inter-tether distance D < 3.3 nm). The PEG silane we used in this work contains 6-9 ethylene glycol EG groups (see CH. 3-1 Supplementary Information). Prior MD simulations indicate that each of these EG groups can make a hydrogen bond with a water molecule to form the hydration layer.[203] Length of a hydrogen bond is ≈ 0.2 nm and the Flory radius of each PEG silane is ≈ 1.3 nm.[204-205] This indicates that virtually an area with diameter d_h ≈ 1.5 nm around each PEG nano-brush can be considered as the sterically hindered area. Figure 3-1f inset indicates that at inter-tether distance D < 3 nm, both the sliding angles and their error bars are very low. We postulate that this threshold inter-tether distance (i.e., D_t ≈ 3 nm) corresponds to the sterically hindered area between two adjacent PEG nano-brushes (i.e., $D_t \approx 2d_h$) in a fully packed condition. Inter-tether distance threshold D_t indicates a distance bellow which test droplets can hardly penetrate between two adjacent nano-brushes and pins to the solid surface. Consequently, if the PEGylation time t_{PEG} > 15 min (see Figure 3-1d), the grafting density is sufficiently high (σ > 0.17 Chain nm^{-2}), which results in the inter-tether distance < 3 nm. Such low inter-tether distance (i.e., $D < D_t$) is less than the diameter of a sterically hindered area surrounding each PEG nano-brush that prevents the approach of the molecules of a test droplet to the solid surface (i.e., no scope of the pining of a test droplet on such surface). Lack of pining of the test droplets on these surfaces results in superior slipperiness (i.e., ω < 3°).

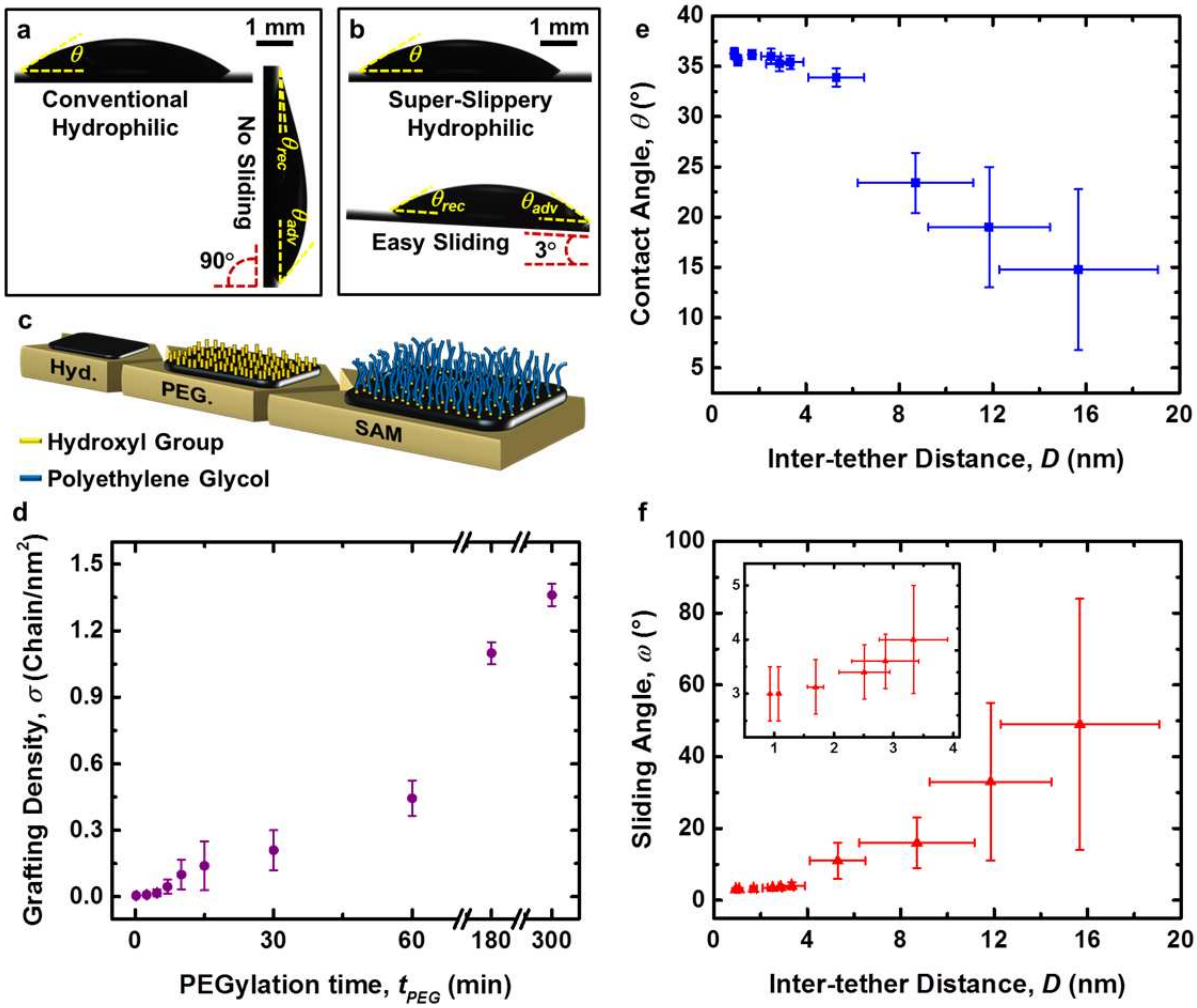

FIGURE 3-1. Fabrication of the non-textured slippery hydrophilic (SLIC) solid surfaces. a) A water droplet on a conventional hydrophilic surface (the droplet cannot slide on the surface even when it is tilted by 90°); **b)** A water droplet on a SLIC surface (the droplet can easily slide across the surface tilted by 3° relative to the horizontal); **c)** Schematic of the fabrication process of SLIC surfaces; **d)** Variation of the grafting density σ by PEGylation time t_{PEG}; **e)** Variation of the contact angle θ by inter-tether distance D; **f)** Variation of the sliding angle ω by inter-tether distance D. Inset shows the sliding angle ω on surfaces with inter-tether distance $D > D_t$. There is likelihood for droplets to not slide on surfaces with $D \approx 12$ and 16 nm even if the surface are tilted by 90°. In such cases, the sliding angle ω are considered 90° to estimate the error bars. Volume of the test droplets ≈ 20 μl.

According to the MD work,[199] chemical homogeneity is a prominent parameter influencing the liquid mobility on hydrophilic slippery surfaces. In order to investigate the influence of chemical homogeneity on slipperiness of our SLIC surfaces, we compared the high-resolution

C1s XPS spectra at multiple (> 30) locations on different SLIC surfaces (see **Figure 3-2a**; also see CH. 3-1 Supplementary Information).

High-resolution C1s XPS spectra (see Figure 3-2a) showed the presence of a peak at 286.5 eV corresponding to the –C–O bond on PEGylated surfaces. Further, increasing the PEGylation time t_{PEG} results in increasing the intensity of the –C–O peak, indicative of an increase in the grafting density σ of PEG nano-brushes on surfaces. Comparison of the intensity of –C–O peak at different spots (> 30 locations) on surfaces with high PEGylation time (e.g., t_{PEG} > 10 min) indicates negligible deviation, implying excellent chemical homogeneity on such surfaces. In contrast, Figure 3-2a illustrates two representative curves with substantial deviation in the intensity of the –C–O peak associated with different spots on a surface with very short PEGylation time (e.g., $t_{PEG} \approx 5$ s), implying poor chemical homogeneity on such surfaces. This substantial chemical inhomogeneity on surfaces with low PEGylation time is reflected in very large error bars in the contact angle θ (see Figure 3-1e) and the sliding angle ω (see Figure 3-1f) of water droplet on these surfaces.

The MD simulation[199] also assumed that the hydrophilic surface is perfectly smooth and the influence of surface roughness on slipperiness was not studied. Such assumption is reflected in fabrication of our SLIC surfaces on silicon wafers with root mean square roughness $R_{rms} \approx$ 0.25 nm, implying high degree of physical homogeneity. We investigated the influence of surface roughness on wettability and slipperiness of hydrophilic surfaces (see CH. 3-1 Supplementary Information). Our atomic force microscopy (AFM) results (see **Figure 3-2b**) indicate that the contact angle θ does not vary noticeably by altering the surface roughness. In contrast, the sliding angle ω increases by increasing the surface roughness, indicative of high sensitivity of the surface slipperiness to surface roughness and surfaces with R_{rms} > 200 nm are

no longer slippery. Figure 3-2b inset demonstrates the topography of a silicon wafer before and after PEGylation for $t_{PEG} \approx 300$ min, indicating the negligible influence of the PEGylation on morphology of solid surfaces. Ellipsometry revealed that our SLIC coatings were < 1 nm thick. Based on these results, we fabricated our SLIC surfaces with PEGylation of silicon wafers for $t_{PEG} = 20$ min for the results discussed below.

Our SLIC surfaces also display slipperiness against lower surface tension liquids. Utilizing droplets of water containing different concentrations of sodium dodecyl sulfate (SDS)[206] with different surface tensions, we systematically investigated the variation of the wettability and slipperiness of our SLIC surfaces by surface tension γ_{lv}. In agreement with Young's law (equation 1-1), our results (see **Figure 3-2c**) indicate that the contact angle θ of test droplets reduce by reduction of the surface tension γ_{lv} and thus the surface is "omniphilic". Further, in agreement with Furmidge's law (equation 1-4), the sliding angle ω of test droplets reduce by reduction of the surface tension γ_{lv} and thus the surface is "omnislippery". To the best of our knowledge, this is the first-ever report of "omniphilic" and "omnislippery" surface (against liquids with surface tension $\gamma_{lv} > 38$ mN m^{-1}). Further, such surface tension-based selective slippery on non-textured and non-lubricated slippery surfaces has not been experimentally realized.[207] Indeed, it is in striking contrast to SLIPS over which the sliding angle is not influenced by surface tension (due to cloaking) and also to superomniphobic surfaces over which the sliding angle increases by reducing the surface tension.[207]

Our SLIC surface display superior slipperiness at room condition (i.e., temperature $T_{room} \approx 25°$ and relative humidity $HR \approx 30\%$). We also explored the influences of temperature and humidity on wettability and slipperiness of SLIC surfaces. Our results (see **Figure 3-2d**) indicate that the surface can retain its wettability and slipperiness in a broad range of relative humidity (i.e., 10%

< *HR* < 100%). Similarly, variation of the contact angle and sliding angle of water droplets on SLIC surfaces by temperature (0° < $T_{surface}$ < 70°) is negligible.

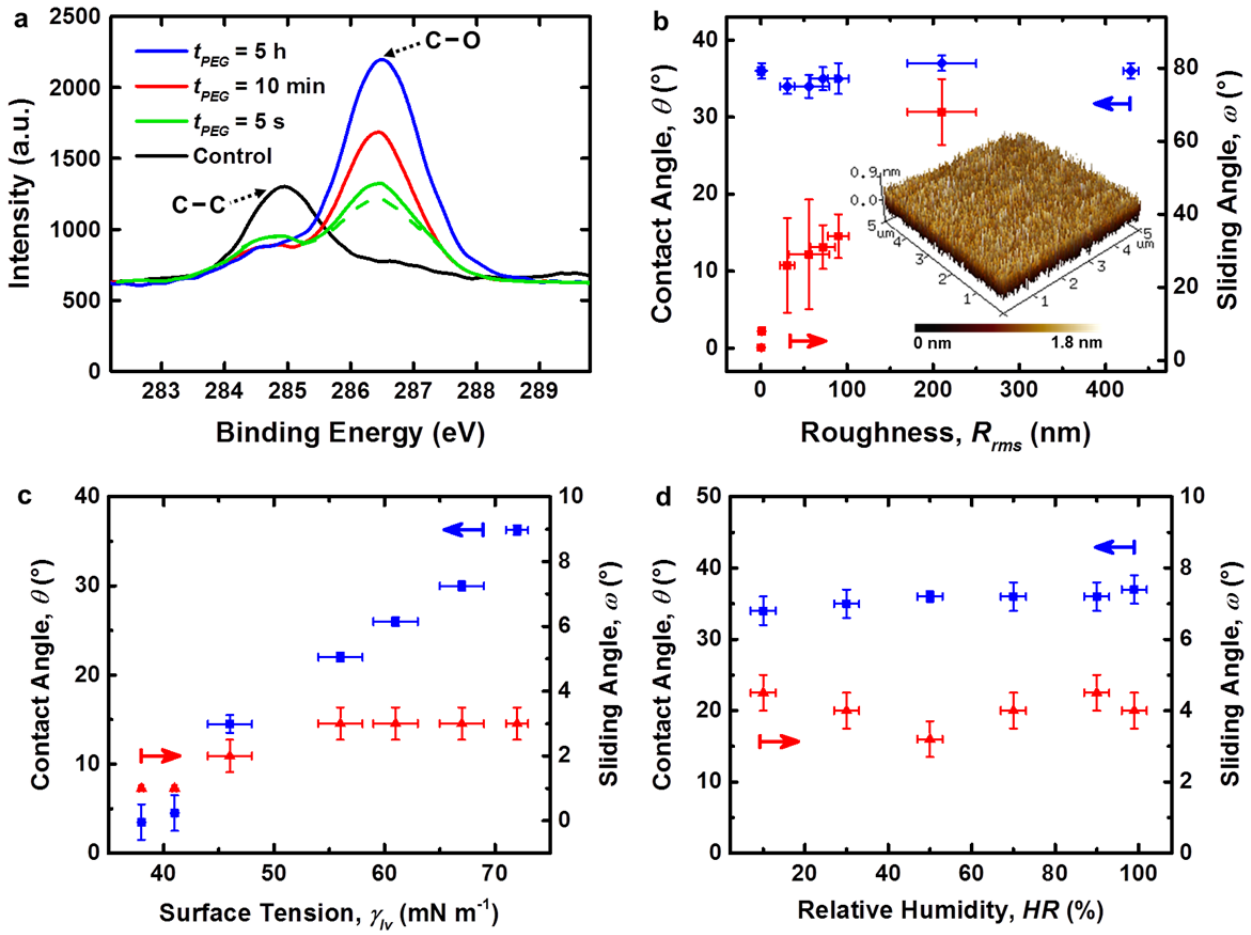

FIGURE 3-2. Characteristics of slippery hydrophilic (SLIC) solid surfaces. a) High-resolution C1s XPS spectra of the unmodified and PEGylated surfaces. The –C–C peak on an unmodified silicon wafer is due to adventitious carbon. The –C–O peak on the PEGylated surface is indicative of PEGylation. Two different representative curves associated to the surfaces with very low PEGylation time indicate the lack of chemical homogeneity on such surfaces; **b)** Variation of contact angle θ and sliding angle ω by surface roughness R_{rms}. Inset shows an AFM image depicting the topography of the PEGylated surface (t_{PEG} = 300 min) with root mean square roughness, R_{rms} < 1 nm and thickness < 1 nm; **c)** Variation of contact angle θ and sliding angle ω by surface tension of test liquids γ_{lv}, indicative of the omniphilic and omnislippery nature of our SLIC surfaces; **d)** Variation of contact angle θ and sliding angle ω by relative humidity *HR*, indicative of the stability of our SLIC surfaces in a wide range of humidity.

3.1.3. Results and Discussion

Our SLIC surface is unique due to its ***i***) omniphilic and selective omnislippery nature, ***ii***) extremely smooth topography, ***iii***) robust slipperiness, and ***iv***) inert nature (no toxicity and charge)[208]. Further, our fabrication technique is fairly simple allowing a systematic variation of the grafting density in a wide range. These unique features make our SLIC surface an exceptional candidate for a broad range of thermal-fluidic applications. For example, **Figure 3-3a** demonstrates that a droplet sliding on our SLIC surface can remove dirt along its path and thus our SLIC surface can also be used for self-cleaning applications. Further, as mentioned, our SLIC surface is the first-ever smooth surface that display selective slipperiness based upon the surface tension of test droplets (i.e., droplets with γ_{lv} < 38 mN m^{-1} cannot slide on the surface). This property enables the separation of immiscible liquids on SLIC surfaces. To demonstrate it, we placed a binary droplet composed of water (representing a high surface tension liquid) and n-hexadecane dyed in red (γ_{lv} ≈ 27.5 mN m^{-1}, representing a low surface tension liquid) on a SLIC surface (see **Figure 3-3b**). According to the Young's law (equation 1-1), n-hexadecane forms a film ($\theta \rightarrow 0$) on the surface and water droplet stay on top of that. Note that the surface is not slippery against n-hexadecane, while water droplet can easily slide on it. Upon tilting the surface, the binary droplet begins to move due to the gravitational force. Since n-hexadecane cannot slide on the surface, it only sheds (a residue of n-hexadecane is obvious along the path of the droplet), while the water droplet can easily slide on the surface and separate from the low surface tension impurities. To the best of our knowledge, this is the first-ever report of the separation of high surface tension liquids and low surface tension liquids based on selective slipperiness, compared to prior wettability-based methods.[209]

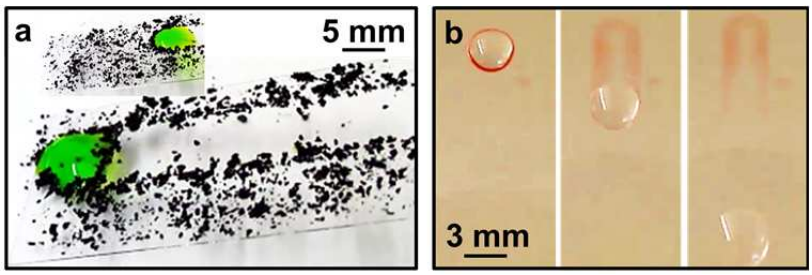

FIGURE 3-3. Applications of SLIC surfaces. a) Self-cleaning on a SLIC surface; **b)** Separation of high surface tension and low surface tension liquids due to the selective slipperiness on our SLIC surface. A droplet composed of water and n-hexadecane (dyed in red) is sliding on a surface tilted by ≈ 30°

3.1.4. Dropwise Condensation on Slippery Hydrophilic Solid Surfaces

Droplet nucleation and condensation are ubiquitous phenomena in nature and industry. Over the past century, research has shown that heat transfer rates during steam dropwise condensation on non-wetting (e.g., hydrophobic) surfaces can be 10X higher than widely accepted filmwise condensation on wetting substrates.[210-211] However, the need for non-wetting hydrophobic coatings in achieving dropwise condensation of water is unclear.

Heat transfer coefficient in dropwise condensation on a solid surface is governed by nucleation and growth of droplets on the surface. According to the classical nucleation theory,[79-80] the rate of nucleation and thus the droplet growth rate increases significantly by increasing the hydrophilicity of the surface (i.e., reducing the contact angle) due to reduced energy barriers for heterogeneous nucleation facilitated by higher solid surface energy.[197, 212] Combination of such high nucleation rate with lower conduction thermal resistance[198] (induced by low contact angle) increases the heat transfer coefficient, significantly. This suggests hydrophilic surfaces as ideal candidates for enhanced dropwise condensation. However, despite this compelling potential, due to the lack of droplet removal mechanism on conventional hydrophilic surfaces (see **Figure 3-4a**), utilization of such surfaces in dropwise condensation did not receive noticeable interest in industrial sectors.

Continuous droplet removal from the surface plays a key role in achieving sustained dropwise condensation. The mobility of a droplet on solid surfaces is governed mainly by the adhesion at solid-liquid interface, which can be decreased through reducing the contact angle hysteresis,[49, 100, 213-216]. Maintaining a high intrinsic wettability (i.e., $\theta_{adv} \ll 90°$) with minimal contact angle hysteresis is difficult to achieve.[65] Many studies have noted the formation of discrete 'flat' water droplets on hydrophilic surfaces during condensation (due to atmospheric contamination of volatile organic compounds after cleaning[217-218]), while the corresponding receding contact angle is typically close to zero,[219] which results in filmwise condensation[220]. Hence, for the past eight decades, researchers have focused on the application of hydrophobic and super-repellent surfaces (displaying low contact angle hysteresis) to achieve dropwise condensation. Droplet removal (mainly through coalescence-induced jumping) on such surfaces is achieved at the expense of high droplet nucleation and growth rate as well as the low conduction thermal resistance. Indeed, condensation on super-repellent surfaces can enhance the heat transfer coefficient only by 30%.[221] Further, recent attempts on the application of super-repellent surfaces (to remove condensate at micrometer length scales through coalescence-induced jumping) has been threatened by nucleation-mediated flooding (i.e., nucleation of droplets in the Wenzel state),[222] progressive flooding (i.e., coalescence of droplets without jumping due to high solid-liquid adhesion),[157] and droplet return due to gravity.[223-224] In another direction, lubricant infused surfaces (LISs or SLIPSs) have been used to achieve dropwise condensation due to the negligible contact angle hysteresis on such surfaces. However, such surfaces are not considered a viable alternative for super-repellent surfaces due to their inherent drawbacks such as water-lubricant miscibility, cloaking of water droplets, and lubricant drainage by time.[225]

While all prior work on achieving dropwise condensation has focused on employing hydrophobic surfaces, we postulate that achieving stable dropwise condensation on a solid hydrophilic surface with low contact angle hysteresis is theoretically possible. Compared to hydrophobic surfaces (see **Figure 3-4b**), dropwise condensation on hydrophilic surfaces (see Figure 3-4a) has additional advantages including enhanced nucleation (due to reduced energy barriers for heterogeneous nucleation)[197] and growth rate, and lower conduction thermal resistance[198] that can lead to higher heat transfer coefficient. The only parameter threatening the superior performance of a slippery hydrophilic surface, compared to its hydrophobic counterparts, is the droplet departure radius (r_{max}). The departure radius r_{max} of a droplet (with volume V_{max}) sliding on a solid surface is the radius of an equivalent droplet (with volume V_{max}) with spherical shape. Small droplet departure radius r_{max} on a surface can result in prompt removal of small droplets from the surface before they can coalesce with many surrounding droplets; whereas, too large droplet departure radius r_{max} increases the possibility of droplet coalescence and film formation on the surface. According to the Furmidg's law, the droplet departure radius r_{max} on a surface is governed by both contact angle (representative of the surface wettability) and contact angle hysteresis (representative of the liquid mobility on the surface). Hence, the droplet departure radius r_{max} on a surface mounted vertically can be estimated as:

$$r_{\max} \approx [\frac{3\gamma_{lv}}{2\pi\rho g}\sin(\frac{\theta_{rec}+\theta_{adv}}{2})(\cos\theta_{rec}-\cos\theta_{adv})]^{1/2} \quad (3\text{-}2)$$

Here γ_{lv}, ρ and g are the liquid surface tension, the liquid density, and the gravitational acceleration, respectively and also θ_{rec} and θ_{adv} are the receding and advancing contact angles, respectively. Equation 3-2 indicates that on moderately hydrophilic to hydrophobic surfaces (i.e., $40° < \theta < 120°$, shaded in pink in **Figure 3-4c**), the droplet departure radius r_{max} is mainly governed by the contact angle hysteresis (i.e., for a given contact angle hysteresis, variation of

the r_{max} with contact angle is insignificant, see Figure 3-4c). This indicates the critical role of contact angle hysteresis on droplet removal (and thus the sustained dropwise condensation) on slippery surfaces. Further, droplet sliding and mobility due to gravitational force becomes virtually invariant to intrinsic surface wettability as the contact angle hysteresis approaches zero (see Figure 3-4c).

In order to experimentally reconcile our predictions about achieving dropwise condensation on solid hydrophilic surfaces, we qualitatively studied the nucleation, growth and removal of droplets on a *i*) hydrophilic and non-slippery surface (θ = 54°±1° and $\omega \rightarrow$ 90°, Figure 3-4-a), *ii*) hydrophobic and slippery surface (θ = 105°±1° and ω = 5°±1°, Figure 3-4-b), and *iii*) hydrophilic and slippery surface (θ = 37°±1° and ω = 5°±1°, **Figure 3-4d**).

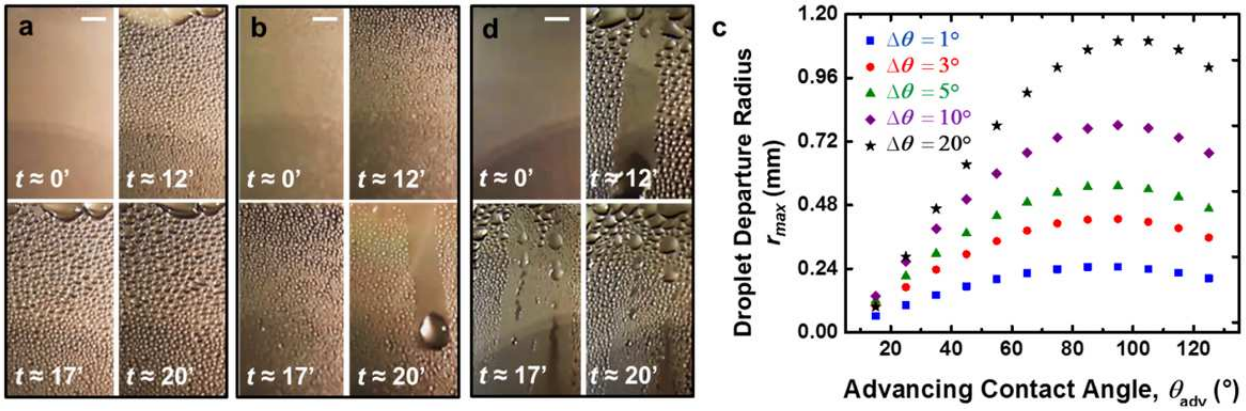

FIGURE 3-4. Dropwise condensation. a and **b)** on a non-slippery hydrophilic (control) and hydrophobic slippery, surfaces, respectively. Only one droplet slides on the hydrophobic slippery surface indicating low nucleation rate and droplet growth; **c)** Influence of contact angle and contact angle hysteresis on the droplet departure radius; Dropwise condensation on our SLIC surfaces. High nucleation rate and growth on our SLIC surface is followed by prompt droplet removal (through sliding and swiping) which makes free room for new nucleation and can result in significantly higher heat transfer coefficient. Scale bars represent 1 mm.

During our experiments, the surface temperature was kept constant (i.e., $T_w = 20 \pm 2°C$) using a Peltier plate with temperature controller. Further, water vapor generated in a boiling dish was transferred to the chamber to provide the vapor supply at temperature $T_v = 65 \pm 5°C$). Comparison of the hydrophilic and hydrophobic surfaces (see Figure 3-4a and 3-4b) clearly

demonstrates faster nucleation and growth of droplets on hydrophilic surfaces. High nucleation rate and growth on the non-slippery hydrophilic surface (see Figure 3-4a) follows only by coalescence of droplets (without sliding) that will lead to transition to filmwise regime. Nucleation rate and droplet growth are much slower on hydrophobic surfaces. Hence, it takes longer time for a droplet to grow to the droplet departure size and begins to slide on the surface (see Figure 3-4b). In contrast, high nucleation rate and growth on our SLIC surface (induced by hydrophilic nature of the surface) is followed by prompt droplet removal (through sliding of large droplets that also swipes smaller droplets along its path) which makes free room for new nucleation (see Figure 3-4d). To the best of our knowledge, this is the first-ever report of dropwise condensation on a hydrophilic (non-lubricated) surface. Combination of the high nucleation and growth rate and the prompt droplet removal from the SLIC surface may result in significantly higher heat transfer coefficient and also critical heat flux and thus makes the SLIC surface a viable alternative for state-of-art hydrophobic and super-repellent surfaces.

3.1.5. Conclusion

Hydrophilic surfaces, fabricated through tethering of hydrophilic nano-brushes to solid surfaces, have huge potential in phase-change heat transfer (e.g., dropwise condensation) due to significantly higher nucleation rate and lower conduction thermal resistance. However, despite such great potentials, conventional hydrophilic surfaces have not been widely used in thermal-fluidic applications due to the poor liquid mobility aroused by the lack of slipperiness at the interface of such surfaces with contacting liquids. In this work, we, for the first time, developed a simple “grafting to” technique to fabricate a novel hydrophilic yet slippery surface that has not been experimentally realized thus far. Combination of very high droplet nucleation and growth rate (aroused by the hydrophilic nature of the surface) with prompt droplet removal (due to the

slippery nature of the surface) makes it a viable alternative for state-of-art surfaces used in dropwise condensation. Finally, relying on the selective slipperiness of the surface against low and high surface tension liquids, we developed the first-ever simple slipperiness-based technique for water-oil separation. Due to such novel properties, we envision that our SLIC surface will attract significant attention from the thermal-fluidic research community and also from industrial sectors.

3.2. On-demand Droplet Manipulation via Triboelectrification

Summary: Droplet manipulation has attracted tremendous interest across different scientific fields over the past two decades. However, current droplet manipulation techniques suffer from drawbacks such as complex fabrication of manipulation platform, or low droplet motility (i.e., long response time), or expensive actuation system, or lack of precise control on droplet motion. In this work, for the first time, we demonstrate controlled manipulation of liquid droplets of both high dielectric strength (e.g., water) and low dielectric strength (e.g., n-hexadecane) on a smooth and slippery surface via triboelectric effect. Our facile and portable methodology enables on-demand, precise manipulation of droplets using solely an electrostatic attract or repulsion force, which is exerted on the droplet by a simple charged actuator (e.g., Teflon sheet). We further demonstrate that even a finger can act as an actuator to enable the transport of droplet. We envision that our simple triboelectric-based droplet manipulation technique will open a new avenue for lab-on-a-chip systems, energy harvesting devices and biomedical applications.

3.2.1. Introduction

Droplet manipulation typically refers to the actuation of an individual liquid droplet using external stimuli.[226] In response to the change in the surrounding physical and/or chemical conditions induced by the external stimuli, an initially stagnant droplet (e.g., a droplet resting on a solid surface) deforms and adopts a dynamic-state (e.g., sliding or rolling off).[226] Upon actuation, a droplet in the dynamic-state can be transported, splitted, merged, or arranged in a controlled manner. These indeed enable the complex functionalities of droplets, such as chemical synthesis,[226] DNA analysis,[226] cell culture,[227] drug screening,[226] electronic displays[228-229] and energy harvesting[230]. Therefore, droplet manipulation has attracted tremendous interest across different scientific fields over the past two decades. To date, a variety of external stimuli-mediated methods based on magnetic field,[231] electric field,[232] light,[233] wettability gradient,[234] or

morphing of surface topography[123] have been developed for manipulating droplets on surfaces. However, these methods usually have drawbacks such as complex fabrication of manipulation platform, low droplet motility (i.e., long response time), expensive actuation system (e.g., laser) and lack of precise control on droplet motion. In this work, for the first time, we demonstrate the controlled manipulation of liquid droplets of both high dielectric strength (e.g., water) and low dielectric strength (e.g., n-hexadecane) on a smooth, slippery and hydrophobic surface via triboelectric effect. Our facile and portable methodology enables on-demand, precise manipulation of droplets using solely an electrostatic attract or repulsion force, which is exerted on the droplet by a simple charged actuator (e.g., Teflon sheet). We further demonstrate that even a finger can act as an actuator to enable the transport of droplet. We envision that our simple triboelectric-based droplet manipulation technique will open new avenues for lab-on-a-chip systems, energy harvesting devices and biomedical applications.

Triboelectrification (or contact electrification) is a contact-induced surface charging phenomenon, in which two surfaces acquire charges of opposite signs (i.e., positive and negative) after they make contact and then detach from each other.[235-236] Although it was discovered over two thousands year ago in ancient Greece, the complex mechanisms involved in the triboelectrification process are still not fully understood so far.[236-237] Nevertheless, an empirical triboelectric series (i.e., a list of materials ranked based on their tendency to become positively or negatively charged) has been established over years to enable qualitative evaluation of the triboelectric properties of different materials.[238] Interestingly, no liquid is included in such series, although the contact electrification of liquids with both high and low dielectric constants, after they contact solid surfaces, has been observed in the past century.[238-239] Despite the lack of fundamental understanding, the contact electrification at a liquid-solid interface has attracted

increasing interest in the past few years, particularly to develop nano energy harvesting technologies.[236] For example, it has been recently shown that pipetting a droplet of a dielectric liquid results in accumulation of positive charges in the droplet (due to the contact of the droplet with the pipette).[240] Leveraging this positive charge, in this work,[241] we demonstrated that a droplet can be attracted using an actuator with an inherently negative charge (e.g., Teflon sheet) or it can be repelled using an actuator with an inherently positive charge (e.g., Nylon sheet) on a slippery surface (see **Figure 3-5a**).

3.2.2. Fabrication and Characterization

We fabricated a hydrophobic slippery surface (see **Figure 3-5b**) through dip coating of nearly perfectly-smooth glass cover slips in chlorine-terminated polydimethylsiloxane (PDMS, see **CH. 3-2 Supplementary Information**). Combination of the extremely low roughness of the glass cover slips and the chemical homogeneity of the hydrophobic coating resulted in a homogeneously slippery surface that facilitates smooth slide of droplets on the surface. During sliding of a liquid droplet on our slippery surface, triboelectrification between the droplet and the surface simultaneously happens that leaves negative charges on the surface and also results in further accumulation of positive charges on the droplet (see **Figure 3-5c**).[242] It has been demonstrated that the amount of charge acquired by the droplet upon sliding on the surface increases by increasing the travel distance d (i.e., a length the droplet slides on the slippery surface).[237] In order to systematically investigate the influence of travel distance d on the amount of charge acquired by the liquid droplet, we placed a droplet of water ($V \approx 50$ μl) on our slippery surface tilted by an angle greater than the sliding angle of the droplet on the surface ω. The water droplets flew down the slippery surface from different travel distances d (ranging from 0.5 mm to 80 mm) spontaneously due to the effect of gravity and fell out of the surface directly between

electrodes of an experimental setup (see **Figure 3-5d**).[239-240, 243] The experimental setup was composed of two electrodes immersed in a bath of silicone oil and the amount of charge on the droplet was precisely measured during the electrophoretic motion of the droplet between electrodes (Details of the experimental setup to measure droplet charge can be found elsewhere[240]). When a charged droplet was dispensed into the liquid bath between two positive and negative electrodes (connected to a power supply), it was deflected horizontally due to the effect of Coulomb force ($F_c = q_d E$).[244] Here, q_d is the net charge of the droplet and E is the uniform, horizontal electric field between two electrodes. Within a short time after deflection, the water droplet reached to a horizontal equilibrium in which the Coulomb force was balanced by the drag force[245] exerted on it from the surrounding silicon oil (i.e., horizontal acceleration ≈ 0). Hence, we can estimate the droplet charge q when the droplet is in the equilibrium condition as:

$$q = \frac{4\pi\mu UR}{E}\frac{3\lambda + 2}{2(\lambda + 1)} \tag{3-3}$$

Here, μ is the viscosity of the silicone oil, U and R are velocity and equivalent radius of the droplet, and λ is the ratio of the viscosity of water and silicon oil. Similar to prior work,[246] our results (see **Figure 3-5e**) indicate that the droplet charge density q'' (i.e., ratio of the net charge of the droplet q to its overall surface area $A = 4\pi R^2$) increased by increasing the travel distance d to reach a plateau due to the charge saturation of the liquid droplet. Further increase in the travel distance d of the liquid droplet cannot alter the droplet charge density q''. **Figure 3-5f** also demonstrates the possibility of tuning the droplet charge q by changing the travel distance d. In this figure, the right droplet (with white sign) travelled $d \approx 0.5$ mm, while the left droplet (with green sign) travelled $d \approx 80$ mm and thus acquired higher charges. Such greater charge enabled it

to overpass the right droplet due to the higher applied Coulomb force, after they were both diverted within the electric field.

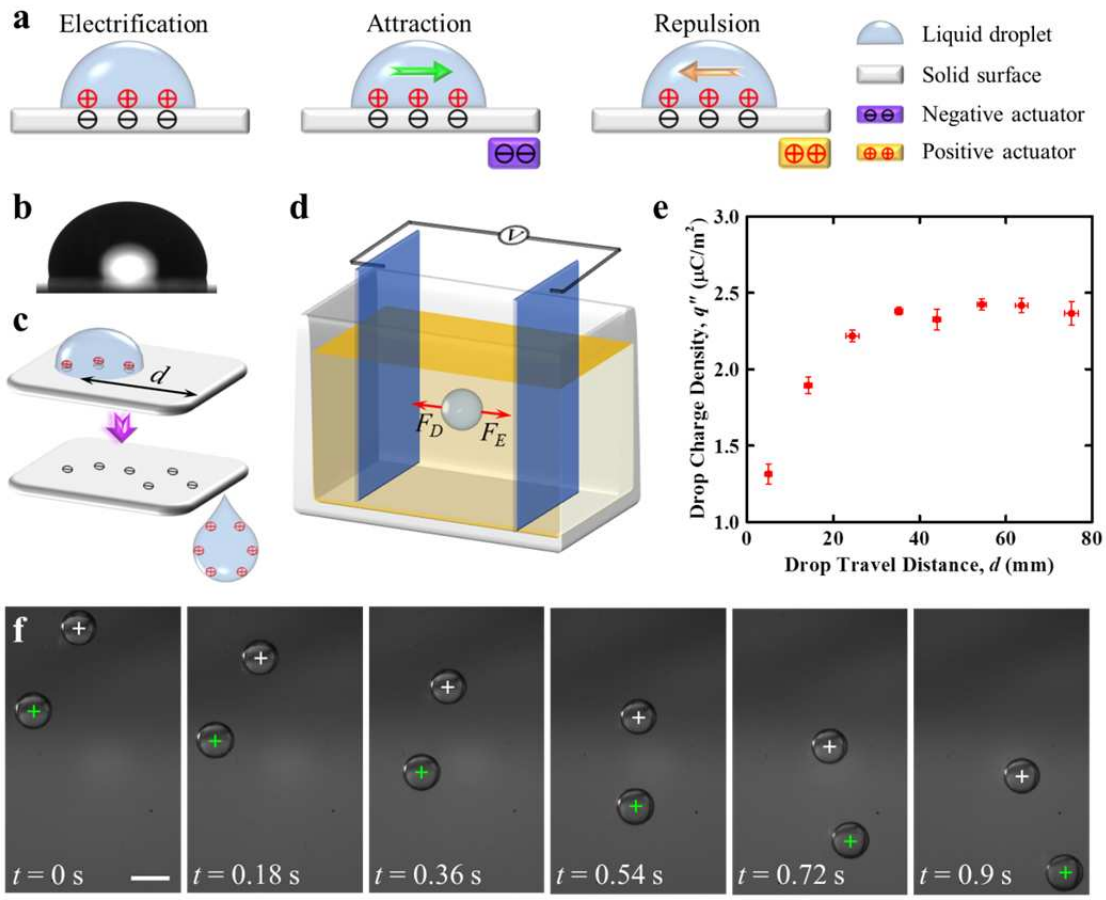

FIGURE 3-5. Charge acquired by a droplet sliding on a solid surface. a) Upon contact of a droplet with a solid surface, it acquires positive charges, while the surface is negatively charged. The positively charged droplet can be attracted or repelled using negatively or positively charged actuators, respectively **b)** A water droplet on the hydrophobic slippery surface used in this work; **c)** Schematic of a droplet acquiring charges upon sliding on the surface; **d)** A Faraday cup composed of 2 electrodes in a bath of oil (to induce a uniform horizontal electric field) for measuring the charge of a droplet during its free fall between electrodes; **e)** Variation of the droplet charge density by its sliding distance on the solid surface; **f)** Free fall of a highly charged (green) and slightly charged (white) water droplets between electrodes of a Faraday cup. A greater Coulomb force applied to the highly charged droplet enables the droplet to overpass the slightly charged droplet. Scale bar represents 5 mm.

3.2.3. Results and Discussion

When a charged droplet on a slippery surface is stimulated by an actuator (with a net charge of q_a) placed at distance L from the droplet, an electrostatic force is exerted to the droplet

(i.e., $F_{el} \sim q_d q_a / L^2$).[244] The electrostatic force attracts the liquid droplet if the actuator has opposite charge (e.g., here Teflon sheet) or repels it if the actuator has similar charge (e.g., here Nylon sheet). Further, the adhesion force between a liquid droplet and a solid surface can be estimated as[100]

$$F_{adh} = \gamma_{lv} D_{TCL} (\cos\theta_{rec} - \cos\theta_{adv}) \tag{3-4}$$

Here, γ_{lv} is the surface tension of the liquid droplet, θ_{rec} and θ_{adv} are the receding contact angle and the advancing contact angle and D_{TCL} is the width of the triple phase contact line perpendicular to the sliding direction. If the magnitude of the electrostatic force is greater than the adhesion force at solid-liquid interface, the liquid droplet can slide toward (i.e., attraction) or away from (i.e., repulsion) the actuator. To demonstrate the feasibility of controlled manipulation of a liquid droplet on a slippery surface, we placed a water droplet on our slippery surface and moved a negative actuator (i.e., Teflon film) close to the droplet (see **Figure 3-6a**). The water droplet began to slowly move toward the actuator when the distance between the droplet and the actuator was $L \approx 6.5$ mm (i.e., Figure 3-6a, $t = 0$ s). The electrostatic force increased by decreasing the distance between the water droplet and the actuator L resulted in acceleration of the droplet ($t \leq 0.12$ s). Further reduction in the distance between the water droplet and the actuator L resulted in significant increase in the magnitude of electrostatic force ($t \rightarrow 0.15$ s). Consequently, the water droplet was highly elongated and rapidly moved toward the actuator. Similarly, we placed a water droplet on our slippery surfaces and moved a positive actuator (i.e., Nylon sheet) close to the droplet (see **Figure 3-6b**). Immediately, the water droplet began to quickly move away from the actuator when the distance between the droplet and the actuator was $L \approx 2$ mm (i.e., Figure 3-6b, $t = 0$ s). The electrostatic force decreased by increasing the distance between the droplet and the actuator L resulted in deceleration of the droplet ($t \leq 0.14$ s). Further

increase in the distance between the water droplet and the actuator L resulted in significant reduction in the magnitude of electrostatic force ($t \rightarrow 0.21$ s). Consequently, the water droplet continued to very slowly move away from the actuator.

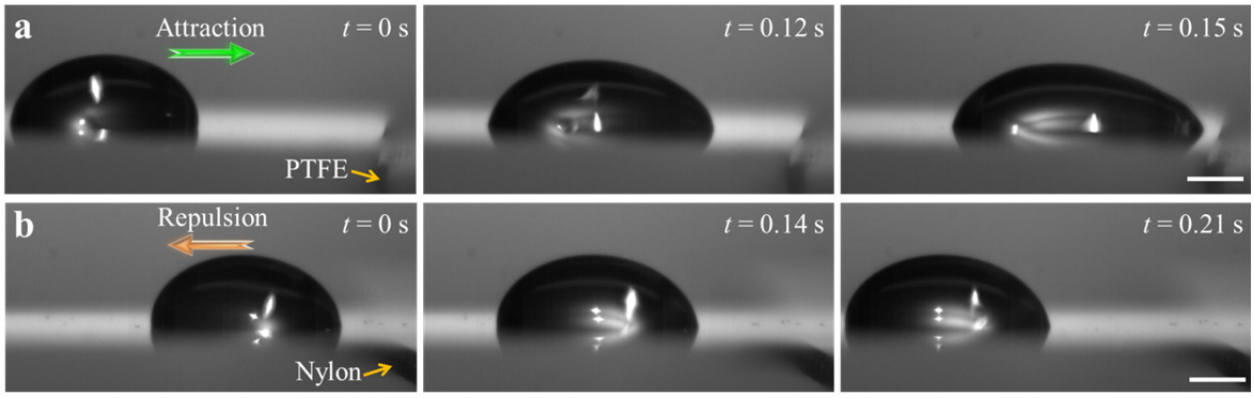

FIGURE 3-6. Droplet manipulation on a hydrophobic slippery surface. a and **b)** Attraction and repulsion of positively charged water droplets using a negatively charged (here PTFE) and positively charged (here Nylon) actuators, respectively. Scale bar represents 2 mm.

Our facile and portable triboelectric-based methodology can be applied to precisely manipulate liquid droplets in complex conditions. For example, the uphill motion of a liquid droplet on a tilted surface is complex because it is not only affected by the adhesion force, but also influenced by the gravitational force.[234] However, our results (see **Figure 3-7a**) demonstrate that a water droplet can be driven up a slippery surface tilted by 12° (i.e., sliding angle of the same droplet on our surfaces was $\omega \approx 15°$). In this experiment, an initially stagnant water droplet (Figure 3-7a, $t = 0$ s) was driven up the slippery surface using an actuator with negative charges (i.e., Teflon film). The droplet continued its uphill motion while the actuator stopped moving. This indeed decelerated the droplet and the droplet eventually stopped at distance $L \approx 60$ mm away from the actuator (Figure 3-7a, $t = 4.5$ s), where the electrostatic force on the water droplet was balanced by the sum of the adhesion force and the gravitational force. The uphill motion of the droplet further indicates that the electrostatic force can be significantly higher than the adhesion force at the solid-liquid interface. Prior work[247-249] has reported the triboelectric effect

even in liquids with low dielectric strength (e.g., n-hexadecane). This indicates the feasibility of the manipulation of droplets of low dielectric strength using our triboelectric-based methodology. **Figure 3-7b** and **Figure 3-7c** demonstrate the attraction and repulsion of a droplet of n-hexadecane with very low dielectric constant ($\varepsilon \approx 2.05$ MV m^{-1})[250] toward or away from the actuators (Teflon or Nylon), respectively.

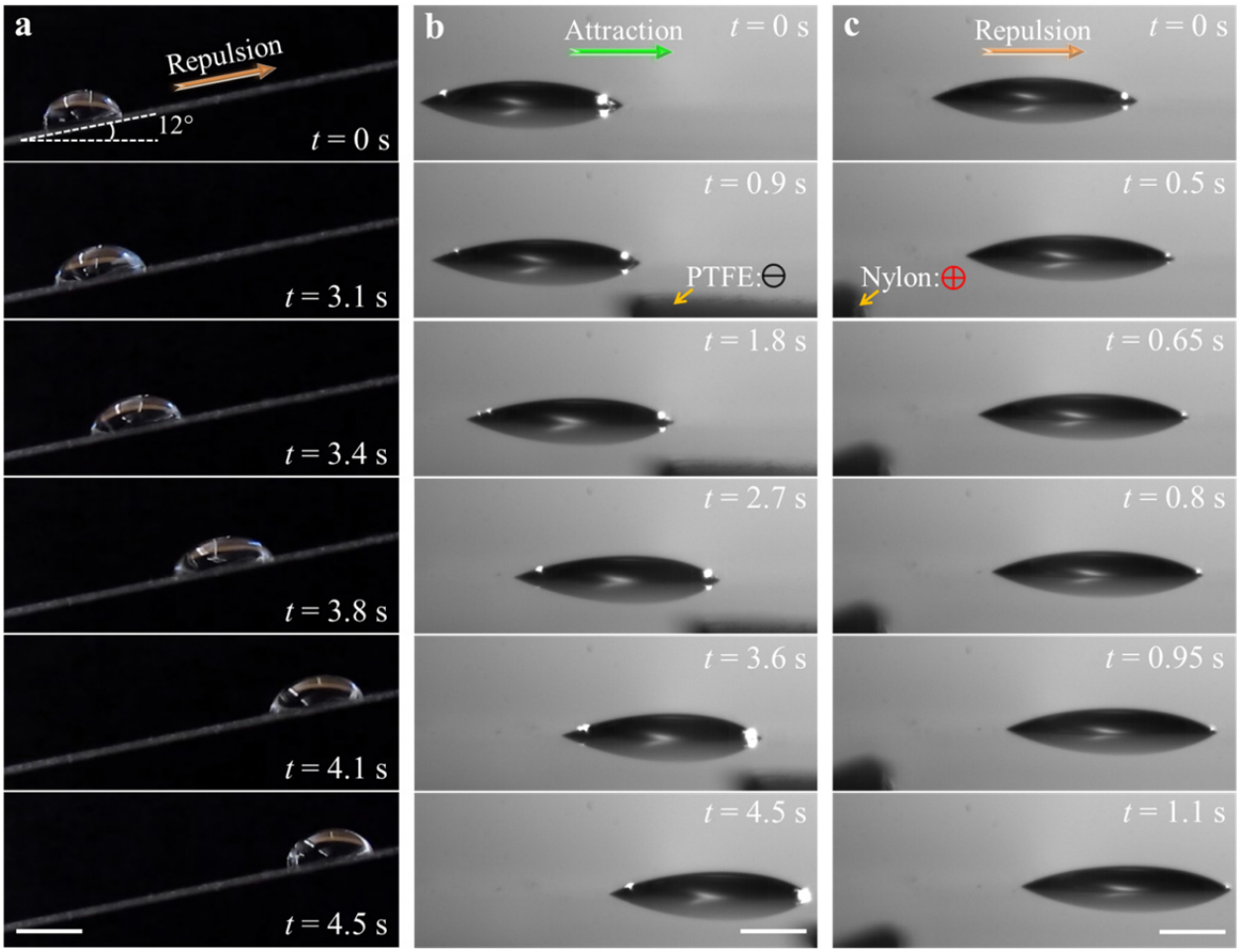

FIGURE 3-7. Droplet manipulation in complex conditions. a) Uphill motion of a water droplet. Scale bar represents 5 mm; **b** and **c)** Attraction and repulsion of a droplet of low dielectric constant (n-hexadecane), respectively, on our slippery surface. Scale bar represents 2 mm.

Our triboelectric-based methodology for droplet manipulation on slippery surfaces can provide a platform to precisely control the droplet motion on solid surfaces, which is of importance for a range of practical applications such as lab-on-a-chip systems, energy harvesting

devices and biomedical applications. For example, droplets of two miscible liquids can be easily mixed in a highly controlled manner. **Figure 3-8a** demonstrates that a charged water droplet is repelled via a nylon (representative of a positively charged) actuator and moved toward an un-charged droplet of toluene (representative of a liquid miscible in water). Upon coalescence, the two miscible droplets mixed with each other. Similarly, **Figure 3-8b** demonstrates that our triboelectric-based methodology can also be employed for coalescence of two immiscible charged and uncharged droplets (e.g., water and n-hexadecane).

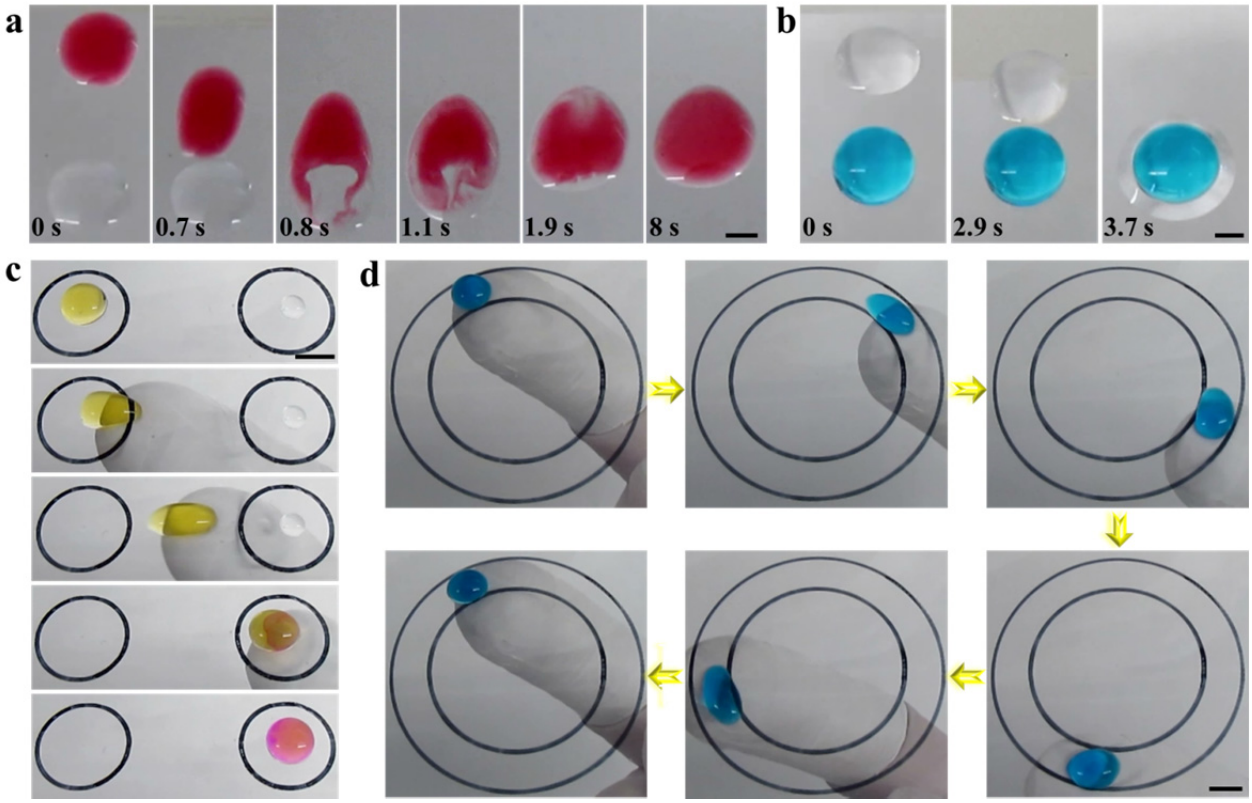

FIGURE 3-8. Potential applications of the triboelectric-based droplet manipulation technique. Selective motion of charged droplets toward un-charged droplets to induce coalescence of two **a)** miscible droplets (water and toluene dyed in red) and **b)** immiscible droplets (n-hexadecane and water dyed in blue). Scale bar represents 2 mm; **c)** Utilization of a finger covered by Teflon tape as an actuator, demonstrating the simplicity of the triboelectric-based droplet manipulation technique; **d)** Highly controlled manipulation of a liquid droplet along a complex path. Black circles are drawn on the back side of the surface. Scale bars in c and d represent 5 mm.

Simplicity is one of the main advantages of our triboelectric-based droplet manipulation technique. **Figure 3-8c** demonstrates that even a finger can act as an actuator to enable the transport of droplets. Here, a basic droplet (with pH ≈ 9.5) was attracted via a finger covered by Teflon tape and transported smoothly toward a droplet of Phenolphthalein (i.e., a pH indicator). Upon coalescence, color of the merged droplet changed to pink indicative of the basic nature of the initial droplet. Note that the dark circles were drawn to better identify the location of the droplets at the onset of the motion. We also demonstrated (see **Figure 3-8d**) the capability of our triboelectric-based mythology to provide a highly controlled manipulation of a liquid droplet along a complex path (i.e., dark circles) using our finger as an actuator, which can attract tremendous interest in lab-on-a-chip devices.

3.2.4. Conclusion

Droplet manipulation has attracted tremendous interest across different scientific fields over the past two decades. However, current droplet manipulation techniques suffer from drawbacks such as complex fabrication of manipulation platforms, or low droplet motility (i.e., long response time), or expensive actuation system, or lack of precise control on droplet motion. In this work, for the first time, we demonstrated controlled manipulation of liquid droplets of both high dielectric strength (e.g., water) and low dielectric strength (e.g., n-hexadecane) on a smooth and slippery surface via triboelectric effect. Our facile and portable methodology enables on-demand, precise manipulation of droplets using solely an electrostatic attract or repulsion force, which is exerted on the droplet by a simple charged actuator (e.g., Teflon sheet). We further demonstrated that even a finger can act as an actuator to enable the transport of droplet. We envision that our simple triboelectric-based droplet manipulation technique will open new avenues for lab-on-a-chip systems, energy harvesting devices and biomedical applications.

4. CHAPTER 4- CONCLUSIONS AND FUTURE WORK

Recent advances in micro/nano-scale fabrication techniques and also chemicals with variety of functionalities have opened up new avenues in tailoring solid-liquid interactions to control the wettability and slipperiness of solid surfaces against contacting droplets. In particular, extensive efforts have been devoted to the investigation of super-repellent surfaces (i.e., surfaces that display extreme repellency to liquids) and also slippery surfaces (i.e., surfaces that allow extreme liquid mobility). The extreme liquid repellency and liquid mobility on such surfaces arises from the combination of appropriate surface texture and surface chemistry. Controlling the surface texture and/or surface chemistry allows tailoring of the solid-liquid interaction to control the droplet wetting and dynamics. Such control on the wetting and dynamics of droplets on solid surfaces is of great interest for industrial applications such as phase-change heat transfer, liquid transportation, anti-fouling, self-cleaning, drag reduction, corrosion control, and manipulation of liquid droplets. The current work summarizes the fundamentals of tailoring the interaction of droplets with textured super-repellent surfaces and also non-textured slippery surfaces and focuses on some of their novel applications. In this chapter, the contributions of this dissertation to fundamental science and applied science are highlighted and the potential aspects of this work for future investigations are discussed.

4.1. Contributions to Fundamental and Applied Sciences

In this work, the following contributions to fundamental science and applied science were made:

(i) Metamorphic Superomniphobic Surfaces:

Contributions to fundamental science: We fabricated the first-ever metamorphic superomniphobic (MorphS) surfaces composed of mushroom-like pillars made of a thermo-responsive shape-memory polymer. We systematically studied the wetting transition of low surface tension and high surface tension liquids on our MorphS surfaces and elucidated the mechanism underlying such transition based on morphology transformation, rather than altering the surface chemistry, which has been shown in prior work.

Contributions to applied science: We demonstrated many cycles of reversible wetting transition on our MorphS surfaces without noticeable change in texture or chemistry of the surfaces. We believe that such reversible wetting transitions on our robust MorphS surfaces will have a wide range of applications including rewritable liquid patterns, hazardous liquid transportation, biochemical assays, liquid-liquid separation membranes, lab-on-a-chip devices, and biosensors.

(ii) Coalescence Induced Self-Propulsion of Droplets on Superomniphobic Surfaces:

Contributions to fundamental science: Utilizing our superomniphobic surfaces, we systematically investigated the different regimes of coalescence-induced self-propulsion for liquids with a wide range of surface tensions in addition to liquids with a wide range of viscosities and droplet radii. Our results indicate in the visco-capillary regime, the non-dimensional jumping velocity V_j^* decreases more rapidly with increasing Ohnesorge number due to decreasing droplet radius than increasing the Ohnesorge number due to increasing viscosity (has not been observed in prior work). This is because decreasing the droplet radius increases the inertial-capillary velocity V_{ic} in addition to increasing the Ohnesorge number. Both the increase

in Ohnesorge number and the increase in inertial-capillary velocity (i.e., two different factors) contribute to a decrease in the non-dimensional jumping velocity with decreasing radius.

Contributions to applied science: We envision that our results will provide the platform and understanding to enable enhanced dropwise condensation of liquids with a wide range of surface tensions or wide range of viscosities.

(iii) Coalescence-induced Jumping of Droplets on Superomniphobic Surfaces with Macrotexture:

Contributions to fundamental science: We developed a simple and passive strategy consisting of superomniphobic surfaces with a protruding macrotexture to experimentally demonstrate coalescence-induced jumping with significantly higher energy conversion efficiency $\eta \approx 18.8\%$. Such high energy conversion efficiency (i.e., about 570% higher efficiency compared to superomniphobic surfaces without a macrotexture) has never been reported before. Our detailed analysis of the droplet dynamics via numerical simulations indicates that underlying mechanism for the significantly higher energy conversion efficiency is the effective redirection of in-plane velocity vectors to out-of-plane velocity vectors due to the presence of the macrotexture. Further, based on a non-dimensional energy balance, we postulate and prove a new physical scaling law (through systematic experiments and numerical simulations), which implies that the upward kinetic energy of the jumping droplet increases linearly with the height of the macrotexture.

Contributions to applied science: We envision that our simple and passive technique will open a new avenue to prevent surface flooding and thus achieve sustained dropwise condensation (especially with liquids of high viscosity and/or low surface tension), which has

been the grand challenge in design and fabrication of ultra-efficient condensers for industrial applications.

(iv) Slippery Hydrophilic (SLIC) Solid Surfaces:

Contributions to fundamental science: We developed a simple "grafting to" technique to fabricate a novel hydrophilic surface that is counterintuitively slippery. We also investigated the influence of physical homogeneity, chemical homogeneity and grafting density of hydrophilic nano-brushes on wettability and slipperiness of such surfaces. Further, we demonstrated a selective surface tension-based slipperiness on our SLIC surface that has not been observed on smooth slippery surfaces so far. In addition, we showed that our surface can retain its slipperiness in environments with a wide range of humidity and thus can be employed in applications like dropwise condensation.

Contributions to applied science: We qualitatively demonstrated that the rate of droplet nucleation and growth on hydrophilic slippery surfaces are significantly higher than hydrophobic slippery surfaces. Combination of very high droplet nucleation and growth rate (aroused by the hydrophilic nature of the surface) with prompt droplet removal (due to the slippery nature of the surface) makes it a viable alternative for state-of-art surfaces used in dropwise condensation. Further, relying on selective slipperiness of our hydrophilic slippery surface against low and high surface tension liquids, we developed the first-ever simple slipperiness-based technique for water-oil separation. Due to such novel properties, we envision that our SLIC surface will attract significant attention in thermal and fluidic research communities and also industrial sectors.

(v) On-demand Droplet Manipulation via Triboelectrification:

Contributions to fundamental science: We demonstrated that a droplet acquired such charge can be actuated using an external actuator and thus move on a slippery surface. We

showed that our controlled and contactless triboelectric-based manipulation technique can be used for both high dielectric strength (e.g., water) and low dielectric strength (e.g., n-hexadecane) droplets. Our facile and portable methodology enables on-demand, precise manipulation of droplets using solely an electrostatic attract or repulsion force, which is exerted on the droplet by a simple charged actuator (e.g., Teflon sheet).

Contributions to applied science: Current droplet manipulation techniques suffer from drawbacks such as complex fabrication of manipulation platform, or low droplet motility (i.e., long response time), or expensive actuation system, or lack of precise control on droplet motion. In contrast, we demonstrated that the triboelectric-based droplet manipulation technique proposed in this work is very simple without any complex fabrication of manipulation platform or expensive actuation system. It also shows precise contactless control with a wide range of liquids. Further, the actuation force can be easily tuned by altering the distance between the droplet and the actuator that combined with high slipperiness of the surface can leads to high mobility the droplets. We envision that our simple triboelectric-based droplet manipulation technique will open a new avenue for lab-on-a-chip systems, energy harvesting devices and biomedical applications.

4.2. Future Work

Perspectives on the unique challenges of this work as well as future directions are presented here.

(i) Textured Super-Repellent Surfaces

Long chain fluorocarbons have been used in fabrication of textured super-repellent surfaces to induce low solid surface energy. However, such materials are being phased out by environmental agencies across the world due to the growing concerns regarding their negative

environmental impacts (e.g., non-biodegradable) and biological impacts (e.g., bioaccumulation).[251] Consequently, future work should be centered on utilization of benign surface chemistries to eliminate such concerns of biodegradability and toxicity. Further, despite the increasing number of reports focused on fabrication of durable super-repellent surfaces, mechanical durability of such surfaces, especially against abrasion, continues to be a grand challenge.[252] Hence, significant efforts still need to be devoted to fabricate micro/nano-scale textures with high deformability and/or self-healing ability to develop durable super-repellent surfaces.

Along with general concerns mentioned above, the projects discussed in this dissertation can be continued in the following directions:

Metamorphic Superomniphobic Surfaces: Wetting transition on our MorphS surfaces requires heating and mechanical compression of the surface. While surface heating can be achieved remotely, mechanical loading entails physical contact with the solid textured surface. Future efforts must be focused on fully remotely-actuated reversibly wetting transition on our MorphS surfaces. Surfaces with remotely-controlled switchable wettability can have numerous implications such as micro-robots used in hazardous liquid transport as well as micro-arrays used for bio-assays.

Coalescence Induced Self-Propulsion of Droplets on Superomniphobic Surfaces: Despite the accuracy of the scaling law (derived based on energy balance) to predict the coalescence-induced jumping velocity of droplets on superomniphobic surfaces in the inertial capillary regime, we demonstrated that such argument fails to predict the velocity of droplets in the visco-capillary regime. Future theoretical, numerical and experimental researches are required to improve the current understanding about the coalescence-induced jumping of

droplets in the visco-capillary regime and developing a new scaling law to predict the jumping velocity.

Coalescence-induced Jumping of Droplets on Superomniphobic Surfaces with Macrotexture: We envision that superior energy conversion efficiency in coalescence-induced jumping of droplets on our surfaces can prevent surface flooding and thus facilitates the dropwise condensation of liquids of high viscosity and/or low surface tension. Future work is required to validate such arguments on surfaces composed of macrotextures (e.g., arrays of ridges). If such surfaces can successfully demonstrate coalescence-induced jumping of droplets with low surface tension and high viscosity and prevent flooding in dropwise condensation in the lab scale, it will open new avenues in design of compact condensers and heat exchangers in various industrial sectors. Further, more scalable techniques to fabricate surfaces composed of required macrotextures need to be developed. In addition, superomniphobic surfaces with macrotexture can be used to control the jumping of coalesced droplets and their directionality to develop ultra-efficient micro heat pipes used in hotspot cooling of micro-devices. Applicability of our scaling law to predict the energy conversion efficiency (or the jumping Webber number) of droplets in the viso-capillary regime also needs to be evaluated.

(ii) Smooth Slippery Surfaces

In contrast to textured super-repellent surfaces, the mechanism underlying the slipperiness of non-textured slippery surfaces is still unclear and future experimental research combined with numerical simulations are required to elucidate the mechanisms of such slipperiness on hydrophobic and hydrophilic surfaces. In addition, influence of wettability (characterized using Young's contact angle) and slipperiness (characterized using contact angle hysteresis or sliding angle) on liquid mobility on such surfaces needs to be investigated in detail. Further, durability

of smooth slippery surfaces in different applications, longevity of their slipperiness in various operating conditions, and also standard storage conditions of these surfaces need to be explored.

Along with general concerns mentioned above, the projects discussed in this dissertation can be continued in the following directions:

Slippery Hydrophilic (SLIC) Solid Surfaces: In this work, we qualitatively explored the influence of wettability and slipperiness on droplet nucleation and growth rate as well as the droplet critical radius. These effects should be investigated quantitatively in detail. In addition, influence of such improvements on the heat transfer coefficient and critical heat flux of dropwise condensation should be quantified. Further, application of our technique to fabricate hydrophilic slippery surfaces using other substrates (e.g., metals and plastics) needs to be investigated. Such metallic slippery hydrophilic materials can be used to develop ultra-efficient thermal equipment such as compact shell & tube heat exchangers and condensers, plate heat exchangers with antifouling properties, and spray cooling used in data centers. Further, due to its hydrophilic and highly slippery nature, they can attract interest in fog harvesting in humid regions.

On-demand Droplet Manipulation via Triboelectrification: Our on-demand droplet manipulation technique relies on the contact electrification at solid-liquid interface. The mechanism of such contact electrification needs to be elucidated. In addition, numerical simulations are required to quantify the attraction and repulsive forces applied to the droplets by the actuators. Further, future research should focus on the application of our simple, controlled and contactless technique to manipulate droplets on lab-on-chip devices.

BIBLIOGRAPHY

1. Bird, J. C.; Dhiman, R.; Kwon, H.-M.; Varanasi, K. K., Reducing the contact time of a bouncing drop. *Nature* **2013,** *503* (7476), 385.
2. Byun, J.; Shin, J.; Kwon, S.; Jang, S.; Kim, J. K., Fast and reversibly switchable wettability induced by a photothermal effect. *Chemical Communications* **2012,** *48* (74), 9278-9280.
3. Kota, A. K.; Kwon, G.; Tuteja, A., The design and applications of superomniphobic surfaces. *NPG Asia Materials* **2014,** *6* (7), e109.
4. Liu, F.; Ghigliotti, G.; Feng, J. J.; Chen, C.-H., Numerical simulations of self-propelled jumping upon drop coalescence on non-wetting surfaces. *Journal of Fluid mechanics* **2014,** *752*, 39-65.
5. Mistura, G.; Pierno, M., Drop mobility on chemically heterogeneous and lubricant-impregnated surfaces. *Advances in Physics: X* **2017,** *2* (3), 591-607.
6. Boreyko, J. B.; Chen, C.-H., Self-propelled dropwise condensate on superhydrophobic surfaces. *Physical review letters* **2009,** *103* (18), 184501.
7. Cheng, M.; Liu, Q.; Ju, G.; Zhang, Y.; Jiang, L.; Shi, F., Bell-Shaped Superhydrophilic–Superhydrophobic–Superhydrophilic Double Transformation on a pH-Responsive Smart Surface. *Advanced Materials* **2014,** *26* (2), 306-310.
8. Enright, R.; Miljkovic, N.; Sprittles, J.; Nolan, K.; Mitchell, R.; Wang, E. N., How coalescing droplets jump. *ACS nano* **2014,** *8* (10), 10352-10362.
9. Sun, T.; Wang, G.; Feng, L.; Liu, B.; Ma, Y.; Jiang, L.; Zhu, D., Reversible switching between superhydrophilicity and superhydrophobicity. *Angewandte Chemie* **2004,** *116* (3), 361-364.
10. Krupenkin, T. N.; Taylor, J. A.; Wang, E. N.; Kolodner, P.; Hodes, M.; Salamon, T. R., Reversible wetting− dewetting transitions on electrically tunable superhydrophobic nanostructured surfaces. *Langmuir* **2007,** *23* (18), 9128-9133.
11. Aria, A. I.; Gharib, M., Reversible tuning of the wettability of carbon nanotube arrays: the effect of ultraviolet/ozone and vacuum pyrolysis treatments. *Langmuir* **2011,** *27* (14), 9005-9011.
12. Huang, X.; Sun, Y.; Soh, S., Stimuli-Responsive Surfaces for Tunable and Reversible Control of Wettability. *Advanced Materials* **2015,** *27* (27), 4062-4068.
13. Zheng, L.; Sundaram, H. S.; Wei, Z.; Li, C.; Yuan, Z., Applications of zwitterionic polymers. *Reactive and Functional Polymers* **2017,** *118*, 51-61.
14. Bhushan, B.; Jung, Y. C.; Koch, K., Self-cleaning efficiency of artificial superhydrophobic surfaces. *Langmuir* **2009,** *25* (5), 3240-3248.
15. Fürstner, R.; Barthlott, W.; Neinhuis, C.; Walzel, P., Wetting and self-cleaning properties of artificial superhydrophobic surfaces. *Langmuir* **2005,** *21* (3), 956-961.
16. Nishimoto, S.; Bhushan, B., Bioinspired self-cleaning surfaces with superhydrophobicity, superoleophobicity, and superhydrophilicity. *Rsc Advances* **2013,** *3* (3), 671-690.
17. Wisdom, K. M.; Watson, J. A.; Qu, X.; Liu, F.; Watson, G. S.; Chen, C.-H., Self-cleaning of superhydrophobic surfaces by self-propelled jumping condensate. *Proceedings of the National Academy of Sciences* **2013,** *110* (20), 7992-7997.

18. Bhushan, B.; Jung, Y. C., Natural and biomimetic artificial surfaces for superhydrophobicity, self-cleaning, low adhesion, and drag reduction. *Progress in Materials Science* **2011,** *56* (1), 1-108.
19. Daniello, R. J.; Waterhouse, N. E.; Rothstein, J. P., Drag reduction in turbulent flows over superhydrophobic surfaces. *Physics of Fluids* **2009,** *21* (8), 085103.
20. Ou, J.; Perot, B.; Rothstein, J. P., Laminar drag reduction in microchannels using ultrahydrophobic surfaces. *Physics of fluids* **2004,** *16* (12), 4635-4643.
21. Bark, D. L.; Vahabi, H.; Bui, H.; Movafaghi, S.; Moore, B.; Kota, A. K.; Popat, K.; Dasi, L. P., Hemodynamic performance and thrombogenic properties of a superhydrophobic bileaflet mechanical heart valve. *Annals of biomedical engineering* **2017,** *45* (2), 452-463.
22. Bark, D.; Vahabi, H.; Movafaghi, S.; Popat, K.; Kota, A. K.; Dasi, L. P. In *Superhydrophobicity to minimize thrombogenic risk on mechanical heart valves*, APS Division of Fluid Dynamics Meeting Abstracts, 2017.
23. Pan, S.; Kota, A. K.; Mabry, J. M.; Tuteja, A., Superomniphobic surfaces for effective chemical shielding. *Journal of the American Chemical Society* **2012,** *135* (2), 578-581.
24. Vahabi, H.; Wang, W.; Movafaghi, S.; Kota, A. K., Free-Standing, Flexible, Superomniphobic Films. *ACS Applied Materials & Interfaces* **2016,** *8* (34), 21962-21967.
25. Jafari, R.; Menini, R.; Farzaneh, M., Superhydrophobic and icephobic surfaces prepared by RF-sputtered polytetrafluoroethylene coatings. *Applied Surface Science* **2010,** *257* (5), 1540-1543.
26. Varanasi, K. K.; Deng, T.; Smith, J. D.; Hsu, M.; Bhate, N., Frost formation and ice adhesion on superhydrophobic surfaces. *Applied Physics Letters* **2010,** *97* (23), 234102.
27. Boreyko, J. B.; Collier, C. P., Delayed frost growth on jumping-drop superhydrophobic surfaces. *ACS nano* **2013,** *7* (2), 1618-1627.
28. Beemer, D. L.; Wang, W.; Kota, A. K., Durable gels with ultra-low adhesion to ice. *Journal of Materials Chemistry A* **2016,** *4* (47), 18253-18258.
29. Jiang, L.; Yao, X.; Li, H.; Fu, Y.; Chen, L.; Meng, Q.; Hu, W.; Jiang, L., "Water Strider" Legs with a Self-Assembled Coating of Single-Crystalline Nanowires of an Organic Semiconductor. *Advanced Materials* **2010,** *22* (3), 376-379.
30. Zhang, X.; Zhao, J.; Zhu, Q.; Chen, N.; Zhang, M.; Pan, Q., Bioinspired aquatic microrobot capable of walking on water surface like a water strider. *ACS applied materials & interfaces* **2011,** *3* (7), 2630-2636.
31. Koh, J.-S.; Yang, E.; Jung, G.-P.; Jung, S.-P.; Son, J. H.; Lee, S.-I.; Jablonski, P. G.; Wood, R. J.; Kim, H.-Y.; Cho, K.-J., Jumping on water: Surface tension–dominated jumping of water striders and robotic insects. *Science* **2015,** *349* (6247), 517-521.
32. Liu, T.; Chen, S.; Cheng, S.; Tian, J.; Chang, X.; Yin, Y., Corrosion behavior of super-hydrophobic surface on copper in seawater. *Electrochimica Acta* **2007,** *52* (28), 8003-8007.
33. Isimjan, T. T.; Wang, T.; Rohani, S., A novel method to prepare superhydrophobic, UV resistance and anti-corrosion steel surface. *Chemical engineering journal* **2012,** *210*, 182-187.
34. Fang, G.; Li, W.; Wang, X.; Qiao, G., Droplet motion on designed microtextured superhydrophobic surfaces with tunable wettability. *Langmuir* **2008,** *24* (20), 11651-11660.
35. Zhao, Y.; Fang, J.; Wang, H.; Wang, X.; Lin, T., Magnetic liquid marbles: manipulation of liquid droplets using highly hydrophobic Fe3O4 nanoparticles. *Advanced materials* **2010,** *22* (6), 707-710.

36. Movafaghi, S.; Cackovic, M. D.; Wang, W.; Vahabi, H.; Pendurthi, A.; Henry, C. S.; Kota, A. K., Superomniphobic Papers for On-Paper pH Sensors. *Advanced Materials Interfaces* **2019**, 1900232.
37. Li, X.-M.; Reinhoudt, D.; Crego-Calama, M., What do we need for a superhydrophobic surface? A review on the recent progress in the preparation of superhydrophobic surfaces. *Chemical Society Reviews* **2007,** *36* (8), 1350-1368.
38. Kota, A. K.; Choi, W.; Tuteja, A., Superomniphobic surfaces: design and durability. *MRS bulletin* **2013,** *38* (5), 383-390.
39. Quéré, D., Wetting and roughness. *Annu. Rev. Mater. Res.* **2008,** *38*, 71-99.
40. Chu, Z.; Seeger, S., Superamphiphobic surfaces. *Chemical Society Reviews* **2014,** *43* (8), 2784-2798.
41. Yong, J.; Chen, F.; Yang, Q.; Huo, J.; Hou, X., Superoleophobic surfaces. *Chemical Society Reviews* **2017,** *46* (14), 4168-4217.
42. Nosonovsky, M.; Bhushan, B., Superhydrophobic surfaces and emerging applications: non-adhesion, energy, green engineering. *Current Opinion in Colloid & Interface Science* **2009,** *14* (4), 270-280.
43. Young, T., III. An essay on the cohesion of fluids. *Philosophical transactions of the royal society of London* **1805,** *95*, 65-87.
44. Wenzel, R. N., RESISTANCE OF SOLID SURFACES TO WETTING BY WATER. *Industrial & Engineering Chemistry* **1936,** *28* (8), 988-994.
45. Cassie, A.; Baxter, S., Wettability of porous surfaces. *Transactions of the Faraday society* **1944,** *40*, 546-551.
46. Vahabi, H.; Wang, W.; Popat, K. C.; Kwon, G.; Holland, T. B.; Kota, A. K., Metallic superhydrophobic surfaces via thermal sensitization. *Applied Physics Letters* **2017,** *110* (25), 251602.
47. Wang, W.; Lockwood, K.; Boyd, L. M.; Davidson, M. D.; Movafaghi, S.; Vahabi, H.; Khetani, S. R.; Kota, A. K., Superhydrophobic coatings with edible materials. *ACS applied materials & interfaces* **2016,** *8* (29), 18664-18668.
48. Johnson Jr, R. E.; Dettre, R. H., Contact angle hysteresis. III. Study of an idealized heterogeneous surface. *The journal of physical chemistry* **1964,** *68* (7), 1744-1750.
49. Dettre, R. H.; Johnson Jr, R. E., Contact Angle Hysteresis. IV. Contact Angle Measurements on Heterogeneous Surfaces1. *The journal of physical chemistry* **1965,** *69* (5), 1507-1515.
50. Eral, H.; Oh, J., Contact angle hysteresis: a review of fundamentals and applications. *Colloid and polymer science* **2013,** *291* (2), 247-260.
51. Extrand, C., A thermodynamic model for contact angle hysteresis. *Journal of Colloid and interface Science* **1998,** *207* (1), 11-19.
52. Makkonen, L., A thermodynamic model of contact angle hysteresis. *The Journal of Chemical Physics* **2017,** *147* (6), 064703.
53. Tadmor, R.; Das, R.; Gulec, S.; Liu, J.; E. N'guessan, H.; Shah, M.; S. Wasnik, P.; Yadav, S. B., Solid–liquid work of adhesion. *Langmuir* **2017,** *33* (15), 3594-3600.
54. Lafuma, A.; Quéré, D., Superhydrophobic states. *Nature materials* **2003,** *2* (7), 457.
55. Patankar, N. A., On the modeling of hydrophobic contact angles on rough surfaces. *Langmuir* **2003,** *19* (4), 1249-1253.
56. Gao, L.; McCarthy, T. J., The "lotus effect" explained: two reasons why two length scales of topography are important. *Langmuir* **2006,** *22* (7), 2966-2967.

57. Tuteja, A.; Choi, W.; Ma, M.; Mabry, J. M.; Mazzella, S. A.; Rutledge, G. C.; McKinley, G. H.; Cohen, R. E., Designing superoleophobic surfaces. *Science* **2007,** *318* (5856), 1618-1622.
58. Tuteja, A.; Choi, W.; Mabry, J. M.; McKinley, G. H.; Cohen, R. E., Robust omniphobic surfaces. *Proceedings of the National Academy of Sciences* **2008,** *105* (47), 18200-18205.
59. Zhao, H.; Law, K.-Y.; Sambhy, V., Fabrication, surface properties, and origin of superoleophobicity for a model textured surface. *Langmuir* **2011,** *27* (10), 5927-5935.
60. Kota, A. K.; Li, Y.; Mabry, J. M.; Tuteja, A., Hierarchically structured superoleophobic surfaces with ultralow contact angle hysteresis. *Advanced materials* **2012,** *24* (43), 5838-5843.
61. Liu, T.; Kim, C.-J., Turning a surface superrepellent even to completely wetting liquids. **2014**.
62. Miwa, M.; Nakajima, A.; Fujishima, A.; Hashimoto, K.; Watanabe, T., Effects of the surface roughness on sliding angles of water droplets on superhydrophobic surfaces. *Langmuir* **2000,** *16* (13), 5754-5760.
63. Hare, E.; Shafrin, E.; Zisman, W., Properties of films of adsorbed fluorinated acids. *The Journal of physical chemistry* **1954,** *58* (3), 236-239.
64. Arkles, B., Hydrophobicity, hydrophilicity and silane surface modification. *Gelest Inc, Morrisville* **2011**.
65. Drelich, J.; Chibowski, E.; Meng, D. D.; Terpilowski, K., Hydrophilic and superhydrophilic surfaces and materials. *Soft Matter* **2011,** *7* (21), 9804-9828.
66. Zhu, Z.; Zheng, S.; Peng, S.; Zhao, Y.; Tian, Y., Superlyophilic Interfaces and Their Applications. *Advanced Materials* **2017,** *29* (45), 1703120.
67. Marmur, A., From hygrophilic to superhygrophobic: theoretical conditions for making high-contact-angle surfaces from low-contact-angle materials. *Langmuir* **2008,** *24* (14), 7573-7579.
68. Marmur, A., Wetting on hydrophobic rough surfaces: to be heterogeneous or not to be? *Langmuir* **2003,** *19* (20), 8343-8348.
69. Nosonovsky, M., Multiscale roughness and stability of superhydrophobic biomimetic interfaces. *Langmuir* **2007,** *23* (6), 3157-3161.
70. Su, Y.; Ji, B.; Huang, Y.; Hwang, K.-c., Nature's design of hierarchical superhydrophobic surfaces of a water strider for low adhesion and low-energy dissipation. *Langmuir* **2010,** *26* (24), 18926-18937.
71. Wong, T.-S.; Kang, S. H.; Tang, S. K.; Smythe, E. J.; Hatton, B. D.; Grinthal, A.; Aizenberg, J., Bioinspired self-repairing slippery surfaces with pressure-stable omniphobicity. *Nature* **2011,** *477* (7365), 443.
72. Lafuma, A.; Quéré, D., Slippery pre-suffused surfaces. *EPL (Europhysics Letters)* **2011,** *96* (5), 56001.
73. Xiao, R.; Miljkovic, N.; Enright, R.; Wang, E. N., Immersion condensation on oil-infused heterogeneous surfaces for enhanced heat transfer. *Scientific reports* **2013,** *3*, 1988.
74. Kim, P.; Wong, T.-S.; Alvarenga, J.; Kreder, M. J.; Adorno-Martinez, W. E.; Aizenberg, J., Liquid-infused nanostructured surfaces with extreme anti-ice and anti-frost performance. *ACS nano* **2012,** *6* (8), 6569-6577.
75. Glavan, A. C.; Martinez, R. V.; Subramaniam, A. B.; Yoon, H. J.; Nunes, R.; Lange, H.; Thuo, M. M.; Whitesides, G. M., Omniphobic "RF paper" produced by silanization of paper with fluoroalkyltrichlorosilanes. *Advanced Functional Materials* **2014,** *24* (1), 60-70.
76. Rykaczewski, K.; Paxson, A. T.; Staymates, M.; Walker, M. L.; Sun, X.; Anand, S.; Srinivasan, S.; McKinley, G. H.; Chinn, J.; Scott, J. H. J., Dropwise condensation of low surface tension fluids on omniphobic surfaces. *Scientific reports* **2014,** *4*, 4158.

77. Wang, L.; McCarthy, T. J., Covalently attached liquids: instant omniphobic surfaces with unprecedented repellency. *Angewandte Chemie* **2016,** *128* (1), 252-256.
78. Daniel, D.; Timonen, J. V.; Li, R.; Velling, S. J.; Aizenberg, J., Oleoplaning droplets on lubricated surfaces. *Nature Physics* **2017,** *13* (10), 1020.
79. Kaschiev, D., *Nucleation: Basic Theory With Applications*. Butterworth Heinemann: Oxford, 2000.
80. Rose, J., Dropwise condensation theory and experiment: a review. *Proceedings of the Institution of Mechanical Engineers, Part A: Journal of Power and Energy* **2002,** *216* (2), 115-128.
81. Khan, S.; Atieh, M.; Koç, M., Micro-nano scale surface coating for nucleate boiling heat transfer: A critical review. *Energies* **2018,** *11* (11), 3189.
82. Barrat, J.-L.; Chiaruttini, F., Kapitza resistance at the liquid—solid interface. *Molecular Physics* **2003,** *101* (11), 1605-1610.
83. Zhang, P.; Lin, L.; Zang, D.; Guo, X.; Liu, M., Designing Bioinspired Anti-Biofouling Surfaces based on a Superwettability Strategy. *Small* **2017,** *13* (4), 1503334.
84. Guo, F.; Guo, Z., Inspired smart materials with external stimuli responsive wettability: a review. *RSC Advances* **2016,** *6* (43), 36623-36641.
85. Kim, Y. J.; Ebara, M.; Aoyagi, T., A smart hyperthermia nanofiber with switchable drug release for inducing cancer apoptosis. *Advanced Functional Materials* **2013,** *23* (46), 5753-5761.
86. Kim, Y. J.; Ebara, M.; Aoyagi, T., A smart nanofiber web that captures and releases cells. *Angewandte Chemie International Edition* **2012,** *51* (42), 10537-10541.
87. Kota, A. K.; Kwon, G.; Choi, W.; Mabry, J. M.; Tuteja, A., Hygro-responsive membranes for effective oil–water separation. *Nature communications* **2012,** *3*, 1025.
88. Chapman, J.; Regan, F., Nanofunctionalized superhydrophobic antifouling coatings for environmental sensor applications—advancing deployment with answers from nature. *Advanced Engineering Materials* **2012,** *14* (4).
89. Yu, X.; Wang, Z.; Jiang, Y.; Shi, F.; Zhang, X., Reversible pH-Responsive Surface: From Superhydrophobicity to Superhydrophilicity. *Advanced Materials* **2005,** *17* (10), 1289-1293.
90. Minko, S.; Müller, M.; Motornov, M.; Nitschke, M.; Grundke, K.; Stamm, M., Two-level structured self-adaptive surfaces with reversibly tunable properties. *Journal of the American Chemical Society* **2003,** *125* (13), 3896-3900.
91. Lim, H. S.; Kwak, D.; Lee, D. Y.; Lee, S. G.; Cho, K., UV-driven reversible switching of a roselike vanadium oxide film between superhydrophobicity and superhydrophilicity. *Journal of the American Chemical Society* **2007,** *129* (14), 4128-4129.
92. Song, W.; Veiga, D. D.; Custódio, C. A.; Mano, J. F., Bioinspired degradable substrates with extreme wettability properties. *Advanced Materials* **2009,** *21* (18), 1830-1834.
93. Zhang, J.; Lu, X.; Huang, W.; Han, Y., Reversible superhydrophobicity to superhydrophilicity transition by extending and unloading an elastic polyamide film. *Macromolecular rapid communications* **2005,** *26* (6), 477-480.
94. Wang, Y.; Ma, K.; Xin, J. H., Stimuli-Responsive Bioinspired Materials for Controllable Liquid Manipulation: Principles, Fabrication, and Applications. *Advanced Functional Materials* **2018**.
95. Popova, A. A.; Schillo, S. M.; Demir, K.; Ueda, E.; Nesterov-Mueller, A.; Levkin, P. A., Droplet-Array (DA) Sandwich Chip: A Versatile Platform for High-Throughput Cell Screening Based on Superhydrophobic–Superhydrophilic Micropatterning. *Advanced Materials* **2015,** *27* (35), 5217-5222.

96. Zhang, Y.; Park, S.; Liu, K.; Tsuan, J.; Yang, S.; Wang, T.-H., A surface topography assisted droplet manipulation platform for biomarker detection and pathogen identification. *Lab on a Chip* **2011,** *11* (3), 398-406.
97. Liu, P.; Chin, L.; Ser, W.; Chen, H.; Hsieh, C.-M.; Lee, C.-H.; Sung, K.-B.; Ayi, T.; Yap, P.; Liedberg, B., Cell refractive index for cell biology and disease diagnosis: past, present and future. *Lab on a Chip* **2016,** *16* (4), 634-644.
98. Lv, J.-a.; Liu, Y.; Wei, J.; Chen, E.; Qin, L.; Yu, Y., Photocontrol of fluid slugs in liquid crystal polymer microactuators. *Nature* **2016,** *537* (7619), 179.
99. Dussan, E., On the ability of drops or bubbles to stick to non-horizontal surfaces of solids. Part 2. Small drops or bubbles having contact angles of arbitrary size. *J. Fluid Mech* **1985,** *151* (1).
100. Furmidge, C., Studies at phase interfaces. I. The sliding of liquid drops on solid surfaces and a theory for spray retention. *Journal of colloid science* **1962,** *17* (4), 309-324.
101. Hao, C.; Liu, Y.; Chen, X.; Li, J.; Zhang, M.; Zhao, Y.; Wang, Z., Bioinspired interfacial materials with enhanced drop mobility: From fundamentals to multifunctional applications. *Small* **2016,** *12* (14), 1825-1839.
102. Biance, A.-L.; Chevy, F.; Clanet, C.; Lagubeau, G.; Quéré, D., On the elasticity of an inertial liquid shock. *Journal of Fluid Mechanics* **2006,** *554*, 47-66.
103. Clanet, C.; Béguin, C.; Richard, D.; Quéré, D., Maximal deformation of an impacting drop. *Journal of Fluid Mechanics* **2004,** *517*, 199-208.
104. Fedorchenko, A. I.; Wang, A.-B.; Wang, Y.-H., Effect of capillary and viscous forces on spreading of a liquid drop impinging on a solid surface. *Physics of Fluids* **2005,** *17* (9), 093104.
105. Bennett, T.; Poulikakos, D., Splat-quench solidification: estimating the maximum spreading of a droplet impacting a solid surface. *Journal of Materials Science* **1993,** *28* (4), 963-970.
106. Deng, X.; Schellenberger, F.; Papadopoulos, P.; Vollmer, D.; Butt, H.-J. r., Liquid drops impacting superamphiphobic coatings. *Langmuir* **2013,** *29* (25), 7847-7856.
107. Reyssat, M.; Pépin, A.; Marty, F.; Chen, Y.; Quéré, D., Bouncing transitions on microtextured materials. *EPL (Europhysics Letters)* **2006,** *74* (2), 306.
108. Cassie, A., Contact angles. *Discussions of the Faraday society* **1948,** *3*, 11-16.
109. Zang, D.; Zhang, W.; Song, J.; Chen, Z.; Zhang, Y.; Geng, X.; Chen, F., Rejuvenated bouncing of non-Newtonian droplet via nanoparticle enwrapping. *Applied Physics Letters* **2014,** *105* (23), 231603.
110. Aarts, D. G.; Lekkerkerker, H. N.; Guo, H.; Wegdam, G. H.; Bonn, D., Hydrodynamics of droplet coalescence. *Physical review letters* **2005,** *95* (16), 164503.
111. Cheng, Y.; Xu, J.; Sui, Y., Numerical investigation of coalescence-induced droplet jumping on superhydrophobic surfaces for efficient dropwise condensation heat transfer. *International Journal of Heat and Mass Transfer* **2016,** *95*, 506-516.
112. Cha, H.; Xu, C.; Sotelo, J.; Chun, J. M.; Yokoyama, Y.; Enright, R.; Miljkovic, N., Coalescence-induced nanodroplet jumping. *Physical Review Fluids* **2016,** *1* (6), 064102.
113. Liu, F.; Ghigliotti, G.; Feng, J. J.; Chen, C.-H., Self-propelled jumping upon drop coalescence on Leidenfrost surfaces. *Journal of Fluid Mechanics* **2014,** *752*, 22-38.
114. Nam, Y.; Kim, H.; Shin, S., Energy and hydrodynamic analyses of coalescence-induced jumping droplets. *Applied Physics Letters* **2013,** *103* (16), 161601.
115. Nam, Y.; Seo, D.; Lee, C.; Shin, S., Droplet coalescence on water repellant surfaces. *Soft Matter* **2015,** *11* (1), 154-160.

116.Kim, M.-K.; Cha, H.; Birbarah, P.; Chavan, S.; Zhong, C.; Xu, Y.; Miljkovic, N., Enhanced jumping-droplet departure. *Langmuir* **2015,** *31* (49), 13452-13466.
117.Narhe, R. D.; Khandkar, M.; Shelke, P.; Limaye, A.; Beysens, D. A., Condensation-induced jumping water drops. *Physical Review E* **2009,** *80* (3), 031604.
118.Vahabi, H.; Wang, W.; Davies, S.; Mabry, J. M.; Kota, A. K., Coalescence-induced self-propulsion of droplets on superomniphobic surfaces. *ACS applied materials & interfaces* **2017,** *9* (34), 29328-29336.
119.Rykaczewski, K.; Paxson, A. T.; Staymates, M.; Walker, M. L.; Sun, X.; Anand, S.; Srinivasan, S.; McKinley, G. H.; Chinn, J.; Scott, J. H. J., Dropwise condensation of low surface tension fluids on omniphobic surfaces. *Scientific reports* **2014,** *4*.
120.Lv, C.; Hao, P.; Yao, Z.; Niu, F., Departure of condensation droplets on superhydrophobic surfaces. *Langmuir* **2015,** *31* (8), 2414-2420.
121.Hong, J.; Lee, S. J., Detaching droplets in immiscible fluids from a solid substrate with the help of electrowetting. *Lab on a Chip* **2015,** *15* (3), 900-907.
122.Schutzius, T. M.; Jung, S.; Maitra, T.; Graeber, G.; Köhme, M.; Poulikakos, D., Spontaneous droplet trampolining on rigid superhydrophobic surfaces. *Nature* **2015,** *527* (7576), 82.
123.Wang, W.; Salazar, J.; Vahabi, H.; Joshi-Imre, A.; Voit, W. E.; Kota, A. K., Metamorphic superomniphobic surfaces. *Advanced Materials* **2017,** *29* (27).
124.Lendlein, A.; Langer, R., Biodegradable, elastic shape-memory polymers for potential biomedical applications. *Science* **2002,** *296* (5573), 1673-1676.
125.Ware, T.; Simon, D.; Arreaga-Salas, D. E.; Reeder, J.; Rennaker, R.; Keefer, E. W.; Voit, W., Fabrication of responsive, softening neural interfaces. *Advanced Functional Materials* **2012,** *22* (16), 3470-3479.
126.Yakacki, C. M.; Shandas, R.; Lanning, C.; Rech, B.; Eckstein, A.; Gall, K., Unconstrained recovery characterization of shape-memory polymer networks for cardiovascular applications. *Biomaterials* **2007,** *28* (14), 2255-2263.
127.Grigoryev, A.; Tokarev, I.; Kornev, K. G.; Luzinov, I.; Minko, S., Superomniphobic magnetic microtextures with remote wetting control. *Journal of the American Chemical Society* **2012,** *134* (31), 12916-12919.
128.Heng, L.; Guo, T.; Wang, B.; Fan, L.-Z.; Jiang, L., In situ electric-driven reversible switching of water-droplet adhesion on a superhydrophobic surface. *Journal of Materials Chemistry A* **2015,** *3* (47), 23699-23706.
129.Verho, T.; Korhonen, J. T.; Sainiemi, L.; Jokinen, V.; Bower, C.; Franze, K.; Franssila, S.; Andrew, P.; Ikkala, O.; Ras, R. H., Reversible switching between superhydrophobic states on a hierarchically structured surface. *Proceedings of the National Academy of Sciences* **2012,** *109* (26), 10210-10213.
130.Verplanck, N.; Galopin, E.; Camart, J.-C.; Thomy, V.; Coffinier, Y.; Boukherroub, R., Reversible electrowetting on superhydrophobic silicon nanowires. *Nano letters* **2007,** *7* (3), 813-817.
131.Simon, D.; Ware, T.; Marcotte, R.; Lund, B. R.; Smith, D. W.; Di Prima, M.; Rennaker, R. L.; Voit, W., A comparison of polymer substrates for photolithographic processing of flexible bioelectronics. *Biomedical microdevices* **2013,** *15* (6), 925-939.
132.Lee, E.; Yang, S., Bio-inspired responsive polymer pillar arrays. *MRS Communications* **2015,** *5* (2), 97-114.
133.Xie, T., Recent advances in polymer shape memory. *Polymer* **2011,** *52* (22), 4985-5000.

134.Meng, H.; Li, G., A review of stimuli-responsive shape memory polymer composites. *Polymer* **2013,** *54* (9), 2199-2221.
135.Chen, C. M.; Yang, S., Directed water shedding on high-aspect-ratio shape memory polymer micropillar arrays. *Advanced materials* **2014,** *26* (8), 1283-1288.
136.Lv, T.; Cheng, Z.; Zhang, E.; Kang, H.; Liu, Y.; Jiang, L., Self-Restoration of Superhydrophobicity on Shape Memory Polymer Arrays with Both Crushed Microstructure and Damaged Surface Chemistry. *Small* **2016**.
137.Lv, T.; Cheng, Z.; Zhang, D.; Zhang, E.; Zhao, Q.; Liu, Y.; Jiang, L., Superhydrophobic Surface With Shape Memory Micro/Nanostructure and Its Application in Rewritable Chip for Droplet Storage. *ACS nano* **2016,** *10* (10), 9379-9386.
138.Öner, D.; McCarthy, T. J., Ultrahydrophobic surfaces. Effects of topography length scales on wettability. *Langmuir* **2000,** *16* (20), 7777-7782.
139.Dorrer, C.; Rühe, J., Advancing and receding motion of droplets on ultrahydrophobic post surfaces. *Langmuir* **2006,** *22* (18), 7652-7657.
140.Zhao, H.; Park, K.-C.; Law, K.-Y., Effect of surface texturing on superoleophobicity, contact angle hysteresis, and "robustness". *Langmuir* **2012,** *28* (42), 14925-14934.
141.Liu, T.; Kim, C., Turning a surface superrepellent even to completely wetting liquids. *Science* **2014,** *346* (6213), 1096-1100.
142.Ware, T. H.; McConney, M. E.; Wie, J. J.; Tondiglia, V. P.; White, T. J., Voxelated liquid crystal elastomers. *Science* **2015,** *347* (6225), 982-984.
143.Yakacki, C.; Saed, M.; Nair, D.; Gong, T.; Reed, S.; Bowman, C., Tailorable and programmable liquid-crystalline elastomers using a two-stage thiol–acrylate reaction. *RSC Advances* **2015,** *5* (25), 18997-19001.
144.Behl, M.; Kratz, K.; Zotzmann, J.; Nöchel, U.; Lendlein, A., Reversible Bidirectional Shape-Memory Polymers. *Advanced Materials* **2013,** *25* (32), 4466-4469.
145.Razzaq, M. Y.; Behl, M.; Kratz, K.; Lendlein, A., Multifunctional hybrid nanocomposites with magnetically controlled reversible shape–memory effect. *Advanced Materials* **2013,** *25* (40), 5730-5733.
146.Watson, J. A.; Cribb, B. W.; Hu, H.-M.; Watson, G. S., A dual layer hair array of the brown lacewing: repelling water at different length scales. *Biophysical journal* **2011,** *100* (4), 1149-1155.
147.Enright, R.; Miljkovic, N.; Alvarado, J. L.; Kim, K.; Rose, J. W., Dropwise condensation on micro-and nanostructured surfaces. *Nanoscale and Microscale Thermophysical Engineering* **2014,** *18* (3), 223-250.
148.Miljkovic, N.; Wang, E. N., Condensation heat transfer on superhydrophobic surfaces. *MRS bulletin* **2013,** *38* (5), 397-406.
149.Attinger, D.; Frankiewicz, C.; Betz, A. R.; Schutzius, T. M.; Ganguly, R.; Das, A.; Kim, C.-J.; Megaridis, C. M., Surface engineering for phase change heat transfer: A review. *MRS Energy & Sustainability-A Review Journal* **2014,** *1*.
150.Cho, H. J.; Preston, D. J.; Zhu, Y.; Wang, E. N., Nanoengineered materials for liquid–vapour phase-change heat transfer. *Nature Reviews Materials* **2016,** *2*, 16092.
151.Miljkovic, N.; Enright, R.; Nam, Y.; Lopez, K.; Dou, N.; Sack, J.; Wang, E. N., Jumping-droplet-enhanced condensation on scalable superhydrophobic nanostructured surfaces. *Nano letters* **2012,** *13* (1), 179-187.
152.Enright, R.; Miljkovic, N.; Dou, N.; Nam, Y.; Wang, E. N., Condensation on superhydrophobic copper oxide nanostructures. *Journal of Heat Transfer* **2013,** *135* (9), 091304.

153.Rykaczewski, K.; Scott, J. H. J., Methodology for imaging nano-to-microscale water condensation dynamics on complex nanostructures. *Acs Nano* **2011,** *5* (7), 5962-5968.
154.Rykaczewski, K., Microdroplet growth mechanism during water condensation on superhydrophobic surfaces. *Langmuir* **2012,** *28* (20), 7720-7729.
155.Enright, R.; Miljkovic, N.; Al-Obeidi, A.; Thompson, C. V.; Wang, E. N., Condensation on superhydrophobic surfaces: the role of local energy barriers and structure length scale. *Langmuir* **2012,** *28* (40), 14424-14432.
156.Miljkovic, N.; Enright, R.; Wang, E. N., Effect of droplet morphology on growth dynamics and heat transfer during condensation on superhydrophobic nanostructured surfaces. *ACS nano* **2012,** *6* (2), 1776-1785.
157.Miljkovic, N.; Preston, D. J.; Enright, R.; Wang, E. N., Electric-field-enhanced condensation on superhydrophobic nanostructured surfaces. *ACS nano* **2013,** *7* (12), 11043-11054.
158.Zhang, Q.; He, M.; Chen, J.; Wang, J.; Song, Y.; Jiang, L., Anti-icing surfaces based on enhanced self-propelled jumping of condensed water microdroplets. *Chemical Communications* **2013,** *49* (40), 4516-4518.
159.Yan, X.; Zhang, L.; Sett, S.; Feng, L.; Zhao, C.; Huang, Z.; Vahabi, H.; Kota, A. K.; Chen, F.; Miljkovic, N., Droplet Jumping: Effects of Droplet Size, Surface Structure, Pinning, and Liquid Properties. *ACS nano* **2019**.
160.Wang, F.-C.; Yang, F.; Zhao, Y.-P., Size effect on the coalescence-induced self-propelled droplet. *Applied Physics Letters* **2011,** *98* (5), 053112.
161.McKinley, G. H.; Renardy, M., Wolfgang von ohnesorge. *Physics of Fluids* **2011,** *23* (12), 127101.
162.Rykaczewski, K.; Paxson, A. T.; Anand, S.; Chen, X.; Wang, Z.; Varanasi, K. K., Multimode multidrop serial coalescence effects during condensation on hierarchical superhydrophobic surfaces. *Langmuir* **2013,** *29* (3), 881-891.
163.Chen, X.; Patel, R. S.; Weibel, J. A.; Garimella, S. V., Coalescence-Induced Jumping of Multiple Condensate Droplets on Hierarchical Superhydrophobic Surfaces. *Scientific reports* **2016,** *6*.
164.Kota, A. K.; Mabry, J. M.; Tuteja, A., Superoleophobic surfaces: design criteria and recent studies. *Surface Innovations* **2013,** *1* (2), 71-83.
165.Wang, B.-B.; Zhao, Y.-P.; Yu, T., Fabrication of novel superhydrophobic surfaces and droplet bouncing behavior—part 2: water droplet impact experiment on superhydrophobic surfaces constructed using ZnO nanoparticles. *Journal of adhesion science and technology* **2011,** *25* (1-3), 93-108.
166.Okumura, K.; Chevy, F.; Richard, D.; Quéré, D.; Clanet, C., Water spring: A model for bouncing drops. *EPL (Europhysics Letters)* **2003,** *62* (2), 237.
167.Prosperetti, A.; Tryggvason, G., *Computational methods for multiphase flow*. Cambridge university press: 2009.
168.Fluent, A., 14.5 Theory Guide. *Canonsburg, PA, USA: ANSYS Inc* **2012**.
169.Baroudi, L.; Kawaji, M.; Lee, T., Effects of initial conditions on the simulation of inertial coalescence of two drops. *Computers & Mathematics with Applications* **2014,** *67* (2), 282-289.
170.Liu, X.; Cheng, P., 3D multiphase lattice Boltzmann simulations for morphological effects on self-propelled jumping of droplets on textured superhydrophobic surfaces. *International Communications in Heat and Mass Transfer* **2015,** *64*, 7-13.
171.Mohammadiun, S.; Neyshabouri, S. S.; Naser, G.; Vahabi, H., Numerical investigation of submerged vane effects on flow pattern in a 90 junction of straight and bend open channels.

Iranian Journal of Science and Technology, Transactions of Civil Engineering **2016,** *40* (4), 349-365.
172. Mohammadiun, S.; Salehi Neyshabouri, S.; Naser, G.; Parhizkar, H.; Vahabi, H., Effects of open-channel geometry on flow pattern in a 90 junction. *Iranian Journal of Science and Technology Transactions of Civil Engineering* **2015,** *39* (C2+), 559-573.
173. Mohammadiun, S.; SALEHI, N. S.; Parhizkar, H.; Vahabi, H., EFFECT OF SEPARATING WALL GEOMETRY ON FLOW PATTERN OF A LARGE-SCALED 90O OPEN-CHANNEL JUNCTION. **2016**.
174. Yue, P.; Zhou, C.; Feng, J. J., A computational study of the coalescence between a drop and an interface in Newtonian and viscoelastic fluids. *Physics of Fluids (1994-present)* **2006,** *18* (10), 102102.
175. Jasper, J. J., The surface tension of pure liquid compounds. *Journal of physical and chemical reference data* **1972,** *1* (4), 841-1010.
176. Liu, T.; Kim, C.-J., Turning a surface superrepellent even to completely wetting liquids. *Science* **2014,** *346* (6213).
177. Nowak, E.; Kovalchuk, N. M.; Che, Z.; Simmons, M. J., Effect of surfactant concentration and viscosity of outer phase during the coalescence of a surfactant-laden drop with a surfactant-free drop. *Colloids and Surfaces A: Physicochemical and Engineering Aspects* **2016,** *505*, 124-131.
178. Weheliye, W. H.; Dong, T.; Angeli, P., On the effect of surfactants on drop coalescence at liquid/liquid interfaces. *Chemical Engineering Science* **2017,** *161*, 215-227.
179. Chinaud, M.; Voulgaropoulos, V.; Angeli, P., Surfactant effects on the coalescence of a drop in a Hele-Shaw cell. *Physical Review E* **2016,** *94* (3), 033101.
180. Mulroe, M. D.; Srijanto, B. R.; Ahmadi, S. F.; Collier, C. P.; Boreyko, J. B., Tuning superhydrophobic nanostructures to enhance jumping-droplet condensation. *ACS nano* **2017,** *11* (8), 8499-8510.
181. Cavalli, A.; Preston, D. J.; Tio, E.; Martin, D. W.; Miljkovic, N.; Wang, E. N.; Blanchette, F.; Bush, J. W., Electrically induced drop detachment and ejection. *Physics of Fluids* **2016,** *28* (2), 022101.
182. Miljkovic, N.; Preston, D. J.; Enright, R.; Wang, E. N., Electrostatic charging of jumping droplets. *Nature communications* **2013,** *4*, 2517.
183. Miljkovic, N.; Preston, D. J.; Enright, R.; Wang, E. N., Jumping-droplet electrostatic energy harvesting. *Applied Physics Letters* **2014,** *105* (1), 013111.
184. Zhang, K.; Liu, F.; Williams, A. J.; Qu, X.; Feng, J. J.; Chen, C.-H., Self-propelled droplet removal from hydrophobic fiber-based coalescers. *Physical review letters* **2015,** *115* (7), 074502.
185. Vahabi, H.; Wang, W.; Mabry, J. M.; Kota, A. K., Coalescence-induced jumping of droplets on superomniphobic surfaces with macrotexture. *Science advances* **2018,** *4* (11), eaau3488.
186. Vahabi, H.; Wang, W.; Mabry, J.; Kota, A., A passive technique for coalescence-induced jumping of droplets (with high viscosity or low surface tension) at Ohnesorge number> 1. *Bulletin of the American Physical Society* **2018**.
187. Segur, J. B.; Oberstar, H. E., Viscosity of glycerol and its aqueous solutions. *Industrial & Engineering Chemistry* **1951,** *43* (9), 2117-2120.
188. Chen, X.; Wu, J.; Ma, R.; Hua, M.; Koratkar, N.; Yao, S.; Wang, Z., Nanograssed micropyramidal architectures for continuous dropwise condensation. *Advanced functional materials* **2011,** *21* (24), 4617-4623.

189.Oh, J.; Birbarah, P.; Foulkes, T.; Yin, S. L.; Rentauskas, M.; Neely, J.; Pilawa-Podgurski, R. C.; Miljkovic, N., Jumping-droplet electronics hot-spot cooling. *Applied Physics Letters* **2017,** *110* (12), 123107.
190.Rykaczewski, K.; Scott, J. H. J.; Rajauria, S.; Chinn, J.; Chinn, A. M.; Jones, W., Three dimensional aspects of droplet coalescence during dropwise condensation on superhydrophobic surfaces. *Soft Matter* **2011,** *7* (19), 8749-8752.
191.Qu, X.; Boreyko, J. B.; Liu, F.; Agapov, R. L.; Lavrik, N. V.; Retterer, S. T.; Feng, J. J.; Collier, C. P.; Chen, C.-H., Self-propelled sweeping removal of dropwise condensate. *Applied Physics Letters* **2015,** *106* (22), 221601.
192.Chakraverty, B. K.; Pound, G., Heterogeneous nucleation at macroscopic steps. *Acta metallurgica* **1964,** *12* (8), 851-860.
193.Gauthier, A.; Symon, S.; Clanet, C.; Quéré, D., Water impacting on superhydrophobic macrotextures. *Nature communications* **2015,** *6*, 8001.
194.Xu, L.-C.; Bauer, J. W.; Siedlecki, C. A., Proteins, platelets, and blood coagulation at biomaterial interfaces. *Colloids and Surfaces B: Biointerfaces* **2014,** *124*, 49-68.
195.Koh, L. B.; Rodriguez, I.; Venkatraman, S. S., A novel nanostructured poly (lactic-co-glycolic-acid)–multi-walled carbon nanotube composite for blood-contacting applications: Thrombogenicity studies. *Acta biomaterialia* **2009,** *5* (9), 3411-3422.
196.Tao, P.; Shang, W.; Song, C.; Shen, Q.; Zhang, F.; Luo, Z.; Yi, N.; Zhang, D.; Deng, T., Bioinspired engineering of thermal materials. *Advanced Materials* **2015,** *27* (3), 428-463.
197.Kashchiev, D., *Nucleation: Basic Theory with Applications*. 1 ed.; Butterworth-Heinemann: Oxford, 2000.
198.Xiao, R.; Miljkovic, N.; Enright, R.; Wang, E. N., Immersion Condensation on Oil-Infused Heterogeneous Surfaces for Enhanced Heat Transfer. *Sci Rep-Uk* **2013,** *3*.
199.Ho, T. A.; Papavassiliou, D. V.; Lee, L. L.; Striolo, A., Liquid water can slip on a hydrophilic surface. *Proceedings of the National Academy of Sciences* **2011,** *108* (39), 16170-16175.
200.Minko, S., Grafting on solid surfaces:"Grafting to" and "grafting from" methods. In *Polymer surfaces and interfaces*, Springer: 2008; pp 215-234.
201.Ortiz, R.; Olsen, S.; Thormann, E., Salt-induced control of the grafting density in poly (ethylene glycol) brush layers by a grafting-to approach. *Langmuir* **2018,** *34* (15), 4455-4464.
202.Patil, R. R.; Turgman-Cohen, S.; Šrogl, J. í.; Kiserow, D.; Genzer, J., Direct measurement of molecular weight and grafting density by controlled and quantitative degrafting of surface-anchored poly (methyl methacrylate). *ACS Macro Letters* **2015,** *4* (2), 251-254.
203.Wang, C.; Yang, Y.; Fang, H., Recent advances on "ordered water monolayer that does not completely wet water" at room temperature. *SCIENCE CHINA Physics, Mechanics & Astronomy* **2014,** *57* (5), 802-809.
204.Rubinstein, M.; Colby, R. H., *Polymer physics*. Oxford university press New York: 2003; Vol. 23.
205.Jokerst, J. V.; Lobovkina, T.; Zare, R. N.; Gambhir, S. S., Nanoparticle PEGylation for imaging and therapy. *Nanomedicine* **2011,** *6* (4), 715-728.
206.Hernáinz-Bermúdez de Castro, F.; Galvez-Borrego, A.; Calero-de Hoces, M., Surface Tension of Aqueous Solutions of Sodium Dodecyl Sulfate from 20 C to 50 C and pH between 4 and 12. *Journal of Chemical & Engineering Data* **1998,** *43* (5), 717-718.
207.Wang, L.; McCarthy, T. J., Covalently attached liquids: instant omniphobic surfaces with unprecedented repellency. *Angewandte Chemie International Edition* **2016,** *55* (1), 244-248.

208.Hutanu, D.; Frishberg, M. D.; Guo, L.; Darie, C. C., Recent applications of polyethylene glycols (PEGs) and PEG derivatives. *Mod Chem Appl* **2014,** *2* (2), 1-6.
209.Padaki, M.; Murali, R. S.; Abdullah, M. S.; Misdan, N.; Moslehyani, A.; Kassim, M.; Hilal, N.; Ismail, A., Membrane technology enhancement in oil–water separation. A review. *Desalination* **2015,** *357*, 197-207.
210.Schmidt, E.; Schurig, W.; Sellschopp, W., Condensation of water vapour in film- and drop form. *Z Ver Dtsch Ing* **1930,** *74*, 544-544.
211.Rose, J. W., Dropwise condensation theory and experiment: a review. *P I Mech Eng a-J Pow* **2002,** *216* (A2), 115-128.
212.Wu, A.; Vahabi, H.; Cha, H.; Chavan, S.; Kota, A. K.; Miljkovic, N. Dropwise Condensation on Hydrophilic Surfaces. University of Illinois at Urbana-Champaign, 2018.
213.Dettre, R., Contact angle, wettability, and adhesion. *Advances in Chemistry Series* **1964,** *43*, 136.
214.Gennes, P.-G. d.; Brochard-Wyart, F.; Quéré, D., *Capillarity and wetting phenomena : drops, bubbles, pearls, waves*. Springer: New York, 2004; p xv, 291 p.
215.Bocquet, L.; Lauga, E., A smooth future? *Nat Mater* **2011,** *10*, 334.
216.Daniel, D.; Timonen, J. V. I.; Li, R.; Velling, S. J.; Kreder, M. J.; Tetreault, A.; Aizenberg, J., Origins of Extreme Liquid Repellency on Structured, Flat, and Lubricated Hydrophobic Surfaces. *Phys Rev Lett* **2018,** *120* (24), 244503.
217.Preston, D. J.; Miljkovic, N.; Sack, J.; Enright, R.; Queeney, J.; Wang, E. N., Effect of hydrocarbon adsorption on the wettability of rare earth oxide ceramics. *Appl Phys Lett* **2014,** *105* (1).
218.Cha, H. Y.; Wu, A.; Kim, M. K.; Saigusa, K.; Liu, A. H.; Miljkovic, N., Nanoscale-Agglomerate-Mediated Heterogeneous Nucleation. *Nano Letters* **2017,** *17* (12), 7544-7551.
219.Lundy, R.; Byrne, C.; Bogan, J.; Nolan, K.; Collins, M. N.; Dalton, E.; Enright, R., Exploring the Role of Adsorption and Surface State on the Hydrophobicity of Rare Earth Oxides. *ACS Applied Materials & Interfaces* **2017,** *9* (15), 13751-13760.
220.Rose, J. W., Condensation heat transfer fundamentals. *Chem Eng Res Des* **1998,** *76* (A2), 143-152.
221.Miljkovic, N.; Enright, R.; Nam, Y.; Lopez, K.; Dou, N.; Sack, J.; Wang, E. N., Jumping-Droplet-Enhanced Condensation on Scalable Superhydrophobic Nanostructured Surfaces. *Nano Letters* **2013,** *13* (1), 179-87.
222.Ölçeroğlu, E.; McCarthy, M., Self-Organization of Microscale Condensate for Delayed Flooding of Nanostructured Superhydrophobic Surfaces. *ACS Applied Materials & Interfaces* **2016,** *8* (8), 5729-5736.
223.Enright, R.; Miljkovic, N.; Alvarado, J. L.; Kim, K. J.; Rose, J. W., Dropwise Condensation on Micro- and Nanostructured Surfaces. *Nanoscale and Microscale Thermophysical Engineering* **2014,** *8* (3), 223-250.
224.Chavan, S.; Cha, H.; Orejon, D.; Nawaz, K.; Singla, N.; Yeung, Y. F.; Park, D.; Kang, D. H.; Chang, Y. J.; Takata, Y.; Miljkovic, N., Heat Transfer through a Condensate Droplet on Hydrophobic and Nanostructured Superhydrophobic Surfaces. *Langmuir* **2016,** *32* (31), 7774-7787.
225.Sett, S.; Yan, X.; Barac, G.; Bolton, L. W.; Miljkovic, N., Lubricant-Infused Surfaces for Low-Surface-Tension Fluids: Promise versus Reality. *ACS Applied Materials & Interfaces* **2017,** *9* (41), 36400-36408.

226.Regan, D. P.; Howell, C., Droplet manipulation with bioinspired liquid-infused surfaces: a review of recent progress and potential for integrated detection. *Current Opinion in Colloid & Interface Science* **2019**.
227.Fuhr, G.; Müller, T.; Schnelle, T.; Hagedorn, R.; Voigt, A.; Fiedler, S.; Arnold, W. M.; Zimmermann, U.; Wagner, B.; Heuberger, A., Radio-frequency microtools for particle and live cell manipulation. *Naturwissenschaften* **1994,** *81* (12), 528-535.
228.Abdelgawad, M.; Wheeler, A. R., The digital revolution: a new paradigm for microfluidics. *Advanced Materials* **2009,** *21* (8), 920-925.
229.Hayes, R. A.; Feenstra, B. J., Video-speed electronic paper based on electrowetting. *Nature* **2003,** *425* (6956), 383.
230.Moon, J. K.; Jeong, J.; Lee, D.; Pak, H. K., Electrical power generation by mechanically modulating electrical double layers. *Nature communications* **2013,** *4*, 1487.
231.Pipper, J.; Zhang, Y.; Neuzil, P.; Hsieh, T. M., Clockwork PCR including sample preparation. *Angewandte Chemie International Edition* **2008,** *47* (21), 3900-3904.
232.Zhang, Y.; Wittstock, G., A Platform for Electric Field Aided and Wire-Guided Droplet Manipulation. *Small* **2017,** *13* (5).
233.Jiang, D.; Park, S.-Y., Light-driven 3D droplet manipulation on flexible optoelectrowetting devices fabricated by a simple spin-coating method. *Lab on a Chip* **2016,** *16* (10), 1831-1839.
234.Chaudhury, M. K.; Whitesides, G. M., How to make water run uphill. *Science* **1992,** *256* (5063), 1539-1541.
235.McCarty, L. S.; Whitesides, G. M., Electrostatic charging due to separation of ions at interfaces: contact electrification of ionic electrets. *Angewandte Chemie International Edition* **2008,** *47* (12), 2188-2207.
236.Wang, Z. L., Triboelectric nanogenerators as new energy technology for self-powered systems and as active mechanical and chemical sensors. *ACS nano* **2013,** *7* (11), 9533-9557.
237.Zheng, L.; Wu, Y.; Chen, X.; Yu, A.; Xu, L.; Liu, Y.; Li, H.; Wang, Z. L., Self-Powered Electrostatic Actuation Systems for Manipulating the Movement of both Microfluid and Solid Objects by Using Triboelectric Nanogenerator. *Advanced Functional Materials* **2017,** *27* (16), 1606408.
238.Reches, M.; Snyder, P. W.; Whitesides, G. M., Folding of electrostatically charged beads-on-a-string as an experimental realization of a theoretical model in polymer science. *Proceedings of the National Academy of Sciences* **2009,** *106* (42), 17644-17649.
239.Burgo, T. A.; Galembeck, F.; Pollack, G. H., Where is water in the triboelectric series? *Journal of Electrostatics* **2016,** *80*, 30-33.
240.Choi, D.; Lee, H.; Kang, I. S.; Lim, G.; Kim, D. S.; Kang, K. H., Spontaneous electrical charging of droplets by conventional pipetting. *Scientific reports* **2013,** *3*, 2037.
241.Wang, W.; Vahabi, H.; Cackovic, M.; Jiang, R.; Kota, A. In *On-demand Droplet Manipulation via Triboelectrification*, APS Meeting Abstracts, 2017.
242.Sun, Y.; Huang, X.; Soh, S., Using the gravitational energy of water to generate power by separation of charge at interfaces. *Chemical science* **2015,** *6* (6), 3347-3353.
243.Lee, C.-P.; Chang, H.-C.; Wei, Z.-H., Charged droplet transportation under direct current electric fields as a cell carrier. *Applied Physics Letters* **2012,** *101* (1), 014103.
244.Walker, J.; Halliday, D.; Resnick, R., Fundamentals of physics 10 ed S Jhonson et al (111 River Street Hoboken. John Wiley & Sons Inc: 2014.

245. Taylor, G. I., The viscosity of a fluid containing small drops of another fluid. *Proceedings of the Royal Society of London. Series A, Containing Papers of a Mathematical and Physical Character* **1932,** *138* (834), 41-48.
246. Lin, Z. H.; Cheng, G.; Lee, S.; Pradel, K. C.; Wang, Z. L., Harvesting water drop energy by a sequential contact-electrification and electrostatic-induction process. *Advanced Materials* **2014,** *26* (27), 4690-4696.
247. Guo, Q.; Singh, V.; Behrens, S. H., Electric charging in nonpolar liquids because of nonionizable surfactants. *Langmuir* **2009,** *26* (5), 3203-3207.
248. Miaoulis, I.; Abedian, B.; Darnahal, M., Theory for electric charging in flow of low-conductivity liquids through screens. *Journal of Electrostatics* **1990,** *25* (3), 287-294.
249. Galembeck, F.; Burgo, T. A.; Balestrin, L. B.; Gouveia, R. F.; Silva, C. A.; Galembeck, A., Friction, tribochemistry and triboelectricity: recent progress and perspectives. *RSC Advances* **2014,** *4* (109), 64280-64298.
250. Brazier, D.; Freeman, G., The effects of pressure on the density, dielectric constant, and viscosity of several hydrocarbons and other organic liquids. *Canadian Journal of Chemistry* **1969,** *47* (6), 893-899.
251. Arnot, J. A.; Gobas, F. A., A review of bioconcentration factor (BCF) and bioaccumulation factor (BAF) assessments for organic chemicals in aquatic organisms. *Environmental Reviews* **2006,** *14* (4), 257-297.
252. Verho, T.; Bower, C.; Andrew, P.; Franssila, S.; Ikkala, O.; Ras, R. H., Mechanically durable superhydrophobic surfaces. *Advanced materials* **2011,** *23* (5), 673-678.
253. Owens, D. K.; Wendt, R., Estimation of the surface free energy of polymers. *Journal of applied polymer science* **1969,** *13* (8), 1741-1747.
254. Mabry, J. M.; Vij, A.; Iacono, S. T.; Viers, B. D., Fluorinated Polyhedral Oligomeric Silsesquioxanes (F-POSS). *Angewandte Chemie* **2008,** *120* (22), 4205-4208.
255. Dong, Z.; Ma, J.; Jiang, L., Manipulating and dispensing micro/nanoliter droplets by superhydrophobic needle nozzles. *ACS nano* **2013,** *7* (11), 10371-10379.
256. Huang, J. Y.; Lo, Y.-C.; Niu, J. J.; Kushima, A.; Qian, X.; Zhong, L.; Mao, S. X.; Li, J., Nanowire liquid pumps. *Nature nanotechnology* **2013,** *8* (4), 277-281.
257. Ferraro, P.; Coppola, S.; Grilli, S.; Paturzo, M.; Vespini, V., Dispensing nano-pico droplets and liquid patterning by pyroelectrodynamic shooting. *Nature nanotechnology* **2010,** *5* (6), 429-435.
258. Mukherjee, P.; Mysels, K., Critical Micelle Concentrations of Aqueous Surfactants, NSRDS-NBS# 36. *Superintendent of Documents, Washington, DC* **1971**.

APPENDICES

CH. 2-1 Supplementary Information

Fabrication of MorphS surfaces:

The photocurable prepolymer solution was prepared by mixing 1,3,5-triallyl-1,3,5-triazine-2,4,6(1H,3H,5H)-trione (TATATO, Sigma-Aldrich Co.), tris[2-(3-mercaptopropionyloxy)ethyl] isocyanurate (TMICN, Bruno Bock) and tricyclodecane dimethanol diacrylate (TCDDA, Sigma-Aldrich Co.) at a molar ratio of 0.345:0.345:0.31 (TATATO:TMICN:TCDDA). The concentration of the photoinitiator, 2,2-dimethoxy-2-phenylacetophenone (DMPA, Sigma-Aldrich Co.), was 0.1 wt.%. After thorough mixing, the pre-polymer solution was applied to the surface of a cleaned silicon wafer via spin coating. The shape memory polymer thin film (~55 μm thick) was obtained by irradiating the spin coated sample with 365 nm UV light for an hour and post-curing overnight at 120˚C. In order to fabricate the SMP pillars, first, a 220 nm thick silicon oxynitride layer was deposited on the top of cured shape memory film through plasma enhanced chemical vapor deposition (PECVD, Figure 2-3). Then, a 1.5 μm thick layer of photoresist S1813 (DOW Electronic Materials) was spin coated on the sample surface and baked at 115˚C. Hexamethyldisilazane was used as primer to provide good adhesion between the silicon oxinitride layer and photoresist layer. Upon UV irradiation of the photoresist through masks with hexagonal arrays of circles (with different circle size and inter-circle spacing) at a dose of 110 mJ/cm^2 using a mask aligner (Karl Suss MA6B Contact Printer) and subsequently developing the photoresist in MF-319 (DOW Electronic Materials), hexagonal patterns of photoresist columns was obtained. These hexagonal patterns were transferred into the silicon

oxinitride layer via reactive ion etching (RIE) at ~30 °C and a pressure of 120 mTorr using a CF_4/O_2 gas mixture. The shape memory polymer pillars were then etched using O_2 RIE at elevated temperatures (~200 °C) and at a pressure of 220 mTorr. Upon removal of the silicon oxynitride layer using hydrofluoric (HF) acid, surfaces with hexagonally arranged mushroom-like pillars fabricated with the thermo-responsive shape memory polymer were obtained. The surfaces were further modified via vapor phase silanization at 120˚C for 1 hour using 200 μL of heptadecafluoro-1,1,2,2-tetrahydrodecyl trichlorosilane (Gelest) to impart low solid surface energy.

Characterization of surface morphology and solid surface energy:

The surface morphology was examined using a scanning electron microscope (SEM; JEOL JSM-6500F) at 10 kV. Owens-Wendt approach[253] was used to estimate the solid surface energy of the MorphS surfaces by employing non-textured, fluorinated shape memory polymer films with n-hexadecane ($\theta \approx \theta_{adv} = 79°$) as the non-polar liquid and water ($\theta \approx \theta_{adv} = 114°$) as the polar liquid.

Measurement of contact angles and roll off angles:

A contact angle goniometer (Ramé-Hart 200-F1) was used to measure the contact angles and roll off angles. The contact angles were measured by advancing or receding ~8 μL droplets on the surface using a micrometer syringe (Gilmont). The roll-off angles were determined by tilting the stage until the ~8 μL droplet rolled off from the surface. Five measurements were performed on each surface. The errors in contact angle and roll-off angle were ±1° and ±1°, respectively.

Ex-situ wetting transition:

To induce the morphological transformation, the MorphS surface with the mushroom-like pillar texture was heated to a temperature of 65˚C, which is higher than the glass transition temperature $T_g \approx 60$℃ of the SMP, using a heating stage mounted on the contact angle goniometer. A compressive stress (~10 MPa) was exerted on the heated surface over an area of 1 cm^2. The surface was then quickly cooled down to room temperature with nitrogen. The morphology was transformed and "locked" into a new collapsed pillar texture. When the collapsed pillar texture was reheated to a temperature of 65°C, the morphology transformed to the mushroom-like pillar texture within 1 minute due to the ramp rate of the hot plate, and the surface was subsequently cooled to room temperature. The surface wettability was characterized by measuring the contact angles and roll off angles of water and n-hexadecane, with different droplets on the as-prepared or the recovered mushroom-like pillar texture and the collapsed pillar texture.

In-situ wetting transition:

A droplet of water or formamide was placed on the collapsed pillar texture and heated to ~65°C within 1 minute using a heating stage mounted on the contact angle goniometer. Due to the ramp rate of the heating stage, it took ~55 s for the surface temperature T to increase from room temperature to 65°C (i.e., above the glass transition temperature $T_g \approx 60$℃ of shape memory polymer). The actual transition of the collapsed pillar texture to the mushroom-like pillar texture occurred in < 10 s when $T > T_g$ (Figure 2-6.a and 2-6.b). Snapshots of the droplet on the surface were obtained as the morphology transformed from the collapsed pillar texture to the mushroom-like pillar texture. The droplet volume was estimated via image analysis.

CH. 2-2 Supplementary Information

Fabrication of superomniphobic surfaces:

We fabricated hierarchically structured (i.e., a finer length scale texture superimposed on an underlying coarser length scale texture), re-entrant textured, superomniphobic surfaces by conformally spray coating stainless steel wire meshes (coarser texture) with blends of fluorodecyl POSS and super-fast instant adhesive SF100 (finer texture). As received, corrosion-resistant, 304 stainless steel wire meshes (wire diameter ≈ 25 μm and pore size ≈ 38±1 μm; McMaster) were cut into the required size (e.g., 2 cm × 2 cm), rinsed with DI water, cleaned in acetone (Fisher Scientific) with an ultrasonic cleaner (Branson) for 5 min and then dried with nitrogen (Airgas). No further surface treatment was performed on the stainless steel wire meshes. A 20 mg/ml solution of 20 wt% SF100 (super-fast instant adhesive, 3M^{TM}) + 80 wt% fluorodecyl POSS^{254} in Asahiklin AK-225 (Asahi Glass) was spray coated (at a pressure of 30 psi) on the wire mesh using an air brush (Paasche) held 15 cm from the surface. Subsequently, the substrate was allowed to dry at room temperature for an hour. The pore size of the wire mesh reduced to ≈ 14±5 μm after spray coating the blends of fluorodecyl POSS and super-fast instant adhesive SF100 to make it superomniphobic.

Morphology characterization:

The morphology of the superomniphobic surfaces was imaged using a scanning electron microscope (SEM; JEOL 6500F) at 5 kV.

Root mean square roughness measurements:

The root mean square roughness R_{rms} of the surfaces was measured with a 3D optical profilometer (Veeco). At least five measurements were performed at different locations on each

surface. The root mean square roughness $R_{rms} \approx 5\pm1$ μm, for the finer texture (spray coated blends of fluorodecyl POSS and super-fast instant adhesive SF100) of our superomniphobic surfaces.

Contact angle and surface tension measurements:

A contact angle goniometer and tensiometer (Ramé-Hart 260) was used to measure the apparent contact angles (sessile droplet method) and surface tensions (pendant droplet method) using ≈ 2 μL droplets. At least six measurements were performed on each surface. The errors in contact angle, roll off angle and surface tension measurements were ±2°, ±1° and ±1 mN m^{-1}, respectively.

Liquids used for droplet coalescence experiments:

We employed a micropipette (Fisher Scientific) to dispense droplets of DI water with different radii (450 μm < R_0 < 760 μm; this range of droplet radius was easily accessible using a simple syringe, without using complex techniques[255-257]) onto the superomniphobic surfaces. Droplets of different viscosity were obtained by using DI water containing different compositions of glycerol (Sigma-Aldrich).[187] Droplets of different surface tension were obtained by using water containing different concentrations of sodium dodecyl sulfate (SDS; Fisher Scientific).[206] Using SDS in water, the lowest surface tension γ_{lv} that can be achieved is $\gamma_{lv} \approx 38$ mN m^{-1}, at the Critical Micelle Concentration, $CMC \approx 8$ mM.[206, 258] The apparent advancing contact angle θ^*_{adv}, the apparent receding contact angle θ^*_{rec} and physical properties of the tested liquids are listed in **Table SI 2-2-1**.

TABLE SI 2-2-1. Density, viscosity, surface tension, apparent advancing contact angle and apparent receding contact angle of various test liquids on superomniphobic surfaces.

Liquid	Density, ρ [kg m^{-3}]	Viscosity, μ [mPa s]	Surface tension, γ_{lv} [mN m^{-1}]	Apparent advancing contact angle, θ^*_{adv} [°]	Apparent receding contact angle, θ^*_{rec} [°]
Water	998	1	72	165°	163°
water + 20% glycerol	1047	1.8	71	164°	162°
water + 40% glycerol	1099	3.7	70	164°	162°
water + 50% glycerol	1126	5.1	69	163°	160°
water + 60% glycerol	1154	10.8	68	163°	160°
water + 65% glycerol	1167	15.2	68	163°	160°
water + 80% glycerol	1208	60.1	66	162°	158°
water + 84% glycerol	1219	98	65	162°	158°
water + 90% glycerol	1235	219	64	162°	158°
1 mM SDS in water	998	1	67	162°	159°
1.5 mM SDS in water	998	1	61	161°	158°
2 mM SDS in water	998	1	56	160°	155°
3 mM SDS in water	998	1	46	158°	152°
6 mM SDS in water	998	1	40	157°	151°
n-hexadecane	770	3	27.5	156°	147°

Droplet coalescence experiments:

In all of our experiments, we dispensed two droplets of equal volume very close to each other (~2 mm apart) on a horizontally placed superomniphobic surface. The droplets were dispensed using a calibrated micropipette, which is a simple technique that allowed reasonable control over the volume, and consequently the droplet radius R_0. Leveraging the negligible contact angle hysteresis on our superomniphobic surface, we used a syringe to blow air on one of the stationary droplets so that it gradually (with horizontal approach velocity $V_h < 0.01$ m s^{-1} in all our experiments) moved towards and coalesced with the second droplet. In all our

experiments, the kinetic energy due to the horizontal approach velocity is $\sim\rho R_0^3 V_h^2 < 10^{-11}$ J and the released excess surface energy is $\sim\gamma_{lv} R_0^2 > 10^{-8}$ J. In other words, in all our experiments, $\frac{V_h}{V_{ic}} < 10^{-3}$. Consequently, we anticipate that the non-zero horizontal approach velocity does not play a significant role in our coalescence-induced droplet jumping experiments.[113] We determined the jumping velocity V_j of the coalesced droplet from the droplet trajectories using a technique explained in prior work.[4, 113] High-speed movies of coalescing droplets were obtained using a high-speed camera (Photron Fastcam SA3) at 5000 frames per second. The trajectory of the coalesced droplet was recorded using the 'center of mass' based on the video images.[113] All experiments were conducted at room temperature. In all our experiments, Bond number $Bo = \rho g R_0^2/\gamma_{lv} < 0.1$ (i.e., very low).

CH. 2-3 Supplementary Information

Components of Velocity

The volume of fluid (VOF) model is employed here to simulate the two immiscible fluids (i.e., air *a* and the test liquid *l*) by solving a single set of momentum equations and tracking the volume fraction of each of the phases throughout the domain.[114] This model assumes that each cell within the computational domain contains either one phase (i.e., air *a* or test liquid *l*) or two phases (i.e., both air *a* or test liquid *l*) separated by an interface. In each cell, the volume fraction β of each phase is tracked. For example, if the cell contains only the test liquid, $\beta_l = 1$ and $\beta_a = 0$; and when the cell contains both the phases, $0 < \beta_l < 1$ and $0 < \beta_a < 1$. For each cell, equivalent properties (e.g., density ρ) of the phase mixture are calculated by a rule of mixtures as $\rho_{cell,eq} = \beta_{cell,a}\rho_a + \beta_{cell,l}\rho_l$, where $\beta_{cell,l} + \beta_{cell,a} = 1$. The mass of each cell is

$m_{cell} = \rho_{cell,eq}\phi_{cell}$, where ϕ_{cell} is the volume of the cell. The equivalent properties are then used to solve a single set of momentum equations at each cell throughout the computational domain and determine the velocity components for each cell (i.e., $V_{cell,x}$, $V_{cell,y}$ and $V_{cell,z}$). At each time step, once the volume fractions $\beta_{cell,a}$(t) and $\beta_{cell,l}$(t) and the velocity components $V_{cell,x}$(t), $V_{cell,y}$(t) and $V_{cell,z}$(t) are determined for each cell, the magnitude of velocity for each cell is determined as:

$$V_{cell,total}(t) = \left\{V_{cell,x}^2(t) + V_{cell,y}^2(t) + V_{cell,z}^2(t)\right\}^{1/2} \qquad \text{(S2-3-1)}$$

During coalescence, the droplet deforms symmetrically relative to the *xz* and *yz* planes (see Figure SI 2-2-1). Consequently, at each time step, the net velocity of the droplet in x direction $V_{net,x}$(t) = 0 and the net velocity of the droplet in the y direction $V_{net,y}$(t) = 0 (i.e., the center of mass of the droplet does not move in the *x* direction or the *y* direction). However, due to symmetry breaking caused by the superomniphobic surface without or with a ridge, the net velocity of the droplet in *z* direction (i.e., net upward velocity of the droplet) $V_{net,z}(t) = V_{up}(t) \neq 0$. Recognizing that different cells in the computational domain have different mass, this net upward velocity can be estimated through the mass-weighted average of the z component of the velocity in each cell as:

$$V_{up}(t) = \frac{\sum\left\{m_{cell,+z}(t)\,V_{cell,+z}(t) - m_{cell,-z}(t)\,V_{cell,-z}(t)\right\}}{m_c} \qquad \text{(S2-3-2)}$$

Here, $m_{cell,+z}$(t) and $V_{cell,+z}$(t) are the mass and the magnitude of the *z* component of the velocity in cells with positive (i.e., upward) $V_{cell,z}$(t). Similarly, $m_{cell,-z}$(t) and $V_{cell,-z}$(t) are the mass and the magnitude of the *z* component of the velocity in cells with negative (i.e., downward) $V_{cell,z}$(t). Note that $m_c = \rho 4\pi R_c^3/3$ is the mass of the coalesced droplet.

In-plane, Out-of-plane and Total Kinetic Energy

During coalescence, the excess surface energy $E_{surf,ex}$(t) of the droplet is released (see **Figure 2-13a** and **2-14a**) and partly converted into the total kinetic energy $E_{kin,total}$(t) of the droplet. The total kinetic energy of the droplet can be estimated as the sum of the total kinetic energy of the cells within the entire computational domain as:

$$E_{kin,total}(t) = \frac{1}{2}\sum\left\{m_{cell}(t)V_{cell,total}^2(t)\right\} \qquad \text{(S2-3-3)}$$

Note that $V_{cell,total}$(t) is defined by equation S2-3-1 and the total kinetic energy $E_{kin,total}$(t) of the droplet is the sum of the in-plane kinetic energy (in x and y directions) and out-of-plane kinetic energy (in the z direction). During the coalescence, the in-plane kinetic energy manifests as symmetric deformation of the droplet (relative to the xz and yz planes), in the plane of coalescence (i.e., xy plane, see **Figure 2-13b** through **2-13f**, **Figure 2-14b** through **2-14f** and **Section S3**). During stage I of coalescence (see Figure 2-13a and 2-14a), the out-of-plane kinetic energy manifests as symmetric deformation of the droplet perpendicular to the plane of coalescence. During stages II and III of coalescence (see Figure 2-13a and 2-14a), the out-of-plane kinetic energy manifests as both the deformation of the droplet perpendicular to the plane of coalescence and net motion of the center of mass of the droplet in the upward (i.e., $+z$) direction (see **Figure 2-13c** through **2f** and **Figure 2-14c** through **2-14f** as well as Section S3). The upward kinetic energy (i.e., kinetic energy by virtue of the net upward velocity) is a fraction of the total kinetic energy of the droplet that is given as:

$$E_{kin,up}(t) = \frac{1}{2}m_c V_{up}^2(t) \qquad \text{(S2-3-4)}$$

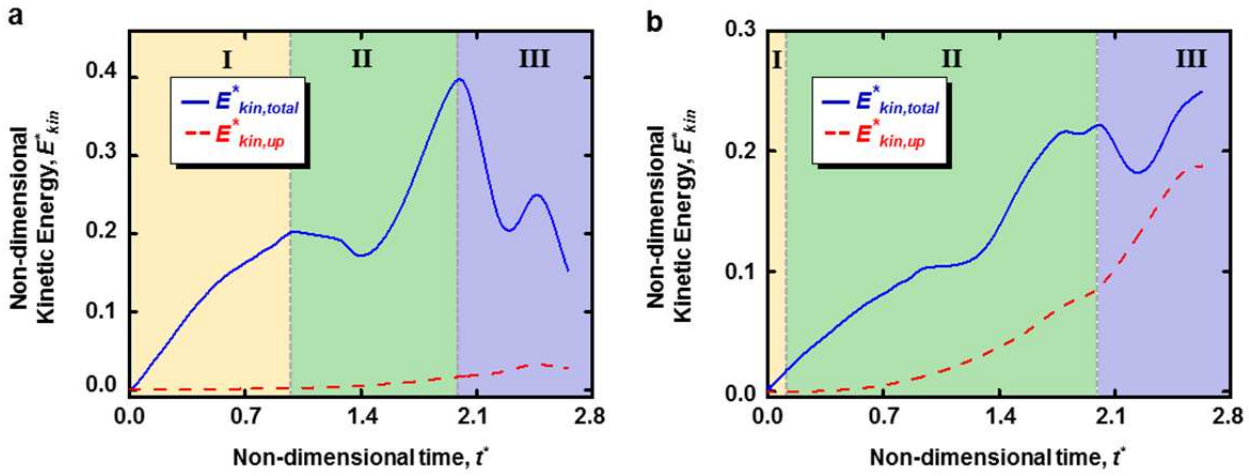

Figure S2-3-1. Components of the total kinetic energy. Evolution of the non-dimensional total kinetic energy $E^*_{kin,total}$ and the upward kinetic energy of the droplets $E^*_{kin,up}$ coalescing on a superomniphobic surface **a)** without and **b)** with a ridge.

V_{up}(t) is defined by equation S2-3-2. In our analysis, we non-dimensionalized the total kinetic energy as $E^*_{kin,total}(t^*) = E_{kin,total}(t) / E_{surf,ex}(0)$, and the upward kinetic energy as $E^*_{kin,up}(t^*) = E_{kin,up}(t) / E_{surf,ex}(0)$. Comparison of the kinetic energies of a coalescing water droplet (R_0 = 600 μm) on a superomniphobic surface with a ridge (ridge height $h_r \approx$ 500 μm) and without a ridge (see **Figure S2-3-1a** and **S2-3-1b**) indicates that the ratio of the upward kinetic energy to the total kinetic energy when the droplet departs from the surface $E^*_{kin,up}(t^*_d) / E^*_{kin,total}(t^*_d) \approx$ 76% and 19% for with and without a ridge, respectively. This implies a more effective redirection of velocity vectors during coalescence on a superomniphobic surface with a ridge compared to that on a superomniphobic surface without a ridge.

Evolution of the Droplet Dynamics (yz view) during Droplet Coalescence

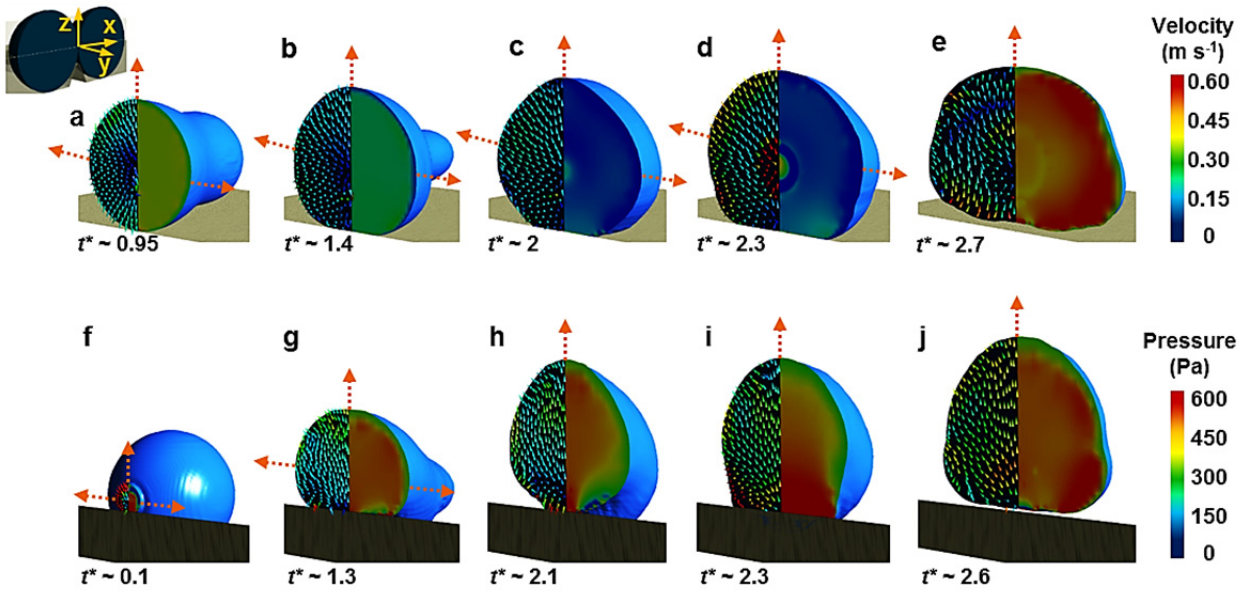

Figure S2-3-2. Velocity vectors and pressure distribution (*yz* view). a-e) A series of snapshots showing the pressure distribution and velocity vectors within the droplet on a superomniphobic surface without a ridge; **f-j)** A series of snapshots showing the pressure distribution and velocity vectors within the droplet on a superomniphobic surface with a ridge (ridge height $h_r \approx 500$ μm). The colors represent the magnitude of pressure and velocity.

Applicability to Smaller Droplets (R0 < 10 μm)

We demonstrated that our strategy to enhance the energy conversion efficiency in coalescence-induced jumping of droplets by using a ridge (with height comparable to the droplet radius) is applicable to droplets with radius R_0 on the order of tens of μm to hundreds of μm (see Figure 2-16). In some applications (e.g., condensation), there can be a wide droplet size distribution, including smaller droplets with radius $R_0 < 10$ μm. In order to demonstrate that our strategy can indeed be applied to smaller droplets with radius $R_0 < 10$ μm, we conducted numerical simulations on coalescence of water droplets with $R_0 = 5$ μm on superomniphobic surfaces (water contact angle $\theta = 165°$) without a ridge and with a ridge (non-dimensional ridge height $h^* = 0.95$, i.e., ridge height $h_r \sim 4.75$ μm).

Our results (see **Figure S2-3-3**) indicate that on the superomniphobic surface without a ridge the energy conversion efficiency $\eta \approx 1.8\%$ (coalesced droplet can barely jump away), while on the superomniphobic surface with a ridge, the energy conversion efficiency $\eta \approx 22.3\%$ (i.e., about 1200% increase in energy conversion efficiency).

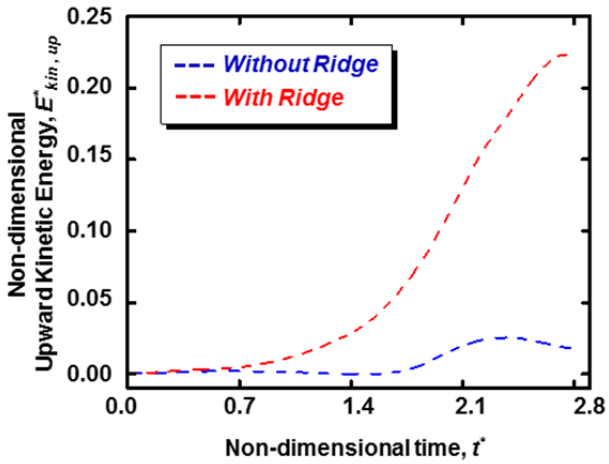

FIGURE S2-3-3. Coalescence-induced jumping of smaller droplets. Evolution of the non-dimensional upward kinetic energy ($E^*_{kin,up}$) during the coalescence of water droplets ($R_0 \approx 5$ μm) on a superomniphobic surface without and with a ridge ($h^* = 0.95$).

Coalescence of Low Surface Tension and High Viscosity Droplets

Coalescence of low surface tension droplets (e.g., n-tetradecane with $\mu \approx 2.1$ mPa s, $\rho \approx$ 760 kg m^{-3}, $\gamma_{lv} \approx 26.6$ mN/m, $R_0 \approx 480$ μm) and high viscosity droplets (e.g., water + 90% glycerol with $\mu \approx 220$ mPa s, $\rho \approx 1230$ kg m-3, $\gamma_{lv} \approx 64$ mN/m, $R_0 \approx 480$ μm) on superomniphobic surfaces without a ridge is shown in **Figure S2-3-4a** and **S2-3-4b**. It is evident that the low surface tension and high viscosity droplets cannot jump away from a superomniphobic surface without a ridge.

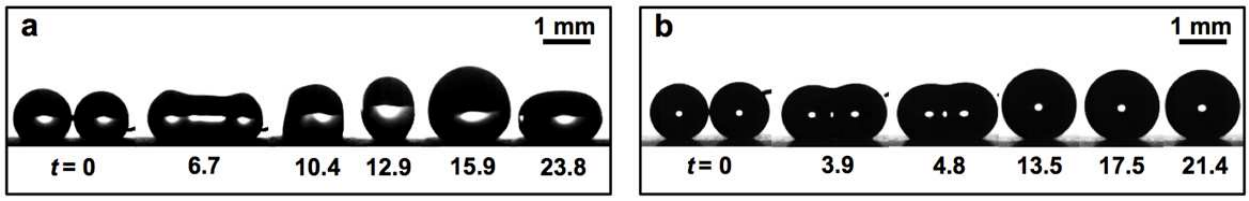

FIGURE S2-3-4. Coalescence of low surface tension and high viscosity droplets. a) A series of snapshots showing the coalescence of n-tetradecane droplets on a superomniphobic surface without a ridge. **b)** A series of snapshots showing the coalescence of water + 90% glycerol droplets on a superomniphobic surface without a ridge. Note the droplets cannot jump away from the surfaces.

Influence of the Ridge Angle

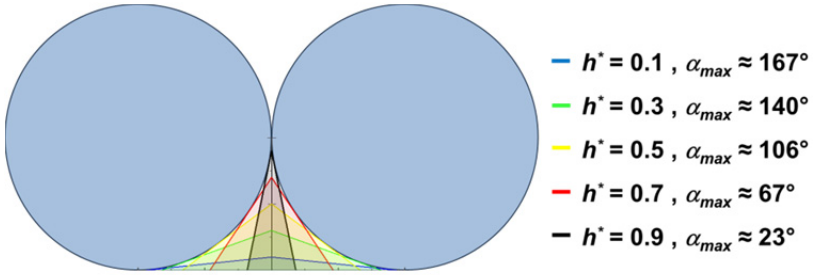

FIGURE S2-3-5. Schematic depicting the influence of non-dimensional ridge height h^* on the maximum ridge angle α_{max}.

In order to determine if the ridge angle α influences the energy conversion efficiency η significantly, we conducted numerical simulations at a low ridge angle ($\alpha \approx 10°$) and a high ridge angle ($\alpha \rightarrow \alpha_{max}$) for non-dimensional ridge heights h^* = 0.1, 0.5, 0.9 (see **Figure S2-3-5**). Our results (see **Table S2-3-1**) indicate that η increases with increasing α (especially evident at lower h^*). This is because, as α increases, the ridge intervenes in the coalescence process earlier and leads to effective redirection of in-plane velocity vectors to out-of-plane. From a fundamental standpoint, a more detailed study is necessary to thoroughly understand the influence of the ridge angle α on the detailed droplet dynamics. From an applied standpoint, the increase in energy conversion efficiency η due to increase in ridge angle α is limited to lower non-dimensional

ridge heights h^* (with lower energy conversion efficiency η); and it is not as significant as the increase in energy conversion efficiency η due to increase in non-dimensional ridge height h^*.

Table S2-3-1. Influence of the ridge angle α on the energy conversion efficiency η in coalescence-induced jumping of droplets with radius R_0 = 600 μm at different non-dimensional ridge heights h^*.

h^*	α [°]	η [%]
0.1	10	4.9
0.1	160	8.0
0.5	10	11.8
0.5	100	13.5
0.9	10	18.8
0.9	20	18.9

Hierarchical Structure for Coalescence-induced Jumping of Droplets at Different Length Scales

Our results indicate that super-repellent surfaces designed with macrotextures (e.g., triangular ridges with height comparable to the droplet radius) can enhance the energy conversion efficiency in coalescence-induced jumping of droplets. This can have significant implications for a wide variety of applications including self-cleaning, anti-icing, energy harvesting, hot spot cooling, lab-on-chip devices and condensation, especially with high viscosity and/or low surface tension droplets.

If the enhanced energy conversion efficiency is to be obtained throughout the super-repellent surface, it requires a periodic arrangement of triangular ridges (e.g., discrete tetrahedrons or continuous ridges) with height comparable to the droplet radius. In some applications (e.g., condensation), there can be a wide droplet size distribution, spreading over multiple length scales. If the enhanced energy conversion efficiency is to be obtained in such cases, it requires a super-repellent surface that is hierarchically structured with ridges at multiple

length scales so that the finer ridges can enhance the energy conversion efficiency for the smaller droplets and the coarser ridges can enhance the energy conversion efficiency for the larger droplets (see **Figure S2-3-6a**). On such surfaces, at each ridge of each length scale, we anticipate heterogeneous nucleation to predominantly occur along the edges of the base of the ridge due to lower free energy barrier,[191-192] followed by droplet growth and coalescence-induced jumping with enhanced energy conversion efficiency (**Figure S2-3-6b**). Further, for each application, the geometry, size and pitch of the ridges at each length scale must be optimized within the parametric space allowed by the fabrication techniques and the geometric limitations for coalescence – ridge angle $\alpha < \alpha_{max}$ (equation 2-19) and the ridge height $h_r \leq D$ (half the inter-feature spacing).

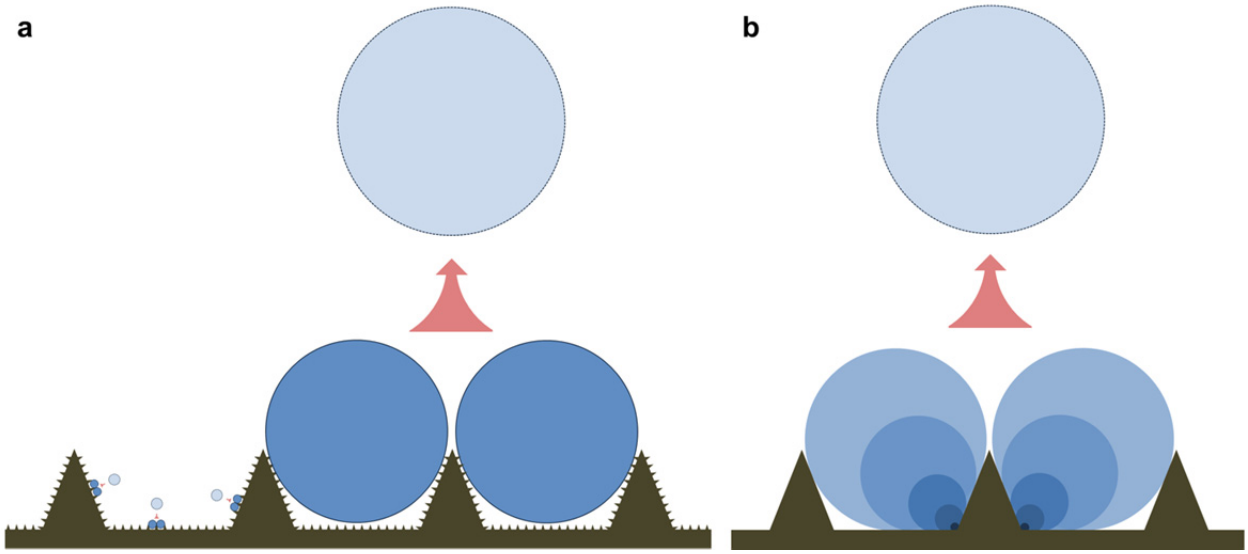

FIGURE S2-3-6. Schematic of a super-repellent surface with periodic arrangement of triangular ridges. a) Super-repellent surfaces with hierarchically structured ridges at two length scales. The finer ridges enhance the energy conversion efficiency for the smaller droplets and the coarser ridges enhance the energy conversion efficiency for the larger droplets. **b)** Heterogeneous nucleation (along the edges of the base of the ridge) and droplet growth, followed by coalescence-induced jumping on the super-repellent ridge.

CH. 3-1 Supplementary Information

Fabrication of Slippery Hydrophilic (SLIC) Solid Surfaces

Silicon wafers (<1 0 0> orientation) were cut to 2 cm × 2 cm, cleaned by sonication in acetone and ethanol, rinsed with deionized (DI) water and dried with nitrogen. For PEGylation, cleaned silicon wafers were exposed to oxygen plasma (PlasmaEtch) for 5 min and subsequently immersed in a solution consisting of 1 µl of 2-[Methoxy(polyethyleneoxy)6-9propyl] tri-methoxysilane and 8 µl of hydrochloric acid in 10 ml of anhydrous toluene for required time (t_{PEG}) at room temperature. Finally, the PEGylated surfaces were rinsed thoroughly with anhydrous toluene, ethanol and DI water and stored for further use.

Fabrication of Slippery Hydrophobic Solid Surfaces

Details of the experimental protocol to fabricate slippery hydrophobic solid surfaces can be found elsewhere.[207]

Hydrophilic Silicon Wafer

Silicon wafers (<1 0 0> orientation) were cut to 2 cm × 2 cm, cleaned by sonication in acetone and ethanol, rinsed with deionized (DI) water and dried with nitrogen.

X-ray photoelectron spectroscopy (XPS)

XPS analysis was conducted on the surfaces using a PHI-5800 spectrometer (Physical Electronics). XPS was conducted using a monochromatic Al Kα X-ray source operated at 15 kV and photoelectrons were collected at a takeoff angle of ≈45° relative to the sample surface. At least 30 different locations were analyzed to assess the chemical homogeneity of the PEGylated surfaces.

Atomic Force Microscopy (AFM)

The surface morphology and the surface roughness of the substrates were characterized with AFM (Bruker MultiMode 8-HR). AFM was conducted with silicon nitride probes mounted on cantilevers in the ScanAsyst® mode. AFM images were acquired by scanning 5 μm x 5 μm areas on the PEGylated surfaces in air, under ambient laboratory conditions, at a scan rate of 1 Hz. The images were analyzed with NanoScope Analysis 1.8 software to obtain the root mean square roughness R_{rms}. At least 30 different locations were analyzed to assess the roughness of the PEGylated surfaces.

Ellipsometry

The thickness of the dry brush was measured by Ellipsometry using a J.A. Woollam variable angle spectroscopic Ellipsometry (model VASE-VB-250). For Ellipsometry measurements, oxidized silicon wafers were used. A spectral scan of the surface was collected between 500 and 900 nm with an incident angle between 60 and 80°, in increments of 5°. The dry brush thickness was determined using a three-layer planar model of the solid surface from the collected spectra, considering the refractive index of air (n = 1.003), PEG (n = 1.45), fused silica upper layer (n = 1.457), and silicon (n = 3.881), and subsequently related to grafting density (σ) using equation 3-1 and then to inter-tether distance using $D \sim 2/\sqrt{\pi\sigma}$.[202]

Measurement of contact angles and sliding angles

The contact angles were measured using a contact angle goniometer (Rame-Hart 200-F1). The contact angles were measured by advancing or receding ~8 μL droplets on the surface. At least six measurements were performed on each surface. the sliding angles were measured through tilting the stage of a contact angle goniometer (Rame-Hart 200-F1).

CH. 3-2 Supplementary Information

Fabrication of Slippery Hydrophobic Solid Surfaces

Glass cover slips (purchased from VWR) were cleaned by sonication in acetone and ethanol, rinsed with deionized (DI) water and dried with nitrogen. Then, cleaned cover slips were exposed to oxygen plasma (PlasmaEtch) for 5 min and subsequently dip coated in a solution consisting of 1 ml of Chlorine terminated polydimethylsiloxane and 10 ml of hexane (in glass petri dishes). The cover slips were gradually removed from the glass petri dishes and let the excess solution fully evaporate on the surface. Finally, the modified surfaces were rinsed thoroughly with hexane and DI water and dried with nitrogen.